AN EXPERIMENTAL INVESTIGATION OF A SMALL-SCALE AEROTHERMOPRESSOR-- A DEVICE FOR INCREASING THE STAGNATION PRESSURE OF A HIGH-TEMPERATURE, HIGH-VELOCITY GAS STREAM BY EVAPORATIVE COOLING

by

KENNETH ROBERT WADLEIGH
S.B., S.M.
Massachusetts Institute of Technology, 1943

SUBMITTED IN PARTIAL FULFILLMENT OF THE REQUIREMENTS
FOR THE DEGREE OF DOCTOR OF SCIENCE

at the

MASSACHUSETTS INSTITUTE OF TECHNOLOGY
June, 1953

Signature of Author ______________________________
Department of Mechanical Engineering, May 18, 1953

Certified by ______________________________
Thesis Supervisor

Accepted by ______________________________
Chairman, Departmental Committee on Graduate Students

Biographical Note

Kenneth Robert Wadleigh was born in Passaic, New Jersey, on March 27, 1921. After graduation from Clifton, New Jersey, High School, he attended the Massachusetts Institute of Technology, from which he received the degrees of Bachelor of Science and Master of Science in 1943.

He served in the United States Naval Reserve from 1943 to 1946 as engineering officer in the Pacific area for an M.T.B. Squadron and later on an LCI. In 1945, he was assigned to the Ames Aeronautical Laboratory of the NACA, where he worked on the development of thermal-anti-icing equipment for aircraft.

In 1946, Wadleigh returned to M.I.T. as an Instructor of Mechanical Engineering. He became Assistant Professor of Mechanical Engineering in 1949. Since 1947, he has been a consultant to Arthur D. Little, Inc.

He is the author of:

"A Preliminary Study of Ram-Activated Cooling Systems for Supersonic Aircraft" (with J. R. Stalder), NACA RM A7C04, April, 1947.

"A New Method of Calculation of Reheat Factors for Turbine and Compressor" (with Joseph Kaye), Journal of Applied Mechanics, Vol. 18, No. 4, December, 1951.

Acknowledgements

I owe thanks to Professor C. R. Soderberg and Professor J. H. Keenan, my superiors, for their generous encouragement and for their permission to curtail my academic teaching schedule in order to carry out the research work.

I am particularly indebted to Professor A. H. Shapiro for his guidance and his whole-hearted cooperation as my thesis supervisor. He is primarily responsible for the invention of the aerothermopressor, for most of the special instrumentation used in connection with it, and for the bases of most of the theoretical analyses of the aerothermopressor process.

Co-workers on the aerothermopressor project who contributed greatly to this work include Bruce Gavril, who designed much of the equipment and carried out many of the analyses, and Howard Larson who assisted with the problem of humidity measurement.

Professors E. S. Taylor, E. P. Neumann, and R. C. Dean of the Gas Turbine Laboratory cooperated in many ways. Harry Foust, who served as chief mechanic on the project, and James Hands of the Gas Turbine Laboratory staff deserve credit for overcoming many practical difficulties.

Thanks are also due Miss Margaret Tefft for computing aid and to Miss Mary Sheehan for secretarial help.

K. R. Wadleigh

Abstract

AN EXPERIMENTAL INVESTIGATION OF A SMALL-SCALE AEROTHERMOPRESSOR--A DEVICE FOR INCREASING THE STAGNATION PRESSURE OF A HIGH-VELOCITY, HIGH-TEMPERATURE GAS STREAM BY EVAPORATIVE COOLING

by

Kenneth R. Wadleigh

Submitted to the Department of Mechanical Engineering in partial fulfillment of the requirements for the degree of Doctor of Science.

The purpose of this investigation was to determine whether or not appreciable increases in stagnation pressure might be achieved through the evaporative cooling effects of liquid water injected into a high-velocity, high-temperature gas stream (the "aerothermopressor" process). It was recognized at the outset that net increases in stagnation pressure can be achieved only in large-scale devices. Consequently, the data obtained in this investigation were to be used to gain a better understanding of the complex processes which occur and to extrapolate measured performance to large-scale aerothermopressors.

The aerothermopressor used in the experimental work consisted of a bellmouth nozzle, a constant area evaporation section 2 1/8 inches in diameter and 73 1/4 inches long, and a diffuser of six degree total angle of divergence. Air which was heated by combustion in a gas furnace was drawn through the aerothermopressor by means of the steam ejector of the M.I.T. Gas Turbine Laboratory. Liquid water was injected into the gas stream at the exit of the bellmouth nozzle. The effects of water injection were inferred from static pressure measurements and from direct humidity measurements. Static pressure variations along the evaporation section were measured, and a special probe was developed to sample the vapor from the liquid-vapor mixture. The humidity of the sample obtained from the probe was measured in a specially-constructed apparatus which utilized a Foxboro "Dewcel" as the primary measuring element.

The overall performance of the aerothermopressor was measured in terms of the normalized stagnation pressure rise $(p_{03}-p_{01})/(p_{01}M_1^2)$ where p_{01} and p_{03} and respectively the stagnation pressures at the entrance to the bellmouth and exit of the diffuser, and M_1 is the mach number at the exit of the bellmouth nozzle. As expected, an overall rise in stagnation pressure was not achieved because the scale of the aerothermopressor was too small. The detrimental effects of wall friction were, therefore, controlling in relation to the favorable effects of evaporative cooling.

The overall performance was found to increase with increasing initial mach number M_1, to increase with initial stagnation temperature T_{01}, and, in this scale, to decrease with initial stagnation pressure p_{01}. For each initial stagnation state and mach number, there was found to exist an optimum rate of water injection rate ω_0. The performance was sensitive to the type of water injection apparatus used. The most satisfactory injection scheme was found to

be a group of axial injection tubes distributed in the cross-section of the exit plane of the bellmouth nozzle.

The best performance achieved was as follows:

T_0, °R	p_0, atm	M_1	ω_0 lb water/lb air	$\left(\frac{p_{03} - p_{01}}{p_{01}\, M_1^2}\right)_{opt}$
1200	1	.777	0.17	-0.229
1500	1	.780	0.24	-0.159
1800	1	.783	0.31	-0.127

Measurements of the wall friction forces were made; the effective Fanning friction factor was estimated to be $f = 0.0040$. Measurements of the rate of evaporation were made by direct use of the vapor sampling probe and by interpretation of static pressure changes. The highest evaporation rates occurred in the period of acceleration of the liquid to gas velocity which occurred in the first three feet of the evaporation section. Only small evaporation rates occurred in the last three feet of the evaporation section.

Transitions from subsonic to supersonic flow in the constant area test section were observed when initial mach number values were sufficiently high.

Interpretations of the experimentally observed results are given, based upon theoretical analyses of the overall aerothermopressor process and the liquid drop evaporation process which are presented in the Appendices.

Extrapolations of the small-scale experimental results are made. It is concluded that stagnation pressure ratios significantly greater than unity can be obtained in large-scale aerothermopressors. Appreciable improvements in the specific power output and thermal efficiencies of simple gas turbine power plants should, therefore, be possible with the application of aerothermopressors.

Thesis Supervisor: Ascher H. Shapiro
Title: Professor of Mechanical Engineering

Table of Contents

I. Introduction

The name "aerothermopressor" has been given to a device which is designed to produce an increase in the stagnation pressure of a high-velocity, high-temperature gas stream by the evaporative cooling effect of injected liquid. The possibility of achieving an increase of stagnation pressure of a gas stream by this method was first discussed by Shapiro and Hawthorne (1)*. They showed that the stagnation pressure of a gas stream might be increased by reducing the stagnation temperature. By making use of Reynold's analogy between heat and momentum transfer, they further showed that this increase in stagnation pressure could not be achieved if heat transfer surfaces were utilized to reduce the stagnation temperature since the corresponding detrimental friction effects would offset the beneficial cooling effects--resulting in a net loss of stagnation pressure. Shapiro and Hawthorne concluded that a rise in stagnation pressure could be achieved only if the decrease in stagnation temperature were accomplished by evaporative cooling. Water was recognized as an ideal liquid for this purpose since, in addition to being plentiful, it has an extremely high latent heat of vaporization.

The first application of this device to be investigated was in connection with a theoretical survey of supersonic wind tunnel propulsion systems (10). The magnitudes of stagnation pressure ratios which appeared feasible in this study were not sufficiently large to justify development for wind tunnel application. The idea was then advanced that the aerothermopressor might be used to improve the thermal efficiencies and power outputs of simple gas-turbine stationary and marine power plants. In this connection, the

---

* Numbers in parentheses refer to the bibliography.

aerothermopressor appears to possess significant promise. The aerothermopressor would perform a function in the gas turbine plant which, in a sense, is analogous to the function of the condenser in the steam power plant. The high temperature gases which issue from the expansion turbine would be expanded to high velocities in the nozzle of the aerothermopressor; liquid would be injected into the stream; and, after evaporative cooling, the resulting stream would pass through a diffuser to be exhausted into the atmosphere. Since the aerothermopressor would provide an overall stagnation pressure rise from the inlet of the nozzle to the exhaust from the diffuser, the exhaust pressure of the turbine could be reduced to values below atmospheric. As a consequence, the thermal efficiency and the net power output of a plant of given size would be improved by the aerothermopressor.

An analysis of the flow within the aerothermopressor (see Appendix A) indicates that (i) the successful performance of the aerothermopressor is a function of the size (diameter) of the evaporation section since the stagnation pressure increases due to liquid evaporation but decreases due to wall friction and liquid drag effects, and (ii) the potential performance of the aerothermopressor is better at supersonic gas speeds than at subsonic gas speeds. It may, therefore, be concluded that a successful aerothermopressor will probably be a large-scale, high-velocity device.

Some small scale experiments on constant-area supersonic aerothermopressors have been conducted by Templeton and Wish (3) and Gisvold and Matheson (4). Generally speaking, these experiments were in the nature of gambles on achieving a stagnation pressure rise with simple, small-scale equipment. Although increases in stagnation pressure were not achieved, much valuable information on the general nature of the aerothermopressor process was gained from these experiments.

More detailed analyses of the aerothermopressor process, particularly of the liquid drop formation and distribution (7) and the drop evaporation process (Appendix D), have been carried out since these experiments were performed. These analyses indicate that the problems associated with the development of a supersonic aerothermopressor are far more difficult to solve than those associated with the development of a subsonic aerothermopressor, and that much more elaborate instrumentation than had been used previously would be necessary to study the complex aerothermopressor process.

These findings led to the decision to concentrate on the construction of a small-scale aerothermopressor with a subsonic nozzle at the entrance to the evaporation section. The device was to be sufficiently well-instrumented to gain a better understanding of the many complex processes which occur in the aerothermopressor than had been obtained in previous work. When the decision was made, the subsonic aerothermopressor was thought to be one in which a subsonic flow was produced at the entrance to the constant-area evaporation section and maintained at subsonic levels throughout the process. During the course of this experimental work, however, it was discovered that transition from subsonic to supersonic flow in a constant-area duct is made possible by certain phenomena associated with the liquid drag and evaporation processes. The distinction between a subsonic and supersonic aerothermopressor thus depends upon the character of the entire process--not only upon the velocity of the gas flow which enters the evaporation section.

The aerothermopressor used in this work consisted of a bellmouth entrance nozzle, a constant area evaporation section, and a diffuser. To supplement the interpretation of the liquid evaporation processes by means of static pressure measurements, a special vapor sampling probe was also developed. This probe permitted the removal of a sample of the vapor from the liquid-vapor mixture in the evaporation section, the water content of which was measured by means of a specially-designed dew point apparatus.

It should be emphasized that the purpose of the work was to obtain fundamental data which would contribute to a better understanding of the complex aerothermopressor process and consequently permit a more rational design of a large-scale aerothermopressor. It was recognized from the outset of this work that the scale of the test apparatus was too small to produce a net increase in stagnation pressure.

II Test Apparatus, Instrumentation, and Calibration

A. Main Test Equipment

All test work was carried out in the Gas Turbine Laboratory of the Massachusetts Institute of Technology.

The main test equipment which was used in this experimental work is shown in the schematic diagram, Figure 1. The aerothermopressor itself consisted of a bellmouth entrance nozzle, a straight constant-area evaporation section, 73 1/4 inches long and 2 1/8 inches in diameter, and a diffuser of six degrees total included angle which diffused the flow to standard six inch pipe. The evaporation section was made of heavy wall type 321 stainless steel tubing in two lengths, each three feet long. The inside wall was honed to provide smooth wall conditions. The bellmouth was machined in a type 321 stainless steel block welded to one end of the test section. The diffuser was rolled from type 321 stainless steel sheet 1/8 inch thick. Since there was a constant area section 1 1/4 inches long at the entrance portion of the diffuser, the total length of the constant area evaporation section 73 1/4 inches.

Twenty static pressure taps of 0.030 inch diameter were spaced along the length of the evaporation section as shown. These taps and two pitot-static tubes, located 15 1/2 inches upstream from the entrance to the bellmouth nozzle and 8 3/4 inches downstream from the exit of the diffuser, were connected to a mercury manometer board to permit measurement of pressure distribution throughout the apparatus.

The constant area evaporation section was also fitted with eight access ports to permit the use of special sampling probes and any other special instrumentation. The probes were inserted in these access ports through plugs of the type shown in Figure 2. Blind plugs shaped to fit the inside contour of the circular evaporation section were fitted to the access ports when no probes were in use.

The initial stagnation temperature of the gas T_o was measured 12 inches upstream from the entrance of bellmouth nozzle by means of a five-shielded, chromel-alumel thermocouple probe manufactured by the Airflo Instrument Company. A Leeds and Northrup K2 potentiometer was used for this and other temperature measurements.

The steam ejector of the Gas Turbine Laboratory provided the suction necessary to run the aerothermopressor tests. Atmospheric air was drawn into the apparatus through a specially constructed gas-heating furnace. The furnace, which was constructed by the Etter Engineering Company, utilized an Eclipse NHE burner No. 5 as the primary heating burner and an Eclipse Walltite LEA-9 burner No. 3 as the pilot burner. Excellent temperature control was achieved by regulating the primary combustion air by means of a large butterfly valve and a small bypass valve located between the air blower and the gas burners.

Various water injection nozzles were held at the center of the stream at the bellmouth nozzle by a suspension apparatus located upstream from the bellmouth. Radial water injection nozzles were also located 3/8 inch and 10 3/4 inches downstream from the entrance of the constant-area evaporation section. The water flow rates were measured by means of a Schutte and Koerting No. 3A rotameter, a Schutte and Koerting No. 4B rotameter, a modified Fischer and Porter No. D4 rotameter, or a special calibrated orifice, depending upon the mass rate of flow being used. For most nozzles city water pressure was sufficiently high, but, for those which required high pressures, a Burks turbine pump Model 75 E16 was used. The water flow was controlled by means of a pressure regulating valve and a needle valve.

The hot gases emerging from the aerothermopressor passed into a large quench tank in which cooling water was sprayed. The cooled gases then passed through a standard 6 inch valve to the main stream ejector line. This valve provided control of the mass rate of flow of gas through the system. Liquid water which accumulated in the quench tank was exhausted by means of a Pemberthy XL-96 No. 2 steam ejector.

Except for flow conditions at the high initial mach numbers just slightly below choking values, steady-state conditions were easily achieved. Under these steady-state conditions pressure measurements were made to within an accuracy of less than one millimeter; water flow measurements to an accuracy of 0.002 lb per second. Inlet stagnation temperature as indicated by the thermocouple were easily held to within 5 degrees Fahrenheit. The measurements of initial mach number and air flow rate were subject to greater error; these errors are discussed in the following section B.

At choked flow conditions, all measurements were accomplished equally well except that there were large pressure fluctuations in that portion of the evaporation section in which the shock fluctuated.

Almost all test work was carried out at inlet stagnation pressures corresponding to the slight drop in pressure from the atmosphere through the gas furnace and inlet piping. For the few tests run at lower pressure loads, a "jury-rigged" throttle valve, consisting of a stainless steel sheet inserted between flanges in the pipe between the furnace and the aerothermopressor, was used.

B. Measurement of Initial Mach Number and Mass Rate of Flow of Gas

The bellmouth nozzle at the entrance of the aerothermopressor evaporation section (Figure 1) was used for flow measurement as well as for the acceleration of the gas stream.

The initial mach number and the mass rate of flow of gas were computed under the assumption that the flow through the nozzle was one-dimensional and isentropic. The isentropic relations of the Gas Tables (9) were used since the variation of specific heat with temperature is appreciable at the temperature levels used in the experimental work.

It was found during the initial experimental work that the flow through the bellmouth nozzle was evidently three-dimensional in character since pressure depressions were observed at the location of the throat pressure tap. The presence of the various liquid injection nozzles was also found to disturb the entering gas flow with a variable effect on the pressure depression depending upon the injection nozzle used.

Since simple one-dimensional isentropic flow relations were used to predict the velocity and mass rate of flow from the measured inlet stagnation temperature and pressure and the static pressure at the exit of the nozzle, it was necessary to correct the measurements for the observed depression. It was not possible to rely upon the next static pressure measurement two inches downstream from the nozzle exit because, in most tests, water was injected at the nozzle exit plane. The resulting drag of the water had a marked influence on the static pressure at all locations downstream from the plane of injection.

The correction to the pressure measurement at the nozzle exit tap was obtained from a series of tests in which the pressure variation along the constant-area section was measured. The "corrected" inlet pressures p_1 were then obtained by a simple extrapolation of these data. The plots of Figure 3 are typical of the pressure variations which were measured and the extrapolations which were made. It was possible to run these tests with no liquid injection at the nozzle exit plane up to initial mach numbers which were higher than those corresponding to choked flow with no water injection. This was accomplished by injecting liquid through the radial injection nozzles at a position 10 3/4 inches downstream from the exit plane of the aerothermopressor nozzle.

As would be expected, the ratio of the normalized pressure drop through the nozzle for the corrected value of $p_1, \left(\frac{p_{01} - p_1}{p_{01}}\right)_{corr}$, to the value for the measured value of $p_1, \left(\frac{p_{01} - p_1}{p_{01}}\right)_{meas}$, was found to be a linear function of the square of the initial mach number M_1^2, as shown in Figures 4, 5 and 6. The water injection nozzles which were used are described in Table 1. The curves of Figure 4 show that for each liquid injection nozzle this correction factor is independent of temperature and pressure level within the order of accuracy of the measurements and extrapolations.

For convenience in computing values of the initial mach number and mass rate of flow of gas, the correction factor $\left(\frac{p_{01} - p_1}{p_{01}}\right)_{corr} \div \left(\frac{p_{01} - p_1}{p_{01}}\right)_{meas}$ was plotted as a function of $\left(\frac{p_{01} - p_1}{p_{01}}\right)_{meas}$ as shown in Figure 7.

In the range of initial mach numbers tested, the correction factor may be in error by as much as 10 to 12% but the resulting errors in predicted mach number and mass rate of flow are considerably less—about 1% in the range of initial mach numbers used.

C. Humidity-Measuring Instruments and Calibration

1. Statement of the Problem

The theoretical analysis of Appendix B shows that it is necessary to measure at least two independent properties of the flow to determine the state of the liquid-vapor mixture at any cross-section of the aerothermopressor. In previous experimental work (3, 4) only the static pressure of the stream was measured, and the actual state was inferred only on the basis of certain assumptions regarding the value of the wall friction forces. Accordingly, in this experimental work it was decided to attempt to measure at least one other property in addition to the static pressure.

The difficulties in measuring the total or stagnation pressure of the stream when liquid droplets are present is apparent. No attempts were made to develop a satisfactory total pressure probe sufficiently early in this work although development of a stagnation pressure probe by other workers is in progress at the time of this writing.

For this work, efforts were concentrated on the development of a suitable method of measuring the water vapor content of the gas stream at several cross-sections of the evaporation section. The problem of measuring the humidity of the liquid vapor mixture was reduced to (i) withdrawing a true sample of the gas phase of the two-phase flow, and (ii) measuring the water vapor content of this sample.

2. Sampling Probes

It is difficult to withdraw a sample of the gas phase since the liquid droplets are so small that they may easily follow the direction of the gas streams. Furthermore, any liquid which impinges upon the probe may very likely run into the sampling holes. Two vapor-sampling probes ("humidity probes") were built which incorporated features which overcame these difficulties to a large degree. The probes are shown in figures 8 and 9.

The sampling hole of each probe was inclined away from the direction of flow of the main stream in an attempt to provide a small radius of curvature of the streamlines of the incoming sample stream. With this small radius of curvature, it was hoped that most of the liquid droplets, particularly the larger ones, would be thrown off.

The sampling hole of each probe was also prevented from taking in liquid water which impinged on the probe by a boundary layer suction port. In probe I, this hole was provided only on the upstream side of the sampling hole, while in probe II, the boundary layer suction port was an annulus which surrounded the sampling hole.

Eight access ports were provided along the length of the evaporation section of the experimental aerothermopressor (Figure 1). The humidity probes were held in these access ports by means of special glands the details of which are shown in Figure 2. Each probe was traversed across the stream by loosening the gland screws and sliding the probe in its gland guide.

3. Apparatus for Measuring Humidity of Sample Stream

A special apparatus was constructed to provide suction for the boundary layer and sample ports of the sampling probes and to provide a means for measuring the water vapor content of the sample stream. The detailed design, construction and test of this apparatus formed the subject of another thesis (5).

A schematic diagram of this device is shown in Figure 10. Briefly, an ejector operated by compressed air provided a controlled suction pressure for the boundary layer port. The boundary layer stream which was withdrawn was passed through a boiling water heat exchanger to insure that all the liquid present was vaporized. The mass rate of flow of this stream was measured by a small converging nozzle placed between the heat exchanger and the suction ejector.

Another ejector operated by compressed air provided suction for the sampling port. The sample stream was passed successively through a heated line, boiling water heat exchanger, flow-measuring nozzle, controlled temperature heat exchanger, water jacketed "Dewcel" chamber, and the suction ejector.

The dew point temperature of the sample stream was measured by a Dewcel, a commercial instrument manufactured by the Foxboro Instrument Company which is calibrated by means of data on the equilibrium of lithium-chloride and water at various temperatures. The dew point thus measured and the pressure within the Dewcel chamber gives the value of the specific humidity ω of the sample stream through the familiar relation

$$\omega = \frac{W_s}{W_a} \quad \frac{p_g}{p - p_g} \quad ,$$

where p_g is the saturation pressure corresponding to the dew point temperature and p is the pressure in the Dewcel chamber.

4. Calibration of Sampling Probes

In Reference 5, Larson shows that the humidity measurements taken by the humidity-measuring apparatus shown in Figure 10 ~~is~~ are accurate to within 3%

To test the ability of the sampling probes to remove the gas phase of the liquid-vapor mixture, each probe was tested under rather severe conditions. With the probe located in the center of the gas stream at the last access port located 67.5 inches from the injection plane (Figure 1), the aerothermopressor was operated cold (little or no evaporation) at an initial mach number of about 0.5 and with liquid water injection through nozzle no. 3 (Table 1).

When the aerothermopressor was operated with an initial stagnation temperature T_{01} corresponding to atmospheric temperature (approximately 60F) and with an initial injection rate ω_0 of approximately 0.2 lb water per lb air, readings of dew point temperature could not be observed over a wide range of boundary layer and sample suction flow rates. The dew points under these conditions were below the lowest available dew point thermometer reading of about 45°F. Only when no boundary layer flow rate was used were dew point temperatures observed; these were extremely erratic since liquid water was sucked in under this condition.

Each probe was then tested at the same location with only the pilot burner of the aerothermopressor gas burner lighted. Inlet stagnation temperature T_{01} under these conditions varied from about 120 to 133°F. The results of these tests are shown in Figures 11 through 16.

The results of tests of probe I (Figure 8) showing the effects of varying the sample flow rate and the boundary layer flow rate are shown in Figure 11. In this series of tests the inlet stagnation temperature T_{01}, stagnation pressure p_{01}, mach number M_1, and injection rate ω_0 were held constant. While the sample flow rate was held constant at about 7.2 to 7.3 (10^{-4}) lb/sec, the boundary layer flow rate was varied for zero to 12.3 (10^{-4}) lb/sec. At values of the boundary layer flow above about 6 (10^{-4}) lb/sec there was no trend in the variation of measured specific humidity indicating that little or none of the liquid impinging on the probe was permitted to enter the sampling hole. At lower values of the boundary layer flow, however, the measured specific humidity was much higher, indicating that some liquid which impinged on the probe was permitted to enter the sampling hole.

While the boundary layer flow was held approximately constant at 10.8 to 11.5 (10^{-4}) lb/sec, the sample flow rate was varied from 4.3 to 7.6 (10^{-4}) lb/sec. Higher values of the sample flow could not be obtained since the flow was choked at about 7.6 (10^{-4}) lb/sec. At values of the sample flow above about 6 (10^{-4}) lb/sec there was no trend in the variation of the measured specific humidity, indicating that liquid droplets were effectively thrown away from the incoming sample stream, while at sample flow rates below 6 (10^{-4}) lb/sec, the opposite was the case.

The results shown in Figure 11 were taken to indicate that sampling probe I operated quite effectively when boundary layer and sample flow rates were each maintained above 6 (10^{-4}) lb/sec.

Operating with these favorable sample and boundary layer flow rates, probe I was then tested at different values of initial injection rate for the same inlet stagnation state and mach number. The results of these tests are shown in Figure 12. The value of the specific humidity of about 0.016 lb water per lb air measured when no liquid was being injected corresponded to the value of the water vapor content of the outside atmosphere plus the water formed in the combustion in the pilot burner. Although when liquid was injected there was additional water evaporated into the gas stream passing through the aerothermopressor, it is unlikely that this evaporated water accounted entirely for the rise in measured specific humidity with injection rate shown in Figure 12.

It may be seen that some water evaporated during these tests from the data plotted in Figure 13. The observed values of the ratio of the static pressure at the probe location to the initial stagnation pressure $\frac{p}{p_{01}}$ are plotted against the water injection rate. Also plotted are the results of discontinuity calculations (Appendix B and Reference 2) for the case of no evaporation and for various values of the wall friction term $f \frac{L}{D}$. The difference in slope between the experimentally observed data and the results of the calculations indicates that evaporation took place, since the static pressure increases as a result of evaporation (Table 2).

The dew point temperature variation of the aerothermopressor stream at the probe location based upon the measured specific humidity (Figure 12) and the observed static pressure (Figure 13) is plotted as a function of the initial injection rate in Figure 14. Also plotted is the stream temperature predicted from the discontinuity analysis for the case of no evaporation and with the wall friction term $f \frac{L}{D} = 0.10$. Since evaporation would lower this predicted temperature still more, it is obvious from the comparison of these two curves that a very small amount of liquid water was taken in with the sample stream--particularly at the higher injection rates.

The maximum amount of liquid drawn in with the sample stream at the highest injection rates was probably no greater than about 7% of the initial injection rate. Since the probe was mostly used to withdraw samples in the high-temperature runs at cross-sections were most of the liquid was evaporated, this error was neglected in interpreting the data taken at high temperature levels.

Sampling probe II (Figure 9) was subjected to a series of tests similar to that described for probe I. The results of the tests in which the sample flow rate and boundary layer flow rate were varied independently are shown in Figure 15. In this case no definite limiting flow rates of the nature found for probe I were evident. Furthermore, for probe II, the suction vacuum necessary for any given flow rate were found to be much higher than those for probe I and, as a result, the pressures measured in the Dewcel chamber were extremely low. Greater errors in prediction of the specific humidity from the measured Dewcel chamber pressure and dew point temperature were, therefore, possible with probe II. Time limitations prevented a satisfactory exploration of the flow phenomena observed with probe II. Nevertheless, the results of the tests of probe II at various initial injection rates which are shown in Figure 16 indicate good agreement with the results for probe I (Figure 12). Difficulties were also experienced with short circuits in the thermocouples located in the vapor-sampling probes. Time limitations prevented the repair of these special devices. As a result, no reliable temperature measurements were obtained with these probes.

III Discussion of Experimental Results and Comparison with Theory

A. Interpretation of the General Effects of Water Injection and Evaporation on Pressure Distribution in Evaporation Section

1. Use of Theoretical Analysis

The static pressure distributions along the evaporation section which have been measured for various combinations of values of initial parameters are helpful in interpreting the effects of water injection, water evaporation and wall friction on the flow. The table of influence coefficients, Table 2, which results from a theoretical analysis of the aerothermopressor flow (Appendix A), permits the formulation of the following table of qualitative effects on static pressure and mach number changes:

	Static pressure, p	Mach number, M
Subsonic Flow ($M < 1$)		
Liquid evaporation (cooling) causes	increase	decrease
Liquid drag and wall friction cause	decrease	increase
Supersonic Flow ($M > 1$)		
Liquid evaporation (cooling) causes	decrease	increase
Liquid drag and wall friction cause	increase	decrease

With the measured pressure distributions and the above table a good picture of the nature of the aerothermopressor process may be formulated.

2. Effects of Liquid Injection for Processes with Low and High Stagnation Temperature

In Figure 17 are plotted the static pressure distributions along the length of the evaporation section which were measured in tests conducted at essentially constant initial mach number M_1 and with three water injection rates ω_0 and two initial values of the stagnation temperature T_0.

The curves labelled A0 and B0 are for runs with no liquid injection at initial stagnation temperatures of 530 R and 1500 R respectively. Since the flow was subsonic, in these tests the static pressure decreased in accordance with the well-known Fanno line interpretation. The mach number, of course, increased along the test section. The low temperature curve A0 lies above the high temperature curve B0 because (i) the initial mach number M_1 ~~is~~ was slightly lower and (ii) because the wall friction factor f was smaller since the Reynolds number for the cold flow was higher.

Curves A2 and A3 represent the pressure distributions which were obtained for increasing values of the water injection rate at low temperatures. Since little or no liquid was evaporated in these runs, the pressure drops were greater since the drag of the liquid added to the wall friction effects. The increases in mach number along the evaporation section were accordingly larger; in fact, the curve marked A3 corresponds very closely to the choked flow condition.

Comparison of curves B1 and B2 with curves A1 and A2 shows that the injection of water at the high initial stagnation temperature of 1500 R had quite the opposite effect. In these runs the evaporation of water was appreciable and consequently the pressure drops were less than for the corresponding test with no liquid injection. The mach number changes were undoubtedly also much smaller than for the runs with no liquid injection at high temperature.

3. Effects of Varying the Water Injection Rate in Processes at High Initial Stagnation Temperature

The pressure changes at high temperature levels caused by the combined effects of wall friction, water injection, and water evaporation shown by curves B0, B1 and B2 of figure 17 are more pronounced at higher values of the initial mach number. In Figure 18 are plotted static pressure distribution curves corresponding to various liquid injection rates which were measured in tests at an initial Mach number $M_1 = 0.65$ and at an initial stagnation temperature $T_{01} = 1500$ R. Since the initial mach number corresponding to choked flow with no liquid injection was below 0.65, no curve corresponding to a dry run is shown in this figure.

For each constant value of the injection rate, the following characteristic divisions in the overall process should be noted:

a) The static pressure immediately following injection decreased rapidly since the liquid drag forces were predominate.

b) Following this drop in pressure there was a rapid rise in pressure corresponding to the rapid evaporation of liquid during the "turbulent" portion of the evaporation process--where there existed large differences between the liquid and gas velocities. The evaporation effects were predominate over the drag and wall friction effects during this portion of the process.

c) After the liquid was accelerated to velocities nearly equal to the gas velocities, the evaporation rate decreased in the "laminar" portion of the evaporation process, since the heat transfer coefficients were smaller and the temperature differences were lower. Consequently, the wall friction drag became controlling, and the pressure again began to decrease.

The curves of Figure 18 also show that there existed an optimum injection rate between $\omega_0 = 0.21$ and 0.31. Above this optimum injection rate drag effects caused by added liquid injection offset the evaporation effects, since the gas temperatures dropped to near-saturation values. The optimum value of the injection rate is discussed more fully in section III C.

4. Transition from Subsonic to Supersonic Flow in the Constant Area Evaporation Section

The combined effects of wall friction, water injection drag, and water evaporation at high temperature levels permit a transition from subsonic to supersonic flow in the constant area evaporation section of the aerothermopressor. This curious phenomenon is illustrated by the pressure distribution curves of Figure 19 which were measured in tests at a constant initial stagnation temperature $T_{01} = 1500$ R and a constant injection rate $\omega_0 = 0.21$ lb water per lb air.

The curves of Figure 19 which correspond to initial mach number values of 0.48 and 0.65 are very similar to the curves of Figure 18, differing only in that the magnitudes of the pressure changes increase rapidly with mach number. The initial pressure drops associated with predominate liquid evaporation, the following pressure increases associated with predominate liquid evaporation, and the final pressure drops associated with predominate wall friction were evident in these experiments.

Although the corresponding values of the mach number could not be measured, it may be assumed that the mach number first increased when liquid drag was predominate, then decreased when evaporation was predominate, and finally increased again when wall friction was predominate. The value of the mach number therefore passed through a maximum when the liquid evaporation first became predominate. As the initial mach number of the stream was increased, this maximum mach number value increased until it reached the critical value of unity. This condition occurred in the experiments of Figure 19 when the value of the initial mach number was increased to 0.78. The mass rate of flow reached ~~at~~ a maximum at this condition since the flow was choked when the local mach number was equal to unity. No further increases in initial mach number or flow rate by lowering the back pressure p_{03} were possible.

For the choked flow corresponding to the curve marked 1 in Figure 19, the pressure first decreased and the mach number increased because the liquid drag was predominate in the subsonic flow. The critical condition was reached when the mach number became equal to unity at a point about three or four inches from the injection plane. At this condition, the evaporation became predominate; the pressure continued to decrease, and the mach number continued to increase—corresponding to the predominate effect of evaporation in supersonic flow. At a distance of about 33 inches from the plane of injection, the wall friction became predominate, the rate of evaporation having decreased, and there followed a pressure increase and mach number decrease corresponding to the influence of wall friction in supersonic flow. A shock to subsonic flow followed at about 55 inches, and then, with wall friction predominate, the pressure decreased and the mach number increased to unity at the exit of the constant area section. The flow in the diffuser section became supersonic and shocked to subsonic at a mach number and location corresponding to the value of the back pressure at the points labelled 2, 3 or 4. The back pressure corresponding to the point labelled 4 was that limiting value which corresponded to subsonic flow throughout the diffuser from a mach number of unity at the entrance to the diffuser.

As the back pressure was increased above that corresponding to point 4, the shock moved forward in the evaporation section and the typical pressure distribution curves labelled 5, 6 and 7 were obtained. The values of the mach number at the entrance to the diffuser corresponding to these curves were, of course, less than unity.

It was found impossible to adjust the flow to move the shock any closer to the injection plane than that indicated by the curve labelled 8. As the back pressure was increased slightly above that corresponding to the point labelled 9, the entire flow became very unsteady. Small variations in initial conditions then caused large unsteady surges in pressure and flow rate.

For an initial stagnation temperature of 1500 R, and injection rates below about 0.14 lb water per lb air, it was impossible to reach a mach number of unity at any point other than the exit of the constant-area evaporation section.

At low water injection rates, the liquid drag was not sufficient to cause the mach number to increase to unity in the constant-area evaporation section.

B. Experimental Determination of the Optimum Water Injection Nozzle

The design of the water injection nozzles is a critical portion of the overall design of the aerothermopressor since the overall performance of the aerothermopressor is dependent upon achieving maximum water evaporation rates in minimum lengths of evaporation section. The injection nozzle design must therefore satisfy the following two major requirements:

1) The diameter of the liquid droplets produced by the injection nozzles should be as uniformly small as possible. The drop evaporation equations D11 and D13 of Appendix D indicate that the rate of evaporation is inversely proportional to the square of the droplet diameter ($\frac{d}{dt} \sim d^{-2}$) during the laminar or molecular evaporation regime and inversely proportional to five-thirds power of the droplet diameter ($\frac{d}{dt} \sim d^{-\frac{5}{3}}$) during the turbulent portion of the evaporation regime.
2) The liquid droplets should be dispersed as uniformly as possible throughout the gas phase to avoid localized regions of high concentrations of water vapor and liquid which tend to reduce the overall rate of evaporation. This requirement also implies that minimum liquid impingement upon the walls of the aerothermopressor is desirable.

The drop-formation studies of Nukiyama and Tanasawa (8) and of Plender (7) indicate that air-atomization techniques are very effective in producing liquid sprays of very small drop size. Since the main gas stream of the aerothermopressor provided in itself the high velocity gas necessary for this type of atomization, it was felt that the best nozzle designs would result if air atomization was utilized, with the main gas stream serving as the primary source of air.

A major portion of the experimental program was devoted to the determination of the most satisfactory nozzle design for use in the small scale aerothermopressor. Since no direct measuring techniques were available to measure the drop size and distribution, the determination of water injection nozzle performance was based upon the best overall performance of the entire aerothermopressor process.

An overall performance coefficient was defined using as its basis the controlling differential equations for an infinitesmal portion of the aerothermopressor process developed in Appendix A. The differential equation for the change in stagnation pressure may be written as

$$\frac{dp_0}{p_0 M^2} = d\,Y - 2kf\,\frac{dL}{D} ,$$

where the term dY represents all terms which take into account the acceleration and evaporation of the liquid water. Since the objective of the aerothermopressor is to achieve an overall rise in stagnation pressure (that is--to make the liquid injection and evaporation terms outweigh the wall friction term in the integrated form of this equation), the measured overall rise in stagnation pressure, normalized as indicated by the form of this equation, was used as a criterion of aerothermopressor performance. The performance coefficient was therefore defined as $\frac{p_{03} - p_{01}}{p_{01}\,M_1^2}$, where the stagnation pressure p_{01} was measured at the entrance to the nozzle, the stagnation pressure p_{03} was measured at the exit of the diffuser, and the initial mach number M_1 was measured at the entrance of the evaporation section.

The following experimental procedure was used in evaluating the performance of the water injection nozzles:

a) For a constant initial stagnation temperature $T_{01} = 1500$ R, a constant initial stagnation pressure value of ~~constant~~ $p_{01} = 14.7$ psia (approximately) and for several values of the initial mach number M_1, the variations in the overall aerothermopressor performance coefficient $\frac{p_{03} - p_{01}}{p_{01}\, M_1^2}$ with initial injection rate ω_0 were determined. In Figure 20 are shown typical curves of performance coefficient versus initial injection rate determined in this manner.

b) The optimum values of the performance coefficients at each initial mach number were taken from curves similar to those of Figure 20 and plotted as functions of initial mach number M_1 (Figure 21). The highest indicated values of the initial mach number for those nozzles tested at more than one mach number are those mach numbers corresponding to choked flow conditions. The corresponding values of the optimum performance coefficient are those in which the choked condition was located as far upstream in the evaporation section as it was possible to obtain under steady operating conditions (see Section III A).

The curves of Figure 21 therefore represent the optimum performance obtained with twenty different water injection nozzle schemes. Each nozzle is identified in Table 1.

The nozzles fall into four broad categories:

i) axial flow jets (numbers 1, 3, 4, 5, 6, 18, 19, 20);
ii) radial jets located in the test section wall (numbers 7, 8, 11);
iii) water sheet formation nozzles (numbers 2, 16); and
iv) combinations of the preceding categories (numbers 9, 10, 12, 13, 14, 15, 18).

Based upon preliminary cold tests using the transparent test section of Plender (7), it was found that the radial flow jet nozzles (ii) and the water sheet nozzles (iii) produced smaller drop sizes, at least near the point of injection, than the axial flow jets (i). On the other hand, the distribution of water in the cross-section achieved by the axial flow jets (i) was essentially independent of the water-air ratios while the reverse was the case for the other nozzles (ii, iii). There was also some evidence that the final break-up into small droplets of the streams from the axial flow nozzles was probably about as complete as that achieved by the other nozzles, although this final break-up did occur at a greater distance from the point of injection.

The curves of Figure 21 definitely indicate that the performance of the multi-axial jet nozzle No. 3 was at least equal to if not better than that of any other nozzle tested. It was also felt that the multi-axial jet nozzle could be more easily adapted to large scale aerothermopressors than the other types. Nozzle No. 3 was therefore selected as the optimum design, and all further experimental work was carried out using this nozzle.

It should also be noted that a comparison of the performance of nozzles numbers 3 and 20 indicates that the advantages of smaller drop size formation and better distribution associated with higher air velocities at the beginning of the constant-area evaporation section (no. 3) more than outweigh the reduced drag effects associated with locating the same injection nozzle upstream of this section (no. 20).

C. Variation of Overall Aerothermopressor Performance with Initial Mach Number, Initial Stagnation Temperature, Initial Stagnation Pressure, and Initial Injection Rate.

Using the normalized overall stagnation pressure rise $\frac{p_{03} - p_{01}}{p_{01} \quad M_1^2}$ (Section III B) as the single criterion of aerothermopressor performance, tests were made to determine the variation in performance with certain initial parameters. In all of these tests, water injection nozzle no. 3 was used. As expected, in no tests of the small-scale aerothermopressor was there a net size in stagnation pressure since in the small diameter D = 2 1/8 inches, the wall friction forces were too high.

1. Variation in Performance with Initial Injection Rate

The curves of Figure 20 are typical of the variation in overall performance achieved when the water injection rate was varied with the initial stagnation state and the initial mach number held constant. For each set of initial conditions there was found to be an optimum injection rate at which the beneficial effects of the evaporation of liquid were best utilized in offsetting detrimental effects of drag due to injection of the water and the wall friction forces. At injection rates above the optimum, the drag effects caused by the added liquid injection offset any additional evaporative effects since the gas stream saturation conditions limited the amount of water which could be evaporated.

For a fixed initial stagnation state, the optimum injection rate was found to be quite insensitive to initial mach number, varying only about 0.03 lb water per lb air for the range of mach numbers tested (see legend, Figure 22). No definite trend with mach number was observed within the accuracies of the measurements.

2. Variation of Performance with Initial Stagnation Temperature

The experimental results plotted in Figure 20 indicate that at a fixed low value of the injection rate, the aerothermopressor performance was superior for the lower initial stagnation temperatures, while at a fixed high value of the injection rate, this behavior was reserved. The initial stagnation pressure and initial mach number were held constant for these comparisons.

At low values of the injection rate, practically all of the injected water was evaporated (see Section III E) at any of the stagnation temperatures of 1200 R or above. The overall performance was thus dependent upon the variation of the wall friction forces with temperature. The equations of Appendix B may be combined to show this variation in the following equation:

$$\tau \sim f\ p\ M^2$$

Since the Reynolds numbers were larger for the lower temperature runs, the friction factors f were smaller and, consequently, the wall shear forces were smaller for the low temperature runs.

At the high injection rates on the other hand, the fraction evaporated depended to a great extent upon the initial stagnation temperature. The higher temperature differences caused a higher rate of evaporation and the resulting high evaporation outweighed the higher wall friction forces.

For the same reason, the optimum performance, corresponding to the optimum injection rates, increased with initial stagnation temperature. The optimum performance variation with initial stagnation temperature may be seen in Figure 22.

3. Variation of Performance with Initial Stagnation Pressure

The curves of Figures 20 and 22 also illustrate the effects of varying initial stagnation pressure on the overall aerothermopressor performance. For the small-scale aerothermopressor tested, the performance decreased with decreasing initial stagnation pressure. This behavior may be explained by referring to the measured pressure distribution curves of Figure 23 which illustrate the influence of pressure levels on evaporation rates. Unfortunately, the values of the initial mach number and injection rates were not quite the same for the two tests. It may be seen, however, that the rise of pressure corresponding to the turbulent evaporation period was more gradual for the run at lower stagnation pressure which infers that the rate of evaporation was lower. This behavior is to be expected since the Reynolds number was smaller for the low pressure run and, consequently, the heat transfer coefficients were probably smaller. Although the stay time of the droplets in the turbulent portion of the evaporation regime was higher since the acceleration was smaller (Equation D15) and although the wall friction effects were lower, these effects were apparently overshadowed by the low rate of heat transfer.

In large scale aerothermopressors, where wall friction effects become comparatively unimportant, the reverse effect may occur as the pressure level is reduced. The evaporation sections may be sufficiently long to take advantage of the evaporation during the laminar region of evaporation. As the pressure level is reduced, the water content of the gas stream corresponding to saturation at any given temperature is increased. The overall performance of the large scale devices may therefore be superior at low pressure levels. Time limitations prevented a more effective study of pressure level effects in this work.

4. Variation of Performance with Initial Mach Number

In Figure 22 the effect of variation of initial mach number on overall aerothermopressor performance is illustrated. The values of optimum aerothermopressor performance coefficient $\left(\frac{p_{03} - p_{01}}{p_{01}\, M_1^2}\right)_{opt}$ plotted in this figure were obtained from the optimum points of the curve of Figure 20 and similar plots for other values of the initial mach number. The highest values of the initial mach number for each curve of Figure 22 correspond to choked flow conditions. The corresponding values of the performance coefficient are the values obtained when the shocks from supersonic to subsonic flow were maintained as far upstream in the evaporation section as was consistent with steady operation (Section III A).

Fortunately, (since large scale aerothermopressors are envisioned as high velocity devices) the performance of this small-scale aerothermopressor was found to improve with increasing values of the initial mach number. In Section III D it is shown that the fraction of water evaporated was increased with initial mach number. Although detrimental liquid drag and wall friction effects also increased with initial mach number, the evaporation rate was controlling so that an increase in performance with initial mach number was measured.

It should be noted that the stagnation pressure ratio for optimum conditions $\left(\frac{p_{03}}{p_{01}}\right)_{opt}$ actually decreased with initial mach number M_1. As the scale of the aerothermopressor is increased, however, the wall friction forces will be reduced, and the stagnation pressure ratio as well as the performance coefficient will be increased with initial mach number. The maximum values will probably then be obtained when gas-saturation limitations are met.

5. Comparison of Measured Performance Coefficient with Results of High-Velocity Discontinuity Analysis.

The high-velocity discontinuity analysis of Appendix B permits the theoretical computation of the aerothermopressor performance coefficient subject to the assumptions stated in Appendix B. Gavril (2) has carried out such computation in which the stagnation pressure corresponding to that entering the diffuser section p_{02} replaces the measured stagnation pressure p_{03} in the definition of the performance coefficient. The stagnation pressure p_{02} is defined arbitrarily as

$$\frac{p_{02}}{p_2} \equiv \left[1 + \frac{k_2}{K_{202}} \frac{K_{202}-1}{2} M_2^2\right]^{\frac{K_{202}}{K_{202}-1}}$$

The results of these calculations therefore do not account for the influence of liquid in the actual diffusion process or the inefficiencies in the actual diffuser process.

Two points taken from these calculations have been spotted on the measured performance curves of Figure 22. The points correspond to the following assumed conditions:

initial mach number M_1	0.50	0.75
initial stagnation temperature T_{01}, °R	1500	1500
initial injection rate ω_0, lb water/lb air	0.25	0.25
friction factor, f	.0037	.0037
wall friction term based upon distance to section 2, $f \frac{L}{D}$	.127	.127
fraction evaporated, $\frac{\omega_2}{\omega_0}$	0.80*	0.90*

As would be expected, the computed points lie considerably above the corresponding experimental results. The principle reasons for the discrepancy are the following:

a) The actual diffuser efficiency was undoubtedly considerably lower

---

* Extrapolated values based upon the data of Section III D.

than the assumed 100% value of the calculations.

b) There were errors in the assumed values of the fraction evaporated and the wall friction term.

c) The actual flow was not one-dimensional as assumed in the theoretical analysis.

D. Measurements of Rates of Evaporation

1. Corrections for Initial Water Vapor Content

In section II C, it is shown that humidity probe I (Figure 8) was generally more satisfactory in operation than probe II (Figure 9). Consequently, for all humidity measurements at high temperatures only probe I was used. Furthermore, since the inaccuracies caused by liquid water intake in the sampling hole of probe I under very severe conditions were found to be small, the measured values of the specific humidity taken with this probe under high temperature conditions were assumed to be correct to within the accuracy of other measurements.

The measured water vapor content of the sample stream was composed of water vapor from the evaporation of the injected liquid plus the water vapor present in the stream entering the aerothermopressor from the surrounding atmosphere and from the combustion in the gas furnace. To obtain the so-called "corrected" specific humidity--the water vapor content caused by evaporation alone--it was therefore necessary to subtract the specific humidity of the stream entering the aerothermopressor from the measured value of the specific humidity.

The gas used in the gas burner was composed largely of methane, CH_4, which upon complete combustion yields 2.25 pound of water vapor for every pound of fuel burned. For 100% efficient combustion to raise the air temperature from atmospheric to 1500°R, the water vapor formed in combustion would thus amount to about .0257 lb water per lb air. On an operating day when the outside atmospheric dew point was 40°F (specific humidity = 0.0052 lb water per lb air), the specific humidity of the 1500°R stagnation temperature stream running with no water injection was actually measured at 0.031 lb water per lb air, which corresponds to the sum 0.0257 + 0.0052 = 0.0309 lb water per lb air.

Therefore, during all tests, in which humidities were measured the sum of the specific humidity corresponding to the outside dew point of the outside atmosphere and the value of 0.0257 lb water per lb of air for combustion was subtracted from the measured values. Most humidity tests were run on warm rainy days when the outside dew point was about 60F (specific humdity =0.011 lb water per lb air); the value 0.037 lb water per lb air was therefore subtracted from the measured values to obtain the corrected values of specific humidity resulting from the evaporation of the injected water.

2. Humidity Variation Along Evaporation Section

a. Evaporation Rates Measured with Sampling Probe

To investigate experimentally the rate of evaporation of the injected water, humidity measurements were taken along the evaporation section for two different initial injection rates, $\omega_0 = 0.15$, and 0.25 lb water per lb air, using nozzle no. 3 (Table 1)-for constant values of the initial parameters: stagnation temperature $T_{01} = 1500$ R, stagnation pressure $p_{01} = 14.6$ psia and Mach number $M_1 = 0.50$. Measurements were taken at seven positions across the diameter of each cross-section corresponding to access ports which were located respectively 4.5 in, 13.5 in, 40.5 in, and 67.5 in, from the plane of injection.

The results of these traverse tests are shown in Figures 24 and 25 as the profiles of the fraction of liquid evaporated $\frac{\omega}{\omega_0}$ (corrected specific humidity divided by the initial injection rate) at each cross-section. The measurements at ports located 13.5, 40.5, and 67.5 inches from the plane of injection were easily repeated, but the measured dew points at the port located 4.5 in. from the plane of injection fluctuated markedly. This fluctuation was undoubtedly caused by excess water impingement on the probe. At this distance from the injection nozzle much of the water was probably still in the form of long unsteady ligaments rather than small drops (7). The values reported for this access port are those corresponding to the lowest dew point temperatures measured and may be in considerable error.

The lack of symmetry of the profiles at the cross-sections nearest the nozzle may be explained by the fact that, with nozzle no. 3, water was injected at seven discrete points of the cross-section, and complete mixing of the stream had not yet occurred at these cross-sections. The rise of the profile near the tube walls at downstream cross-sections was probably caused by evaporation from the wetted walls of the tube. The shapes of the profiles near the walls were extrapolated from the measured data, and for the cross-section nearest the injection plane are probably subject to great error.

The average fraction evaporated at each cross-section was computed by graphical integration of the profiles of Figures 24 and 25, assuming that these profiles were typical of the distribution across each diameter ± 90° from that corresponding to the measurements and that the velocity across each cross-section was constant. The average fraction evaporated was thus defined as:

$$\left(\frac{\omega}{\omega_0}\right)_{AVG} = \frac{4}{D^2}\int_{-\frac{D}{2}}^{+\frac{D}{2}}\left(\frac{\omega}{\omega_0}\right) r\,dr .$$

It is evident that errors in extrapolation of the profiles in Figure 24 and 25 and in the assumptions of the integration have an appreciable effect on the value of the average fraction evaporated which is computed.

The average fractions evaporated computed by this technique are plotted as a function of the distance from the plane of injection in Figure 26. The rate of evaporation indicated by these measurements is extremely high during the first portion of the evaporation, the "turbulent" regime, and quite low during the remaining portion of the evaporation, the "molecular or laminar" regime.

The turbulent regime is characterized by large differences of velocity between the gas and liquid drops; these velocity differences give rise to large values of the heat transfer coefficients. This fact, together with the large differences in temperature between the gas and liquid drops, accounts for a high time rate of evaporation of the liquid. Since the velocities of the drops are low, the stay times of the drops are high, which, in combination with high time rates of heat transfer, makes for large gradients of the fraction evaporated with distance from the plane of injection.

In the laminar regime, the effects are quite the opposite. The liquid drops travel at velocities almost equal to the gas velocities, and the heat transfer coefficients are correspondingly low. Since the temperature of the gas has also been reduced, the resulting time rates of heat transfer and evaporation are low. In addition, the high drop velocities make the stay time of the drops low. As a result the gradients of the fraction evaporated with distance are low in the laminar regime.

The curves of Figure 26 also show that for a given distance from the plane of injection, the fraction evaporated is smaller for the larger initial injection rate, although the actual specific humidity is larger. This behavior may be explained qualitatively by noting that the rate of evaporation is approximately proportional to the number of droplets formed per unit time and to the temperature difference between the gas and liquid,

$$\frac{d\omega}{dt} \sim N(T - T_q),$$

where N is the number of drops per unit mass rate of flow of air. The rate of change of the fraction evaporated may also be approximated by

$$\frac{d\left(\frac{\omega}{\omega_0}\right)}{dt} \sim \frac{N}{\omega_0}(T - T_q).$$

Since the size of the droplets may be assumed practically independent of the injection rate, the value of N is larger for the higher injection rate, and, although the temperature of the gas will fall more rapidly in this case, the rate of evaporation is controlled by N. Consequently the specific humidity at any distance from the injection point is higher for the larger injection rate.

On the other hand, the rate of change of the fraction evaporated is proportional to the temperature difference since the term $\frac{N}{\omega_0}$ is practically independent of injection rate. Since the rate of evaporation and, consequently, the gas temperature decrease, ~~is~~ are higher for the larger injection rate, the rate of change of the fraction evaporated is smaller. Thus, at any particular cross-section, the fraction evaporated is smaller for the larger initial injection rate.

The foregoing approximate analysis is, of course, not valid when the gas stream approaches a saturated condition.

b. Evaporation Rates Inferred from Static Pressure Data

As explained in Section III E, it is possible to infer the fraction evaporated at any particular cross-section from the static pressure measured at that cross-section providing the following assumptions are made:

i) The wall friction term $f \frac{L}{D}$ is evaluated from an assumed value of the friction factor f.

ii) The velocity of the liquid is assumed equal to the velocity of the gas.

iii) The flow is one-dimensional.

With these assumptions the results of calculations based on the high-velocity discontinuity analysis (Appendix B) may then be used to predict the fraction evaporated.

An effective friction factor f = 0.0040 (based upon the interpretation of wall friction data of Section III E) was assumed to predict the fraction evaporated from the static pressure data (Figure 31) corresponding to those runs in which the vapor sampling probe was used (Figure 26). These static pressure data in combination with the results of the computations based upon the discontinuity analysis (Figure 32) permitted the prediction of the fraction evaporated.

For comparison, the rate of evaporation predicted in this way from the static pressure data ~~and~~ are plotted on Figure 26 together with those rates measured by direct sampling of the stream. The discrepancies between the results of the two methods are large for that portion of the process which occurs in the first three or four feet of the evaporation section and quite small for the remainder of the process. This behavior is to be expected for the following reasons:

i) The liquid was not uniformly distributed in the stream near the plane of injection, and also some liquid may have been taken in the sampling hole.

ii) Errors in the extrapolations of the measured humidity data in Figures 24 and 25 may have resulted in appreciable errors in the prediction of the average values ~~were~~ over the cross-section from these data.

iii) The assumptions in the analysis that the liquid velocity was equal to the gas velocity and that the flow was one-dimensional were most in error during the initial portions of the evaporation processes.

iv) The assumed value of the effective wall friction factor was probably in some error, and the method of averaging the wall friction forces in the analysis (assumption 6 of Appendix B) may also have introduced errors.

c. Results of Theoretical Analysis

Also plotted on Figure 26 is a curve resulting from a stepwise numerical integration of the equations developed in the theoretical analysis of droplet evaporation presented in Appendix D. The integration was carried out for the following parameters:

initial stagnation temperature, $T_{01} = 1500$ R

initial stagnation pressure, $p_{01} = 14.7$ psia

initial mach number, $M_1 = 0.50$

initial injection rate, $\omega_0 = 0.20$ lb water/lb air

Fanning friction factor, $f = 0.005$

diameter of evaporation section, $D = 2.125$ in.

The point where the Reynolds number based upon the relative velocity, $Re_F = \frac{\rho (V - V_f)\, d}{\mu_F}$, reaches unity is indicated on the theoretically determined curve.

At first sight, discrepancies between the computed curve and the experimentally-determined curves appear quite large. Actually, in view of the assumptions made in the theoretical analysis and the sources of empirical data utilized in the computation, the agreement is indeed encouraging. Of the assumptions discussed in Appendix D, those which probably contribute most to the observed discrepancies are as follows:

i) The assumption that upon injection of the water into the gas stream, a homogeneous distribution of the drops is formed instantaneously is far from actual fact. Plender (7) has observed that ligaments of water are formed as the water issues from the nozzles; these ligaments are in turn broken up into small drops. A reasonably homogeneous distribution of the droplets is not formed until the water has progressed a distance of the order of five or more inches from the injection point. The surface-volume mean droplet diameters which are predicted by the Nukiyama and Tanasawa (8) and Plender (7) are not achieved until the water has traversed this distance.

Since in the experiments under discussion, water was injected at seven discrete points of the entrance cross-section, it is not surprising to find that the experimental data indicate much larger effective drop sizes during the turbulent portion of the evaporation.

ii) The assumption that heat and mass transfer coefficients can be evaluated by extrapolating data taken from experiments in which the relative velocities and temperature differences were of a smaller order of magnitude may also account in part for the observed discrepancies. The same statement may be made regarding the drag.

iii) The assumptions that all drops once formed, are of the same size at any particular cross-section, and that no liquid impinges and evaporates from the walls also contribute to the error.

3. Variation in Evaporation Rate with Initial Mach Number and Initial Injection Rate

The fraction evaporated profiles of Figures 24 and 25 indicate that the values measured at the center of the cross-section at the port located 67 1/2" from point of injection are very nearly equal the average fraction evaporated taken over the entire cross-section. To facilitate the experimental study of the effects of changes in evaporation rates caused by changes in initial mach number and injection rate, measurements were taken only at the center of the cross-section at this access port location.

For these experiments, the initial stagnation temperature T_{01} and pressure p_{01} were held constant at 1500 R and 14.5 psia respectively. The initial injection rate ω_0 was varied from 0.10 to about 0.35 lb water per lb air for constant values of the initial mach number $M_1 = 0.50$ and 0.60. The results of these experiments are plotted in Figure 27.

For constant values of initial mach number, the quantities of the injected water which is evaporated increases, but the fraction of the injected water which is evaporated decreases as the initial injection rate is increased. This behavior is explained in the preceding section.

At a given injection rate, the amount evaporated is seen to increase with increasing initial mach number. Since the distance traveled by each droplet during the turbulent regime is comparatively small compared to the total distance traveled for complete evaporation, this total distance may be approximated by

$$L = Vt$$

where t is the time necessary for complete evaporation. From Appendix D, the heat transfer equation for the laminar regime, equation D11, indicates that

$$t \sim d^2 .$$

Also from Appendix D, equation D16, it is seen that the diameter of the drop is inversely proportional to the gas velocity,

$$d \sim \frac{1}{V} .$$

Combining these equations we have

$$L \sim \frac{1}{V} ,$$

which indicates that the length of evaporation section for complete evaporation is inversely proportional to the initial velocity.

Therefore, for a given position in the test section and for a fixed initial injection rate, a higher fraction was measured for the larger initial velocity or mach number.

E. Experimental Evaluation of the Effective Wall Friction Factor

1. General Procedure

In order to interpret the experimental data obtained in these small-scale experiments and in order to predict the performance of large-scale aerothermopressors on the basis of these data, it was necessary to evaluate the effective wall friction factor f. The presence in the stream of liquid water which may impinge upon the walls, run along the walls, and be torn from the walls by the gas stream, makes the application of ordinary dry-wall friction data somewhat questionable. Since the analysis of these effects separately is complex, an "effective" friction factor which really lumps together all momentum effects at the walls has been used in the interpretation of the experimental data.

The effective friction factor was evaluated from the results of three sets of experiments:

i) Experiments with no liquid injection run at low and high temperatures and at initial mach numbers corresponding to choked conditions at the exit of the constant-area evaporation section.

ii) Experiments with liquid injection run at low temperatures with initial mach numbers corresponding to choked conditions at the exit of the constant-area evaporation section.

iii) Experiments with liquid injection and evaporation run at high temperatures and with simultaneous measurements of pressure variation and humidity variation along the length of the evaporation section.

The effective wall friction factor was then predicted by comparing the results of these experiments with computations made on the basis of the high-velocity discontinuity analysis (Appendix B) and, for the runs with no liquid injection, with the properties of the Fanno line (9).

2. Hot Dry Runs

In Figure 28, the variation of the initial mach number at choked flow M_{1c} with the wall friction term $f \frac{L}{D}$ for no liquid injection and for an initial stagnation temperature $T_{01} = 1500°R$ is plotted. The values corresponding to the Fanno line do not agree exactly with the values predicted by the high-velocity discontinuity analysis because, in the former, the variation of the wall friction along the constant-area section is computed by exact methods, while in the latter, this variation is averaged along the length of the test section. (See assumption 6 of Appendix B.) The value of the initial mach number observed experimentally in tests corresponding to these conditions is shown ($M_{1c} = 0.598$). This same value, within ± 0.3% was observed for tests at inlet stagnation pressure of 10.9 and 14.8 psia.

3. Cold Dry and Wet Runs

In Figures 29 and 30 are plotted the results of tests at the low initial stagnation temperature T_{01} of 520 R with and without liquid injection. In Figure 29, the initial mach number corresponding to choked flow M_{1c} as measured in tests and as predicted by the high-velocity discontinuity analysis is plotted as a function of the initial injection rate ω_0. The experimental results of Figure 29 indicate that the value of the wall friction term $f \frac{L}{D}$ corresponding to the test with no liquid injection is about 0.11, while that corresponding to tests with liquid injection is about 0.12, based upon discontinuity analysis.

In Figure 30 the ratio of the measured static pressure at the choked point to the initial stagnation pressure $\frac{p_{2c}}{p_{01}}$ is plotted as a function of the initial injection rate ω_0. Since no pressure tap existed at the end of the constant-area section, the static pressure at the choked section was actually obtained by extrapolating the measured pressures along the length of the section. The mach number data of Figure 29 are therefore probably somewhat more reliable than the pressure data of Figure 30, although there is good agreement between the two.

4. Hot Wet Runs

As discussed in Section III D, the curves of Figure 26 show the variations in the measured rate of evaporation with length which were obtained with the vapor sampling probe I (Figure 8) and the humidity measuring apparatus (Figure 10). In Figure 31 are plotted the static pressure variations with distance from the plane of injection which were measured for the same initial conditions as those corresponding to the curves of Figure 26.

The equations resulting from the high-velocity discontinuity analysis of Appendix B permit the prediction of the effective wall friction factor from these measured pressure and humidity data. Gavril (2) has computed the variation in the ratio of static pressure to initial stagnation pressure $\frac{p}{p_{01}}$ as a function of the fraction of water evaporated $\frac{\omega}{\omega_0}$ for various values of the wall friction term $f\,\frac{L}{D}$. A portion of these computed results which apply to the values of the initial parameters used in the tests represented by the curves of Figures 26 and 31 are plotted in Figure 32.

By entering the charts of Figure 32 with values of the measured static pressure from Figure 31 and the corresponding fraction evaporated from Figure 26, it is possible to estimate the effective wall friction term $f\,\frac{L}{D}$ and consequently the effective friction factor f. The values of the friction factor f computed in this way are very high if the measured data are taken at distances quite close to the plane of injection. The predicted values are smaller for the data taken at larger distances from the plane of injection. This discrepancy is expected for two reasons--i) the humidity measurements are probably more reliable at the greater distances, and ii) in the high-velocity discontinuity analysis, the velocity of the liquid is assumed to be equal to the velocity of the gas and the flow is assumed to be one-dimensional.

5. Tabulation of Friction data

A tabulation of the pertinent friction data obtained by the methods described in the preceding sections follows:

Analysis of Experimental Wall Friction Data

(Diameter of evaporation section D = 2 1/8 inches)

Initial Stagnation Temperature, T_{01}, ^{o}R	1500	1500	520	520	1500	1500
Initial stagnation pressure, p_{01}, psia	14.8	10.9	14.7	14.7	14.6	14.6
Initial injection rate, ω_0, lb water/lb air	0	0	0	.30	.15	.25
Initial mach number, M_1	.597	.597	.595	0.45 to 0.53	.50	.50
Distance from plane of injection, L, inches	$73 \frac{1}{4}$	$73 \frac{1}{4}$	$73 \frac{1}{4}$	$73 \frac{1}{4}$	65	65
Observed wall friction term for discontinuity analysis, $f \frac{L}{D}$	.116	.116	.110	.120	.122	.140
Observed wall friction term for Fanno line, $f \frac{L}{D}$	.131	.131	.128	----	----	----
Effective wall friction factor from discontinuity analysis, f	.00337	.00337	.00319	.00348	.00398	.00457
Effective wall friction factor from Fanno line, f	.00381	.00381	.00371	----	----	----
Initial Reynolds number of gas flow, Re_1	174,500	128,300	605,000	502,000	154,000	154,000
Predicted friction factor from $f = 0.046 (Re_1)^{-0.2}$	.00410	.00438	.00320	.00332	.00425	.00425

The effective friction factor predicted by the discontinuity analysis is seen to differ from that predicted by the Fanno line data by as much as 20% for the runs without liquid injection. A similar error might be expected in the prediction of the friction factor for the runs with liquid injection when the discontinuity analysis is used.

On the basis of the dry run data, the effective friction factor is seen to be somewhat less dependent upon the Reynolds number than the usual experimental correlations indicate ($f = 0.046\ Re_1^{-0.2}$, for example). The injection of liquid on the other hand, has an appreciable effect. For the cold runs, the injection of liquid increased the friction factor by about 10%. For the hot runs, this effect was apparently somewhat stronger although the interpretation of the data taken from hot runs with evaporation introduces some errors. In particular, the value of $f = 0.00457$ predicted for one of the hot runs is somewhat high compared to the other data.

For the purposes of the extrapolation of the small-scale performance data to larger-scale aerothermopressors, an effective friction factor $f = 0.0040$ will be used. This value appears to be a conservative estimate and reasonably well-applicable to the range of hot runs with evaporation which were made.

IV Summary of Results and Conclusions

A. Summary of Results of Tests of the Small Scale Aerothermopressor

1. General Effects of Liquid Injection into a Gas Stream

The theoretical analysis of the aerothermopressor process presented in Appendix A permits a qualitative interpretation of the effects of liquid drag, liquid evaporation, and wall friction from the measured static pressure distribution along the constant-area evaporation section.

For tests at low initial stagnation temperatures, in which little or no liquid was evaporated, the drag due to liquid acceleration and wall friction caused large decreases in static pressure and correspondingly large increases in mach number along the test section (Figure 17). These effects increased with increased liquid injection rates.

For tests at high initial stagnation temperatures, in which appreciable quantities of liquid were evaporated, the overall aerothermopressor process at subsonic mach numbers could be separated qualitatively into three sub-processes: (i) just after injection of liquid, the liquid drag and wall friction effects were predominate over the evaporation effects and consequently there were large decreases in pressure and large increases in mach number; (ii) at a certain point in the process the evaporation effects became predominate and there were corresponding increases in static pressure and decreases in mach number; and (iii) after the liquid had been accelerated to velocities approximately equal to the gas velocities and the gas temperature had decreased, the wall friction effects became predominate over the evaporation effects and there again occurred decreases in pressure and increases in mach number (Figures 17, 18 and 19).

For high values of the initial mach number, a mach number of unity was reached at a point in the evaporation section where the evaporation effects became predominate over liquid drag and wall friction effects. The flow was choked at this condition and no further increases in initial mach number could be achieved. The flow downstream of this critical point ~~remained either subsonic or~~ became supersonic with shock to subsonic flow at a position depending upon the back pressure at the exit of diffuser (Figure 19). In the supersonic portion of the flow, the individual effects of liquid drag, liquid evaporation, and wall friction on the static pressure and mach number were exactly opposite to the corresponding effects in subsonic flow.

2. Effects of Design of Water Injection Nozzles on Performance

The overall performance of the aerothermopressor was measured by the value of the normalized overall rise in the stagnation pressure $(\frac{p_{03} - p_{01}}{p_{01} M_1^2})$. It was found that the performance at any given set of values of the initial parameters was very much dependent upon the injection nozzle design. Nozzles which gave good distribution of liquid in the gas stream over a wide range of liquid injection rates were found to be the most effective (Figure 21 and Table 1).

Nozzle No. 3 (Table 1) which consisted of a seven axial injection tubes, one in the center and six symmetrically disposed in a circle of 5/8 inch radius, gave the most satisfactory overall performance.

3. Effects of Variation in Initial Parameters on Overall Performance at High Initial Stagnation Temperatures

a) Initial Injection Rate

At any given set of initial conditions, the overall performance was first increased as water was injected, reached a maximum and then decreased as the water injection rate was increased above the optimum value (Figure 20).

The decrease in performance at higher injection rates occurred because the added drag losses due to water injection were not compensated for by added evaporation gains, since the gas approached saturation temperature conditions.

b) Initial Stagnation Temperature

The optimum performance of the aerothermopressor was improved as the initial stagnation temperature was increased (Figure 22). This effect was caused by the larger rates of evaporation at the higher temperatures.

c) Initial Stagnation Pressure

In the small-scale apparatus under test, the overall performance was reduced as the pressure level was decreased (Figure 22). Although the detrimental wall friction effects were low at lower pressure levels due to the lower density level, the decreased rate of evaporation due to the lower values of Reynolds number during the turbulent evaporation period apparently was controlling. The reverse effect with change in pressure level may occur in large scale aerothermopressors. In the large scale devices where wall friction effects are unimportant, longer evaporation sections which take advantage of the evaporation during the laminar period of evaporation may be possible. Since, as the pressure level is reduced, the water content of the gas stream corresponding to saturation at any given temperature is increased, the performance of large-scale aerothermopressors may improve if the pressure level is lowered.

d) Initial Mach Number

The overall performance of the aerothermopressor increased as the initial mach number was increased and reached a maximum at choked flow conditions (Figure 22). Since large-scale aerothermopressors will be high-velocity devices, this trend is encouraging.

The best values of the overall performance achieved at an initial stagnation pressure of about one atmosphere were as follows:

initial stagnation temperature T_{01}, °R	initial mach number M_1	optimum performance $\left(\frac{p_{03} - p_{01}}{p_{01} M_1^2}\right)_{opt}$
1200	0.777	-0.228
1500	0.780	-0.158
1800	0.785	-0.126

The values of the performance coefficients predicted by the high-velocity discontinuity analysis of Appendix B for a perfect diffuser are shown on Figure 22. The discrepancy between the computed and measured values indicates, that the diffuser was quite inefficient.

4. <u>Measurements of the Effective Wall Friction Forces</u>

The effective wall friction forces were measured for choked flow runs with no water injection at low and high temperature levels by comparison of the measured mach number and pressure ratios with Fanno curve data and the results of the high-velocity discontinuity analysis of Appendix B, (Figures 28, 29 and 30). The values of the Fanning friction factors obtained were in reasonable agreement with those predicted on the basis of usual prediction equation although the dependence upon Reynolds number appeared to be somewhat lower than would usually be predicted.

For tests with liquid injection at both low and high temperatures, the effective friction factor was found to be greater than that for the equivalent dry runs by about 10%. On this basis the Fanning friction factor value corresponding to most of the high temperature tests with liquid injection was taken to be $f = 0.0040$ for the purposes of extrapolation of small-scale test results to large scale aerothermopressors.

5. Measurement of Evaporation Rate

The vapor sampling probe no. 1 (Figure 8) was effective in removing samples of the vapor from the liquid-vapor stream in the aerothermopressor. With this probe, traverses of the stream at various cross-sections were made (Figures 24 and 25). These traverses indicated that good mixing of the liquid vapor mixture was probably not achieved until a distance of about thirty inches from the point of injection.

The variation of fraction of liquid evaporated along the test section was measured and compared with the results of a numerical integration of the controlling equations of the drop evaporation analysis of Appendix D (Figure 26). In view of the many assumptions made in the theoretical analysis, the agreement between theory and experiment appears quite good. Comparison of the measured and theoretical results indicates that the liquid droplets were formed by successive break-up with smaller and smaller particles as they progressed down the evaporation section. The effective drop size in the overall process was apparently smaller than that predicted by the usual equation of Nukiyama and Tanasawa (8).

The measured rate of evaporation also indicated that very little evaporation occurred in the last three feet of evaporation section. For this small scale aerothermopressor, the performance would probably, therefore, be improved if the length of the constant-area section were reduced. In larger scale apparatus this would not be the case since the wall friction effects would be very small, and the low evaporation rates during the laminar portion of the evaporation regime might therefore produce appreciable increases in stagnation pressure. The fraction of the initial injection rate which was evaporated decreased with increasing injection rate, but the total amount of water evaporated increased with initial injection rate over the range tested (Figures 26 and 27).

B. Extrapolation of Small Scale Test Results to Large Scale Aerothermopressor Processes

The direct mathematical integration of the controlling differential equations for the aerothermopressor process is impossible since the equations are so complex. It is possible to extrapolate the performance measured for the small-scale aerothermopressor in an approximate manner by making use of the differential equation for the rise in the stagnation pressure developed in Appendix A-which may be written in the form

$$\frac{dp_0}{p_0 M^2} = dY - 2\,f\,k\,\frac{dL}{D} \quad ,$$

when the single term dY represents the total effect of all the terms which account for the liquid injection, acceleration, and evaporation. Since neither the stagnation pressure p_0 nor the mach number M changes greatly in the course of the evaporation process at subsonic speeds, this equation may be integrated to the approximate form

$$\frac{p_{03} - p_{01}}{p_{01}\,M_1^{\,2}} = Y - 2f\,k\,\frac{L}{D}$$

Making use of the approximate integrated equation, the results obtained by experiment on the small-scale aerothermopressor may be extrapolated to predict the performance of larger-scale subsonic aerothermopressors. The experimental values for the performance coefficient $\frac{p_{03} - p_{01}}{p_{01}\,M_1^{\,2}}$, the friction factor f, and the length-diameter ratio $\frac{L}{D}$ may be used to compute the value Y. With this value of Y, values of performance coefficient corresponding to larger scale aerothermopressors (smaller values of $\frac{L}{D}$) may be estimated for fixed values of the initial parameters corresponding to the small scale tests. For the best experimental results corresponding to Figure 22, the following parameters apply:

initial stagnation temperature T_{01} °R	1200	1500	1800
initial mach number M_1	0.777	0.780	0.783
initial stagnation pressure p_{01} atm	1.0	1.0	1.0
mass rate of flow of air w_a lb/sec	0.755	0.677	0.612
estimated friction factor f	0.0040	0.0040	0.0040
specific heat ratio k	1.35	1.35	1.35
length to diameter ratio $\frac{L}{D}$	34.5	34.5	34.5
optimum injection rate ω_0 lb water/lb air	0.17	0.24	0.31
optimum performance $\left(\frac{p_{03} - p_{01}}{p_{01} M_1^2}\right)_{opt}$	-0.229	-0.159	-0.127
Y (computed)	0.145	0.215	0.247

Making use of the computed values of the parameter Y, the stagnation pressure ratio $\frac{p_{03}}{p_{01}}$ corresponding to smaller values of the length-diameter ratio may be predicted for the same values of the initial parameters used in the test work. The results of such computations are shown in Figure 33 for assumed values of $k = 1.35$ and $f = 0.0040$. These results show that appreciable stagnation pressure ratios may be achieved in large-scale aerothermopressors.

The extrapolation is conservative since the following improvements in large scale devices over and above the reduction in the length-diameter ratio should be achieved:

a) The friction factor f should be lower since the Reynolds number will be higher and there will be less impingement of water on the walls.

b) The diffuser efficiency will probably be improved. Studies are now under way to determine the optimum design parameters of a diffuser which takes advantage of the momentum effects of any liquid water which enters.

c) The determination of optimum evaporation section length and the variation of cross-sectional area with length of this section (see Section IV C) will provide improvements in performance.

d) The optimum values of the injection rate should be higher in the large-scale aerothermopressors which should result in higher values of the parameter Y.

Considerable improvements in the performance of a simple gas turbine through the use of an aerothermopressor may be predicted even on the basis of the conservative extrapolation to larger scale shown in Figure 33. Consider a simple air-standard cycle gas turbine plant with the following characteristics:

temperature of air entering compressor = 70F
temperature of gas entering turbine = 1500F
pressure ratio across compressor = 4.0
efficiency of compressor = 85%
efficiency of turbine = 85%
mass rate of flow of air = 23.1 lb/sec

The net power output of this plant without an aerothermopressor would be 2000 hp with a thermal efficiency 20.75%.

If an aerothermopressor of about the same length as the small-scale experimental device were applied to this plant, the corresponding operating point may be found by trial and error on Figure 33. The aerothermopressor would operate with an inlet stagnation temperature of 1440 R and an inlet mach number of about 0.78. It would have a diameter of 12.6 inches, and it would produce a stagnation pressure ratio of 1.085. The water flow required for this application would be about 1.1 gallons per minute. If the expansion turbine were modified to expand to the corresponding lower exhaust pressure with no change in expansion efficiency, the net power output and the thermal efficiency of the plant would be increased by 10.47% above the values for the plant without the aerothermopressor.

This percentage improvement would increase with the size of the plant because the scale of the aerothermopressor would increase. Since the extrapolation above is quite conservative, it may be assumed that with suitable development of large scale aerothermopressors, far greater improvements in performance of gas turbine plants may be achieved.

C. Some Comments on the Design of a Large-Scale Aerothermopressor

From the results of the experimental work on the small-scale, constant-area aerothermopressor, it appears advisable to construct and test a large-scale apparatus. At the present time, plans are being made to construct such a large scale unit at the Gas Turbine Laboratory of M.I.T., utilizing air from the large compressor now under construction for the new Ram Jet Test Facility of the Chemical Engineering Department. This compressor will be capable of delivering a mass flow rate of air of 45 pounds per second, which corresponds to a subsonic aerothermopressor of about twelve or thirteen inches in diameter.

It is apparent from the small-scale experimental work that the best design of water injection nozzles for the large-scale rig will probably be of the multi-axial injection type arranged in some form of grid at the entrance of the evaporation section of the aerothermopressor.

It is also apparent from the experimental work that the optimum length of the evaporation section of the large-scale device will probably be larger than the small-scale evaporation section since smaller wall friction effects will permit better utilization of the beneficial evaporation effects in the laminar evaporation regime. The calculation based upon a drop history analysis, similar to that of Appendix D now being processed by Gavril (2) will be valuable in the prediction of the optimum length of evaporation section of the large-scale apparatus.

In addition, the results of these calculations will be helpful in the prediction of the manner in which the cross-sectional area of the evaporation section should be varied with length. For simplicity of manufacture, experiment, and theoretical interpretation of the experimental data, the small-scale aerothermopressor was constructed with a constant area section, but theoretical considerations suggest that better performance will probably result from evaporation in a section whose cross-sectional area varies with length.

An approximate analysis has been developed which suggests that the optimum performance of the aerothermopressor may be achieved when the cross-sectional area of the evaporation section is varied in such a manner as to achieve a constant value of mach number for the flow. This prediction is to be expected since the influence coefficients developed in Appendix A for the change in stagnation pressure $\frac{dp_0}{p_0}$ show that $\frac{dp_0}{p_0}$ increases with the square of the local mach number M^2. If the mach number is maintained at a uniformly high value, the rise in stagnation pressure should thus be an optimum for that mach number level.

The approximate analysis is a discontinuity analysis exact only for very low velocities; it is presented in Appendix D. To predict the optimum design conditions from the analysis, the assumption is made that the cross-sectional area variation with length is such that the pressure-area variation is given by the relation

$$\frac{dp}{dA} = CA^m ,$$

where

$$C = (m+1)\frac{p_1}{A_1^{m+1}} \frac{\left[\frac{p_2}{p_1} - 1\right]}{\left[\left(\frac{A_2}{A_1}\right)^{m+1} - 1\right]} ,$$

and m is constant for any process under consideration. Approximate expressions for the normalized rise in stagnation pressure $\frac{p_{02} - p_{01}}{p_1 k_1 M_M^2}$ are developed where the mach number M_M is made equal to the larger of either the initial mach number M_1 or the final mach number M_2, depending upon the value of ratio of the initial area to the final area of the evaporation section $\frac{A_1}{A_2}$. Since the successful design of various components of the aerothermopressor, such as the diffuser, becomes more difficult at high values of mach number, the use of the maximum mach number M_M as defined above provides a better basis for comparison of performance than the use of either M_1 or M_2 individually.

Computations of the performance predicted on the basis of this analysis have been carried out over a wide range of values of the area ratio $\frac{A_1}{A_2}$ and the constant m for a fixed initial state corresponding to an initial stagnation temperature $T_{01} = 1500$ R, initial mach number $M_1 = 0.50$, and an initial injection rate $\omega_0 = 0.175$ lb water per lb air. The results of these computations are plotted in Figure 34.

The optimum performance occurs at an area ratio corresponding to a mach number ratio $\frac{M_1}{M_2} = 1.0$, for any particular value of the constant m. In the range of area ratios most likely of interest in aerothermopressor design, say from $\frac{A_1}{A_2} = 1.0$ to 1.5, the influence of differences in the value of m is small. It may, therefore, be concluded on the basis of this approximate analysis that the optimum design of an aerothermopressor evaporation section will be one in which the mach number is maintained at a reasonably high constant value.

D. Additional Remarks on a Future Program

The results of the small-scale experimental work have been sufficiently encouraging to warrant the construction of a large-scale aerothermopressor as noted in Section IV C. The experimental work has also made obvious the need for the following additional investigations:

1. The possibilities of the small-scale aerothermopressor test rig have by no means been exhausted by this work. Experiments with this device will be continued in which the constant area evaporation section is shortened and in which diffusers of varying geometry are tested.

In particular, further study of the phenomena associated with transition from subsonic to supersonic flow in a constant-area evaporation section will be made. Since the performance of the aerothermopressor is inherently superior at high velocities, this hitherto unobserved transition may be the key to successful design of large-scale aerothermopressors which operate in both the subsonic and supersonic regimes.

2. The overall performance of the aerothermopressor depends to a large extent upon the efficiency of the diffuser at the end of the evaporation section. The presence of liquid water droplets in the gas stream and the presence of liquid on the diffuser walls both suggest that normal empirical methods of diffuser design may necessarily require modification for this application. A theoretical and experimental program to study these effects is now under way under the overall aerothermopressor project.

3. The apparent success of the vapor sampling probes used in the small scale experimental work justifies continuation of the development of these probes. Time limitations prevented a complete exploitation of the possibilities of these probes for the study of the evaporation rates and for the possible

study of stagnation temperature distribution in the aerothermopressor. In particular, vapor-sampling probes of smaller size which are capable of removing samples nearer the tube walls and which produce smaller disturbances in the flow would be desirable. More complete surveys over the cross-sections near the plane of injection would be desirable.

The development of probes which satisfactorily measure the distribution of the liquid droplets in the gas stream and the development of total pressure probes for use with liquid-vapor mixtures are now under way. These three types of instrumentation when perfected will be invaluable in studying the details of the complex aerothermopressor process.

4. Theoretical studies will be continued to provide better means for interpreting experimental data and for extrapolation of these data to optimum designs of large scale aerothermopressors. With the experimental data from this work and with the results of the computations now being carried out by Gavril (2) in hand, it may be possible to develop a simplified approximate analysis of the aerothermopressor process which will adequately predict changes in performance which may be expected with changes in initial parameters, evaporation-section ~~and~~ area variation, etc.

Appendix A

Derivation of Influence Coefficients for Adiabatic, Constant-Area Liquid-Evaporation Processes

An analysis of the flow of a compressible fluid into which liquid is evaporating in the presence of wall friction effects has been made by Shapiro and Hawthorne (1). The resulting equations for the flow are presented in the form of influence coefficient tables--the influence coefficient corresponding to any one dependent and one independent variable being defined as the value of the partial derivative of the dependent variable with respect to the independent variable.

In the work of Reference 1, the assumptions are made that the liquid is injected continuously along the length of the evaporation section and that this liquid is accelerated to the gas velocity and evaporated immediately upon injection. In the aerothermopressor, however, liquid is injected at only a few discrete cross-sections of the evaporation section, and evaporation occurs while the liquid is entrained in the gas stream. The purpose of this section is to determine the influence coefficients for a flow in which all liquid is injected at one cross-section and in which evaporation takes place from the liquid drops entrained in the gas stream.

The following assumptions are made:

1. The flow is one-dimensional, steady, and adiabatic with respect to the surroundings.
2. The change in temperature of the liquid is negligible; the volume of the liquid is negligible.
3. In evaluating stagnation state properties, the difference between the stagnation and static temperatures of the liquid

will be neglected, and the specific humidity of the stagnation state will be assumed identical to that of the corresponding static state.

4. The gas and vapor (products of combustion and water vapor in the aerothermopressor) obey the perfect gas and Gibbs-Dalton rules. As will be seen, the assumption of constant specific heat of each constituent gas with respect to temperature is necessary only to evaluate changes in stagnation temperature and stagnation pressure.
5. The gas (or products of combustion) has the properties of air, denoted by the subscript a. The evaporated vapor is water vapor, denoted by the subscript s.

The stagnation temperature and pressure will be defined as that temperature and pressure respectively which the stream would attain if it were decelerated reversibly and adiabatically to negligible velocity--with no additional evaporation of liquid. It should be noted that in an actual adiabatic diffusion process of a liquid-vapor mixture, some evaporation will normally occur, so that the measured stagnation pressure will differ from the value obtained from the preceding definition through evaporation effects as well as through irreversibility effects.

The steady flow energy equation written for the ideal diffusion process described above becomes

$$(h_{a0}-h_a)+\omega(h_{s0}-h_s)+\omega_\ell(h_{\ell 0}-h_\ell)=(1+\omega)\frac{V^2}{2g}+\omega_\ell\frac{V_\ell^2}{2g} \quad \cdots\cdots \quad A1$$

Introducing the average specific heat $\bar{c}_p$, defined by

$$\bar{c}_p \equiv \frac{\int_T^{T_0} c_p\,dT}{T_0-T} = \frac{h_0-h}{T_0-T}, \quad \cdots\cdots \quad A2$$

the ratio of liquid velocity to gas velocity,

$$y \equiv \frac{V_\ell}{V}, \quad \cdots\cdots \quad A3$$

and the definition of Mach number,

$$M^2 \equiv \frac{V^2}{C^2} = \frac{V^2}{kgRT} = \frac{V^2 W}{kg\bar{R}T}, \quad \cdots\cdots \quad A4$$

we obtain the value of the stagnation temperature,

$$\frac{T_0}{T} = 1 + \frac{k}{\bar{k}}\,\frac{\bar{k}-1}{2} M^2 \left(1 + \frac{\omega_0 - \omega}{1+\omega} y^2\right) + \frac{\omega_0 - \omega}{1+\omega}\,\frac{\bar{C}_{p\ell}}{\bar{C}_p}\,\frac{T_\ell}{T}\left(\frac{T_{\ell 0}}{T_\ell} - 1\right). \quad \cdots \quad A5$$

The Second Law of Thermodynamics applied to the ideal diffusion process yields

$$S_{a0} + \omega S_{s0} + (\omega_0 - \omega) S_{\ell 0} = S_a + \omega S_s + (\omega_0 - \omega) S_\ell, \quad \cdots\cdots \quad A6$$

or through the Gibbs-Dalton rule,

$$(S_0 - S) + \frac{\omega_0 - \omega}{1+\omega}(S_{\ell 0} - S_\ell) = 0. \quad \cdots\cdots \quad A7$$

The entropy change for the gas and vapor may be taken as

$$S_0 - S = \hat{C}_p \ln\frac{T_0}{T} - R\ln\frac{p_0}{p}, \quad \cdots\cdots \quad A8$$

where the average specific heat $\hat{C}_p$ is defined by

$$\hat{C}_p \equiv \frac{\int_T^{T_0} \frac{C_p\,dT}{T}}{\ln\frac{T_0}{T}} = \frac{\int_h^{h_0} \frac{dh}{T}}{\ln\frac{T_0}{T}}. \quad \cdots\cdots \quad A9$$

Assuming the change in volume of the liquid is negligible, we may write

$$S_{0\ell} - S_\ell = \hat{C}_{v\ell} \ln\frac{T_{0\ell}}{T_\ell}. \quad \cdots\cdots \quad A10$$

Combining equations A7, A8, and A10 we obtain the following expression for the stagnation pressure

$$\frac{p_0}{p} = \left(\frac{T_0}{T}\right)^{\frac{\hat{k}}{\hat{k}-1}} \left(\frac{T_{0\ell}}{T_\ell}\right)^{\frac{\omega_0-\omega}{1+\omega}\frac{\hat{C}_v}{R}} \quad \cdots\cdots \quad A11$$

The specific heat variations with temperature and the unknown liquid temperature ratio, $\frac{T_{0\ell}}{T_\ell}$, make equations A5 and A11 too complex for manipulation to obtain the influence coefficients corresponding to the stagnation temperature and stagnation pressure. It is probable that there is little loss in physical interpretation if, as noted in the preceding list of assumptions, the variation of specific heat with temperature is neglected and the change in liquid temperature is neglected. With these simplifications equations A5 and A11 reduce to the following forms:

$$\frac{T_0}{T} = 1 + \frac{k-1}{2} M^2\left(1 + \frac{\omega_0 - \omega}{1+\omega} y^2\right) \quad \cdots\cdot \; A12$$

$$\frac{p_0}{p} = \left(\frac{T_0}{T}\right)^{\frac{k}{k-1}} = \left[1 + \frac{k-1}{2} M^2\left(1 + \frac{\omega_0 - \omega}{1+\omega} y^2\right)\right]^{\frac{k}{k-1}} \cdots\cdot \; A13$$

We may now derive the influence coefficient equations for the flow under consideration. The steady flow energy equation applied the infinitesmal control surface shown in Figure 35b may be written in the form

$$dh_a + \omega dh_s + (h_s - h_\ell)d\omega + (1+\omega)d\frac{V^2}{2g} + \frac{V^2}{2g}d\omega + (\omega_0 - \omega)d\frac{V_\ell^2}{2g} - \frac{V_\ell^2}{2g}d\omega = 0 \quad \cdots A14$$

The Gibbs-Dalton rule permits the use of the relation,

$$dh_a + \omega dh_s = (c_{pa} + \omega c_{ps})dT = (1+\omega)c_p dT, \quad \cdots A15$$

Combining the definitions of liquid-gas velocity ratio, equation A3, and of Mach number, equation A4, with equations A14 and A15, we have

$$\frac{dT}{T} = -\frac{h_s - h_\ell}{c_p T}\frac{d\omega}{1+\omega} - \frac{k-1}{2}M^2\left[\frac{dV^2}{V^2} + (1-y^2)\frac{d\omega}{1+\omega} + 2\frac{\omega_0 - \omega}{1+\omega}y\frac{dV_\ell}{V}\right] \cdots A16$$

The linear momentum equation to the infinitesmal control surface may be written in the form,

$$-A\,dp - \tau\pi D\,dL = \frac{w_a(1+\omega)}{g}\left[dV + (V - V_\ell)\frac{d\omega}{1+\omega} + \frac{\omega_0 - \omega}{1+\omega}dV_\ell\right] \cdots\cdot \; A17$$

Introducing the definition of the Fanning friction factor,

$$f \equiv \frac{\tau}{\frac{\rho V^2}{2g}}, \quad \cdots\cdot A18$$

the semi-perfect gas equation of state,

$$p = \rho R T = \rho \frac{\bar{R}}{W} T, \quad \cdots\cdot A19$$

the continuity equation,

$$w_a(1+\omega) = \rho V A, \quad \cdots\cdot A20$$

and the definition of liquid-gas velocity ratio, equation A3, and the definition of Mach number, equation A4, into equation A17, we have

$$\frac{dp}{p} = -\frac{kM^2}{2}\left[4f\frac{dL}{D} + \frac{dV^2}{V^2} + 2(1-y)\frac{d\omega}{1+\omega} + 2\,\frac{\omega_o-\omega}{1+\omega}\,\frac{dV_l}{V}\right]. \quad \cdots\cdot A21$$

The semi-perfect or perfect gas equation of state, A19, may be written in the differential form

$$\frac{dp}{p} = \frac{d\rho}{\rho} + \frac{dT}{T} - \frac{dW}{W}, \quad \cdots\cdot A22$$

and the continuity equation A20 may also be written in the differential form

$$\frac{d\omega}{1+\omega} = \frac{d\rho}{\rho} + \frac{dV}{V} = \frac{d\rho}{\rho} + \frac{1}{2}\frac{dV^2}{V^2}. \quad \cdots\cdots A23$$

Equations A22 and A23 may be combined to eliminate the density terms giving

$$\frac{dp}{p} = \frac{dT}{T} + \frac{d\omega}{1+\omega} - \frac{1}{2}\frac{dV^2}{V^2} - \frac{dW}{W}. \quad \cdots\cdot A24$$

Considering the independent variables to be $\left[\frac{h_s-h_l}{c_pT}\frac{d\omega}{1+\omega}\right]$, $\left[\frac{d\omega}{1+\omega}\right]$, $\left[(1-y^2)\frac{d\omega}{1+\omega}\right]$, $\left[4f\frac{dL}{D} + 2(1-y)\frac{d\omega}{1+\omega}\right]$, $\left[\frac{\omega_o-\omega}{1+\omega}\,\frac{dV_l}{V}\right]$ and $\left[\frac{dW}{W}\right]$, equations A16, A21, and A24 may be combined to find expressions for the dependent variables $\frac{dT}{T}$, $\frac{dp}{p}$, and $\frac{dV^2}{V^2}$. The results of this manipulation are represented by the first three horizontal rows of influence coefficients in Table 2.

Expressions for the influence coefficients for the remaining independent variables of Table 2, $\frac{dM^2}{M^2}$, $\frac{dT_0}{T_0}$, and $\frac{dp_0}{p_0}$, may be found by making use of the following differential forms of equations A4, A12, and A13:

$$\frac{dM^2}{M^2} = \frac{dV^2}{V^2} + \frac{dW}{W} - \frac{dK}{K} - \frac{dT}{T} \quad \cdots\cdots \text{A25}$$

$$\frac{dT_0}{T_0} = \frac{dT}{T} + \frac{K-1}{2}\frac{M^2}{\alpha}\frac{\omega_0-\omega}{1+\omega}\left[2y\frac{dV_\ell}{V} - y^2\frac{dV^2}{V^2}\right] - \frac{K-1}{2}\frac{M^2}{\alpha}\left(\frac{1+\omega_0}{1+\omega}\right)y^2\frac{d\omega}{1+\omega}$$
$$+ \frac{K-1}{2}\frac{M^2}{\alpha}\left[1+\frac{\omega_0-\omega}{1+\omega}y^2\right]\frac{dM^2}{M^2} + \frac{KM^2}{2\alpha}\left[1+\frac{\omega_0-\omega}{1+\omega}y^2\right]\frac{dK}{K} \quad \cdots\cdots \text{A26}$$

$$\frac{dp_0}{p_0} = \frac{dp}{p} + \frac{KM^2}{2\alpha}\frac{\omega_0-\omega}{1+\omega}\left[2y\frac{dV_\ell}{V} - y^2\frac{dV^2}{V^2}\right] - \frac{KM^2}{2\alpha}\left[\frac{1+\omega_0}{1+\omega}\right]y^2\frac{d\omega}{1+\omega}$$
$$+ \frac{KM^2}{2\alpha}\left[1+\frac{\omega_0-\omega}{1+\omega}y^2\right]\frac{dM^2}{M^2} + \left[\frac{K}{(K-1)^2}\right]\left[\frac{K(\alpha-1)}{\alpha} - \ln\alpha\right]\frac{dK}{K} \quad \cdots \text{A27}$$

where the parameter α is defined as

$$\alpha \equiv \frac{T_0}{T} = 1 + \frac{K-1}{2}M^2\left[1+\frac{\omega_0-\omega}{1+\omega}y^2\right] \cdots\cdots \text{A28}$$

It is necessary merely to combine equations A25, A26 and A27 with the equations represented by the first three lines of Table 2 to obtain the equations represented by the last three lines of influence coefficients.

An interesting special case of the flow is that in which the liquid velocity is assumed to be constrained to vary such that the liquid to gas velocity ratio, y, is considered an independent parameter in place of $\frac{dV_\ell}{V}$. Differentiating the definition of y, equation A3, we have

$$dy = \frac{dV_\ell}{V} - \frac{y}{2}\frac{dV^2}{V^2} \cdots \text{A29}$$

The table of influence coefficients for this special case may be obtained by substituting from equation A29 into the independent parameters of Table 2 or the controlling equations A16, A21, A26 and A27 may be written as follows:

$$\frac{dT}{T} = -\frac{h_s - h_\ell}{c_p T}\frac{d\omega}{1+\omega} - \frac{k-1}{2}M^2\left[\left(1+\frac{\omega_0-\omega}{1+\omega}y^2\right)\frac{dV^2}{V^2} + (1-y^2)\frac{d\omega}{1+\omega} + \frac{\omega_0-\omega}{1+\omega}dy^2\right] \cdot\cdot A30$$

$$\frac{dp}{p} = -\frac{kM^2}{2}\left[4f\frac{dL}{D} + \left(1+\frac{\omega_0-\omega}{1+\omega}y^2\right)\frac{dV^2}{V^2} + 2(1-y)\frac{d\omega}{1+\omega} + 2\frac{\omega_0-\omega}{1+\omega}dy\right] \cdots A31$$

$$\frac{dT_0}{T_0} = \frac{dT}{T} + \frac{k-1}{2}\frac{M^2}{\alpha}\left[(1-y^2)\frac{d\omega}{1+\omega} + \frac{\omega_0-\omega}{1+\omega}dy^2\right] - \frac{k-1}{2}\frac{M^2}{\alpha}\left[1+\frac{\omega_0-\omega}{1+\omega}y^2\right]\frac{d\omega}{1+\omega}$$

$$+\frac{k-1}{2}\frac{M^2}{\alpha}\left[1+\frac{\omega_0-\omega}{1+\omega}y^2\right]\frac{dM^2}{M^2} + \frac{kM^2}{2\alpha}\left[1+\frac{\omega_0-\omega}{1+\omega}y^2\right]\frac{dk}{k} \quad \cdots \; A32$$

$$\frac{dp_0}{p_0} = \frac{dp}{p} + \frac{kM^2}{2\alpha}\left[(1-y^2)\frac{d\omega}{1+\omega} + \frac{\omega_0-\omega}{1+\omega}dy^2\right] - \frac{kM^2}{2\alpha}\left[1+\frac{\omega_0-\omega}{1+\omega}y^2\right]\frac{d\omega}{1+\omega}$$

$$+\frac{k}{(k-1)^2}\left[\frac{k(\alpha-1)}{\alpha} - \ln\alpha\right]\frac{dk}{k} \quad \cdots\cdot \; A33$$

Solution of equations A30, A31, A32 and A33 in combination with equations A24 and A25 yields the influence coefficients for this special case as represented in Table 3 in which the independent parameters $\left[\frac{\omega_0-\omega}{1+\omega}dy^2\right]$ and $\left[2\,\frac{\omega_0-\omega}{1+\omega}dy\right]$ replace the independent parameter $\left[\frac{\omega_0-\omega}{1+\omega}\,\frac{dV_\ell}{V}\right]$ of Table 2.

The influence coefficients of Table 3 may be specialized still farther for the case where the liquid velocity is always equal to the gas velocity ($y = \frac{V_\ell}{V} = 1$, $dy = 0$). The influence coefficients for this special case are presented in Table 4.

The special constraints imposed upon the flow represented in Tables 3 and 4 are not of physical importance since the liquid velocity will vary physically in other ways. The critical or choking mach numbers for the aerothermopressor process may therefore be inferred from the influence coefficients of Table 2. The value of the critical mach number is unity since the denominators of the influence coefficients approach zero as the local mach number approaches unity.

Appendix B

Discontinuity Analysis of a High-Velocity, Adiabatic, Constant-Area Liquid Evaporation Process

If certain assumptions are made relative to the variation of wall friction along the length of the evaporation section, it is possible to write equations relating to the properties of the stream at any cross-section to the properties of the stream at the cross-section at which the liquid is injected. These equations are useful in interpreting the experimental data taken in the aerothermopressor experiments.

The following assumptions will be made for this so-called "discontinuity" analysis:

1. The flow is one-dimensional, steady, and adiabatic with respect to the surroundings.
2. The cross-sectional area of the evaporation section is constant.
3. The injection velocity of the liquid may be neglected, and the liquid velocity at any cross-section downstream from the injection point is equal to the gas velocity at that section.
4. The liquid temperature is constant, and the volume of the liquid is negligible.
5. The gas, assumed to be air and denoted by the subscript a, and the evaporated vapor, assumed to be water vapor and denoted by the subscript s, obey the semi-perfect gas and Gibbs-Dalton rules. The specific heats of each constituent gas are assumed to vary linearly with temperature so that arithmetic average values may be used.
6. The Fanning friction factor is assumed constant. The wall shear stress at any cross-section is evaluated in terms of the properties

of the gas phase alone at that cross section. To evaluate the integrated value of the wall friction the product kpM^2 assumed to vary linearly with the length of the test section (Equa. B12).

Consider the flow enclosed by the control surface indicated in Figure 35a. The steady flow energy equation applied to the flow through this control surface may be written for each unit mass of air entering in the form

$$h_{a1} + \omega_0 h_{l1} + \frac{V_1^2}{2g} = h_{a2} + \omega_2 h_{s2} + (\omega_0 - \omega_2) h_{l2} + (1+\omega_0)\frac{V_2^2}{2g} \quad \cdots \text{B1}$$

Noting that the liquid temperature is assumed to be constant, and introducing the average specific heats given by

$$h_{a2} - h_{a1} = c_{pa12}(T_2 - T_1),$$
$$h_{s2} - h_{s1} = c_{ps12}(T_2 - T_1), \quad \cdots\cdot \text{B2}$$

equation B1 becomes

$$(c_{pa12} + \omega_2 c_{ps12})(T_2 - T_1) + \omega_2 (h_{s1} - h_{l1}) + \frac{V_1^2}{2g}\left[(1+\omega_0)\frac{V_2^2}{V_1^2} - 1\right] = 0 \quad \cdots \text{B3}$$

Defining an average specific heat for the mixture as

$$c_{p12} = \frac{c_{pa12} + \omega_2 c_{ps12}}{1+\omega_2}, \quad \cdots \text{B4}$$

and introducing the definition of mach number and the local velocity of sound,

$$M^2 \equiv \frac{V^2}{kgRT} = \frac{V^2 W}{kg\bar{R}T}, \quad \cdots\cdot \text{B5}$$

equation B3 becomes

$$\frac{T_2}{T_1} = \frac{1 - \frac{\omega_2}{1+\omega_2}\frac{h_{s1} - h_{l1}}{c_{p12}T_1} + \frac{k_1 - 1}{2} M_1^2 \frac{c_{p1}}{c_{p12}} \frac{1}{1+\omega_2}}{1 + \frac{k_1 - 1}{2} M_1^2 \frac{c_{p1}}{c_{p12}} \frac{1+\omega_0}{1+\omega_2} \frac{W_1}{W_2} \frac{k_2 M_2^2}{k_1 M_1^2}} \quad \cdots\cdot \text{B6}$$

The linear momentum equation when applied to the control surface of Figure 35a yields

$$p_1 A - p_2 A - \int_1^2 \tau \pi D \, dL = \frac{w_a}{g}\left[(1+\omega_0)V_2 - V_1\right] \quad \cdots\cdot \; B7$$

Introducing the definition of the Fanning friction factor for the gaseous phase alone,

$$\tau = \frac{\rho V^2}{2g}, \quad \cdots \; B8$$

the equation of state,

$$p = \rho \frac{\bar{R}}{W} T, \quad \cdots \; B9$$

and the continuity equation,

$$w_a(1+\omega) = \rho V A, \quad \cdots \; B10$$

together with the definition of mach number, equation B5, the linear momentum equation B7 becomes

$$1 - \frac{p_2}{p_1} = \frac{2}{p_1}\int_1^2 f K p M^2 \frac{dL}{D} + K_1 M_1^2\left[(1+\omega_0)\frac{V_2}{V_1} - 1\right] \cdots \; B11$$

The assumption is now made that f is constant and that the integral may be approximated by a linear variation of KpM^2 with length, thus

$$\int_1^2 f K p M^2 = \frac{f}{2}\left[K_1 p_1 M_1^2 + K_2 p_2 M_2^2\right] \cdots\cdot \; B12$$

Introducing B12 into B11 and rearranging, we have

$$\frac{p_2}{p_1} = \frac{1 - K_1 M_1^2\left[f\frac{L}{D} + (1+\omega_0)\frac{V_2}{V_1} - 1\right]}{1 + f\frac{L}{D} K_2 M_2^2} \quad \cdots\cdot \; B13$$

The continuity equation B10, written for the cross-sections 1 and 2 yields

$$1 + \omega_2 = \frac{\rho_2 V_2}{\rho_1 V_1} \quad \cdots \; B14$$

while the equation of state B9 written for the same cross-section yields

$$\frac{p_2}{p_1} = \frac{\rho_2}{\rho_1}\frac{T_2}{T_1}\frac{W_1}{W_2} \cdots B15$$

Combining equations B14 and B15 to eliminate the density ratio we have

$$\frac{p_2}{p_1} = \frac{T_2}{T_1}\frac{W_1}{W_2}\frac{V_1}{V_2}(1+\omega_2) \cdots\cdot B16$$

Combining equations B5, B13 and B16, to eliminate the pressure ratio, we have

$$\left[1-K_1M_1^2\left(f\frac{L}{D}-1\right)\right]\sqrt{\frac{K_1M_1^2W_2T_1}{K_2M_2^2W_1T_2}} = (1+\omega_0)K_1M_1^2+(1+\omega_2)\frac{K_1M_1^2}{K_2M_2^2}\left[1+f\frac{L}{D}K_2M_2^2\right] \cdots\cdot B17$$

Combining equations B6 and B17 to eliminate the temperature ratio, and noting that

$$\frac{W_1}{W_2}\frac{c_{p1}}{c_{p12}}\frac{K_1-1}{2} = \frac{K_1}{2}\frac{K_{12}-1}{K_{12}},$$

where K_{12} is defined by

$$\left(1+\frac{W_a}{W_s}\omega_2\right)\frac{K_{12}-1}{K_{12}} = \frac{K_{a12}-1}{K_{a12}} + \frac{W_a}{W_s}\omega_2\frac{K_{s12}-1}{K_{s12}},$$

we have the following equation for the final mach number M_2:

$$\frac{1+\omega_2}{1+\omega_0}\frac{K_1M_1^2}{K_2M_2^2} = \left[Y-K_1M_1^2\left(\frac{1+\omega_2}{1+\omega_0}f\frac{L}{D}+1\right)\right] \pm \sqrt{Y}\sqrt{Y-2K_1M_1^2\left(\frac{1+\omega_2}{1+\omega_0}f\frac{L}{D}+1\right)+K_1M_1^2\frac{K_{12}-1}{K_{12}}} \cdots\cdot B18$$

where

$$Y = \frac{\left[1+K_1M_1^2\left(1-f\frac{L}{D}\right)\right]^2}{2(1+\omega_0)\left[(1+\omega_2)\frac{W_1}{W_2}-\omega_2\frac{W_1}{W_2}\frac{h_{s1}-h_{\ell 1}}{c_{p12}T_1}+\frac{K_{12}}{K_{12}-1}\frac{K_1M_1^2}{2}\right]} \cdots\cdot B19$$

The final mach number M_2 may thus be evaluated from equations B18 and B19 for any given set of initial conditions as a function of the final specific humidity ω_2 and the wall friction term $f\frac{L}{D}$. The temperature ratio $\frac{T_2}{T_1}$ may then be computed from equation B6, and the pressure ratio $\frac{p_2}{p_1}$ from equations B5 and B13.

Gavril (2) has carried out the computation of the value of M_2 and other property ratios for a series of assumed values of the initial conditions and for various values the final specific humidity ω_2 and the wall friction term $f\frac{L}{D}$. A portion of Gavril's results are presented in Figures 32, 36 and 37 which are used to interpret the experimental data.

It is interesting to note that it is possible to predict the values corresponding to critical or choking conditions from equation B18. No solution for M_2 exists when the value of the term under the second square root sign on the right side of equation B18 is negative. The critical or choking condition is thus obtained when this term equals zero, or

$$\gamma - 2K_1M_1^2\left(\frac{1+\omega_2}{1+\omega_0}f\frac{L}{D}+1\right)+K_1M_1^2\frac{K_{12}-1}{K_{12}}=0 \quad \cdots\cdot \; B20$$

The corresponding value of the critical final mach number M_{2c} is obtained by combining equations B18 and B20, thus

$$K_2M_{2c}^2=\frac{1+\omega_2}{1+\omega_0}\left[\frac{1}{\frac{1}{K_{12}}+\frac{1+\omega_2}{1+\omega_0}f\frac{L}{D}}\right] \quad \cdots\cdots \; B21$$

The critical or choking mach number predicted by this analysis is not unity because of the special restrictions imposed by assumptions 3 and 6. (See Tables 3 and 4 and Appendix A.)

A relation between the initial mach number M_{1c} and the injection rate ω_0 corresponding to this choked condition is obtained by comgining equations B19 and B20. This combination yields

$$K_1M_{1c}^2=\frac{-\zeta\eta+\left(1-f\frac{L}{D}\right)\pm\sqrt{(\zeta\eta)^2+\zeta\left[\frac{K_{12}-1}{K_{12}}+2\eta\left(1-f\frac{L}{D}\right)\right]}}{\zeta\frac{K_{12}-1}{K_{12}}-\left(1-f\frac{L}{D}\right)^2} \quad \cdots \; B22$$

where

$$\zeta \equiv 2(1+\omega_2) f \frac{L}{D} + \frac{K_{12}+1}{K_{12}}(1+\omega_0)$$

$$\eta = \frac{W_1}{W_2}(1+\omega_2) - \frac{W_1}{W_2}\omega_2 \frac{h_{s1}-h_{e1}}{c_{p12}T_1} \quad \ldots\ldots \quad B23$$

Equation 22 establishes the value of the limiting initial mach number M_{1c} for each initial injection rate ω_0 as a function of the remaining initial conditions, the final specific humidity ω_2, and the wall friction term $f \frac{L}{D}$.

Appendix C

Discontinuity Analysis of a Low-Velocity, Adiabatic Liquid Evaporation Process

1. Constant Area Process with Variable Evaporation

The discontinuity analysis of a constant-area, adiabatic liquid evaporation process for high velocity levels has been presented in Appendix B. The resulting equations are so complex that they require laborious computation procedures for solution. When the velocities involved in the process are comparatively low, certain simplifying assumptions may be made which result in equations which are far more easily solved. The purpose of this section is to derive these "low-velocity" equations and to compare the computed results with some results from the more complex analysis.

In addition to the assumptions made in the high velocity analysis of Appendix B, the following assumptions are made:

1) The differences in the kinetic energy terms in the steady-flow energy equation are negligible in comparison to the differences in the enthalpy terms.

2) The influence of pressure variations on the density of the gas may be neglected, since small pressure variations accompany small velocity variations.

3) The definition of stagnation pressure may be simplified to the form

$$p_0 \equiv p + \rho\frac{V^2}{2g} = p\left[1 + \frac{KM^2}{2}\right]$$

The steady-flow energy equation when applied to the control surface shown in Figure 35a becomes

$$(h_{a2} - h_{a1}) + \omega_2(h_{s2} - h_{s1}) + \omega_2(h_{s1} - h_{\ell 1}) = 0 \quad \ldots . C1$$

Introducing the average specific heat of the mixture C_{p12} as defined by equation B4 of Appendix B, equation C1 may be solved directly for the temperature ratio,

$$\frac{T_2}{T_1} = 1 - \frac{\omega_2}{1+\omega_2}\left(\frac{h_{s1} - h_{\ell 1}}{c_{p12} T_1}\right) \cdots\cdot C2$$

The continuity equation may be written as

$$\frac{\rho_2}{\rho_1} = (1+\omega_2)\frac{V_1}{V_2} \cdots\cdots C3$$

The definition of mach number yields

$$M_1^2 = \frac{V_1^2 W_1}{K_1 g R T_1}$$

$$M_2^2 = \frac{V_2^2 W_2}{K_2 g R T_2} \quad \cdots\cdots C4$$

With assumption 2 above, the equation of state yields

$$\frac{\rho_2}{\rho_1} = \frac{W_2}{W_1}\frac{T_1}{T_2} \quad \cdots\cdot C5$$

The linear momentum equation written for the control surface of Figure 35a is

$$p_1 A - p_2 A - \int_1^2 \tau \pi D \, dL = \frac{w_a}{g}\left[(1+\omega_0)V_2 - V_1\right] \cdots\cdot C6$$

Making use of assumption 6 of Appendix B regarding the average wall friction force, and introducing equations C3, C4, and C5, equation C6 gives the following expression for the pressure ratio:

$$\frac{p_2}{p_1} = \frac{1 - K_1 M_1^2\left[(1+\omega_0)(1+\omega_2)\frac{W_1}{W_2}\frac{T_2}{T_1} - \left(1 + f\frac{L}{D}\right)\right]}{1 + f\frac{L}{D}(1+\omega_2)^3\frac{W_1}{W_2}\frac{T_2}{T_1}} \cdots C7$$

Equations C1 and C7 permit easy computation of the final state properties for fixed values of the initial parameters, the amount of liquid evaporated ω_2, and the wall friction term $f\frac{L}{D}$.

The stagnation pressure ratio may also be computed making use of the simplified definition of assumption 3. Thus

$$\frac{p_{02}}{p_{01}} = \frac{p_2}{p_1}\left[\frac{2+K_2M_2^2}{2+K_1M_1^2}\right] \cdots\cdots C8$$

Equations C3, C4, C5 and C8 combine to give

$$\frac{p_{02}}{p_{01}} = \frac{p_2}{p_1}\left[\frac{2+K_1M_1^2(1+\omega_2)^3\frac{W_1}{W_2}\frac{T_2}{T_1}}{2+K_1M_1^2}\right] \cdots\cdots C9$$

Making use of this low-velocity analysis, calculations of the fractional increase of static pressure $\frac{p_2 - p_1}{p_1}$ and the fractional increase of stagnation pressure $\frac{p_{02} - p_{01}}{p_{01}}$ as functions of the fraction evaporated $\frac{\omega_2}{\omega_0}$ have been made for the following parameters:

initial stagnation temperature $T_{01} = 1500$ R

initial mach number $M_1 = 0.50$

initial injection rate $\omega_0 = 0.20$ lb water/lb air

liquid temperature $T_{\ell} = 590$ R

wall friction term $f\frac{L}{D} = 0.0$ and 0.10

The results of these calculations are plotted as solid lines on Figures 36 and 37. For comparison the results of calculations by Gavril (2) which are based on the high-velocity analysis of Appendix B are plotted as dashed lines on the same figures. As might be expected, agreement is reasonably good at an initial mach number $M_1 = 0.5$, but the error increases appreciably with velocity as indicated by the curves for an initial mach number $M_1 = 0.75$. As the initial mach number is decreased, the agreement between the two types of calculation will, of course, improve.

2. Optimum Area Variation Predicted by Low-Velocity Analysis

The comparison of results of the low-velocity and high-velocity discontinuity analysis plotted in Figures 36 and 37 indicates that this analysis may be applied with some accuracy at values of the initial mach number below 0.5, and that it may be used to investigate trends in a qualitative manner above this value. In particular, the analysis may be used to investigate qualitatively the variation in stagnation pressure increase which may be expected with aerothermopressor evaporation sections of variable cross-sectional area.

To accomplish this purpose, the preceding analysis will be modified as follows:

1) The wall friction will be assumed to be negligible ($f \frac{L}{D} = 0$).
2) By any section 2, all liquid will be assumed to have evaporated ($\omega_2 = \omega_0$).
3) The static pressure will vary with cross-sectional area according to the relation

$$\frac{dp}{dA} = CA^{m} \quad \cdots\cdots C10$$

where c and m are constants for any particular process.

The energy equation C2, the definition of mach number equation C4, and the equation of state C5 apply to the variable area process as well as the constant area process. The continuity equation and the linear momentum equation have different forms.

The continuity equation becomes

$$1+\omega_0 = \frac{\rho_2}{\rho_1}\,\frac{V_2}{V_1}\,\frac{A_2}{A_1} \quad \cdots C11$$

The linear momentum equation for the control surface of Figure 35a is

$$p_1 A_1 - p_2 A_2 + \int_1^2 p\,dA = \frac{w_a}{g}\left[(1+\omega_0)V_2 - V_1\right],$$

or

$$-\int_1^2 A\,dp = \frac{w_a}{g}\left[(1+\omega_0) V_2 - V_1\right] \cdots C12$$

Equation C10 may be integrated to solve for the constant,

$$C = (m+1)\frac{p_1}{A_1^{m+1}}\,\frac{\left[\frac{p_2}{p_1}-1\right]}{\left[\left(\frac{A_2}{A_1}\right)^{m+1}-1\right]}\quad\cdots\cdots\ C13$$

Combining equations C10, C12, and C13, we have

$$p_1A_1\left[\frac{m+1}{m+2}\right]\left[\frac{p_2}{p_1}-1\right]\left[\frac{\left(\frac{A_2}{A_1}\right)^{m+2}-1}{\left(\frac{A_2}{A_1}\right)^{m+1}-1}\right] = -\frac{w_a}{g}\left[(1+\omega_0)V_2-V_1\right]\quad\cdots\ C14$$

Introducing the definition of stagnation pressure we have

$$p_{02}-p_{01} = (p_2-p_1)+\left[\frac{\rho_2V_2^2}{2g}-\frac{\rho_1V_1^2}{2g}\right]\cdots\cdots\ C15$$

Combination of equations C4, C5, C11, C14, and C15 yields the following expression for the increase in stagnation pressure:

$$\frac{p_{02}-p_{01}}{K_1p_1M_1^2} = \left[Z-\frac{1}{2}\right]-\frac{A_1}{A_2}\frac{T_2}{T_1}\frac{W_1}{W_2}(1+\omega_0)^2\left[Z-\frac{1}{2}\frac{A_1}{A_2}\right],$$

where

$$Z = \left(\frac{m+2}{m+1}\right)\left[\frac{\left(\frac{A_2}{A_1}\right)^{m+2}-1}{\left(\frac{A_2}{A_1}\right)^{m+1}-1}\right]\quad\cdots\cdots\ C16$$

Combination of equations C4, C5 and C11 yields the following relation for the mach numbers

$$\frac{K_2M_2^2}{K_1M_1^2} = (1+\omega_0)^2\frac{W_1}{W_2}\frac{T_2}{T_1}\left(\frac{A_1}{A_2}\right)^2\cdots\cdots\ C17$$

For any fixed initial state 1 and injection rate ω_0, equations C2 and C16 predict the variation in the rise in stagnation pressure $(p_{02}-p_{01})$ with area ratio $\frac{A_2}{A_1}$ and the constant m (equation C10). For a fixed value of m, the rise in stagnation pressure can be shown to increase as the area ratio $\frac{A_2}{A_1}$ is decreased. From equation C17, it may be seen that, as the area ratio

$\frac{A_2}{A_1}$ is decreased, the mach number ratio is increased. In general, an actual diffusion process becomes less efficient as the mach number at the inlet to the diffuser increases and, in addition, the preceding analysis is quantitatively applicable only at low mach numbers. Thus, the variations in the rise of stagnation pressure predicted by equation C16 with area ratio will be compared on the basis of the parameter $\frac{p_{02} - p_{01}}{p_1 K_1 M_M^2}$, where $M_M^2 = M_1^2$ for $M_2 < M_1$, and $M_M^2 = M_2^2$ for $M_2 > M_1$.

Computations of the variation of the stagnation pressure rise parameter $\frac{p_{02} - p_{01}}{p_1 K_1 M_M^2}$ with area ratio $\frac{A_1}{A_2}$ and the constant m have been made for the following initial parameters:

initial stagnation temperature, $T_{01} = 1500$ R

initial mach number, $M_1 = 0.50$

initial injection rate, $\omega_0 = 0.175$ lb water / lb air

The results of these calculations are plotted in Figure 34. As would be expected from the influence coefficients for $\frac{dp_0}{p_0}$ (Table 2), the processes in which the final mach number is equal to the initial mach number ($M_1 = M_2$) yield the largest values of stagnation pressure rise. In the region of area ratios of probable interest for the aerothermopressor work, say from $\frac{A_1}{A_2} = 1.0$ to 1.5, it may be seen that the variation in the constant m has little effect on the predicted stagnation pressure rise. This would indicate that an assumption of a linear pressure-area relation (m = 0) would probably be adequate if survey discontinuity computations of a more exact nature are undertaken.

Appendix D

Analysis of the Motion and the Evaporation of Liquid Drops Suspended in a Gas Stream

In the process analyses of Appendices A, B, and C, the actual mechanisms of liquid drop acceleration and evaporation have not been considered. The effects of the drop acceleration and evaporation on the overall process for the liquid and gas mixture are taken into account in these analyses by terms which involve the liquid velocity changes dV_λ and specific humidity changes $d\omega$. Since the entire evaporation process is in fact controlled by the heat, mass and momentum transfers between the liquid drops and the gas mixture, this section is devoted to an analysis of these effects.

The actual acceleration and evaporation process is obviously extremely complex, and several simplifying assumptions will be made during the course of the following analysis to make mathematical computation possible. As will be shown, a comparison of actual experimental data with the results of this analysis indicate that reasonable agreement is attained.

Consider a thermodynamic system which is composed of a liquid drop of mass m at any time t during the acceleration and evaporation process. At some instant of time later t + dt the system will be composed of a liquid drop of mass $m - \delta m$ (where δ indicates the absolute value of an infinitesmal change) and a mass δm of vapor. It is difficult, in fact, to identify the system at time t + dt, since the vapor will be mixed with the surrounding gas. For purposes of analysis, however, it will be assumed that the system may be identified, and, further, that the liquid and vapor are at the saturation temperature, that the infinitesmal mass of vapor moves with a velocity equal to that of the drop, and that the work of expansion of the system during this process may be evaluated in terms of the partial pressure of the vapor.

The first law of thermodynamics for this process may then be written, for the stationary observer, as

$$dE = \text{đ}Q - \text{đ}W,$$

or

$$[m-\delta m]\left[u_f + du_f + \frac{V_\ell^2}{2g} + d\frac{V_\ell^2}{2g}\right] + \delta m\left[u_g + du_g + \frac{V_\ell^2}{2g} + d\frac{V_\ell^2}{2g}\right] - m\left[u_f + \frac{V_\ell^2}{2g}\right]$$

$$= q\,dt - \left[-\mathcal{D}\,dx_\ell + p_g\left\{(m-\delta m)(v_f + dv_f) + (v_g + dv_g)\delta m - m v_f\right\}\right] \quad \ldots\ldots D1$$

Equation D1 simplifies to the form

$$m\left[du_f + p_g\,dv_f\right] + m\,d\frac{V_\ell^2}{2g} + h_{fg}\delta m = q\,dt + \mathcal{D}\,dx_\ell,$$

or, since

$$du_f + p_g\,dv_f \approx dh_f,$$

$$m\,dh_f + m\,d\frac{V_\ell^2}{2g} + h_{fg}\delta m = q\,dt + \mathcal{D}\,dx_\ell \quad \ldots\ldots D2$$

Newton's Second law applied to the same system under the assumptions stated yields

$$\mathcal{D} = \frac{m}{g}\frac{dV_\ell}{dt},$$

or

$$\mathcal{D}\,dx_\ell = \frac{m}{g}d\frac{V_\ell^2}{2g} \quad \ldots\ldots D3$$

Combination of equations D2 and D3 results in

$$m\,dh_f = q\,dt - h_{fg}\delta m \quad \ldots\ldots D4.$$

To evaluate the rate of heat transfer it is convenient to define the surface coefficient of heat transfer

$$q = h_g \pi d^2 (T - T_g), \quad D5$$

and, to evaluate rate of mass transfer, it is convenient to define the surface coefficient of mass transfer

$$\frac{\delta m}{dt} = h_m W_s \pi d^2 (p_g - p_s) \ldots\ldots D6$$

In these definitions, it is assumed that the drops are spherical in shape.

Available experimental correlations of heat and mass transfer data are difficult to interpret in light of the preceding assumptions and surface coefficient definitions. For instance, the heat transfer rate predicted by the surface coefficient of heat transfer defined in equation D5 should be, by virtue of equation D2, only that heat transfer necessary to evaporate the liquid to vapor. The heat transfer associated with changing the temperature of the vapor from saturation to stream temperature is not included. This confusion actually arises from the assumption that a thermodynamic system can be defined for this process. This difficulty does not usually arise in experimental determinations of the coefficients since usually gas-liquid temperature differences are used which are much smaller than those encountered in the aerothermopressor. It can be shown that for molecular heat and mass transfer, and for the most severe conditions encountered in the aerothermopressor, the maximum error which is involved in neglecting the rise in temperature of the vapor is about 15%. In view of the inaccuracies introduced by other assumptions of the analysis and the lack of empirical data at high relative velocities this discrepancy will be neglected.

Rivas (6) has correlated experimental data on heat, mass and momentum transfer between air and liquid drops, and, for the range of Reynolds numbers in the aerothermopressor, he finds the following correlations are satisfactory:

$$Nu_m = \frac{h_m d \bar{R} T}{D_F} \frac{\bar{p}_a}{p} = 2\, Sc^{2/9} Re_F^{1/3} \quad \text{FOR } Re_F > 1$$

$$Nu_m = 2 \quad \text{FOR } Re_F \leq 1 \ldots D7$$

$$Nu_q = \frac{h_q d}{k_F} = 2\,Pr^{2/9}\,Re_F^{1/3} \qquad \text{FOR } Re_F \geqslant 1$$

$$Nu_q = 2 \qquad \text{FOR } Re_F \leqslant 1 \quad \ldots\ldots \; D8$$

Equations D4, D5, D6, D7, and D8 may be combined to yield the following equation for the change in temperature of the liquid dT_g,

$$c_{pf}\,dT_g = dh_f = \left[h_{fg} - \left(\frac{\bar{R}T}{W_s}\right)\left(\frac{T-T_g}{p_g-p_s}\right)\left(\frac{p}{p_a}\right)\left(\frac{k_F}{D_F}\right)^{7/9}(\rho c_p)^{2/9}\right]\frac{\delta m}{m} \quad \text{FOR } Re_F \geq 1$$

$$c_{pf}\,dT_g = dh_f = \left[h_{fg} - \left(\frac{\bar{R}T}{W_s}\right)\left(\frac{T-T_g}{p_g-p_s}\right)\left(\frac{p}{p_a}\right)\left(\frac{k_F}{D_F}\right)\right]\frac{\delta m}{m} \quad \text{FOR } Re_F \leq 1$$

$$\ldots\ldots \; D9$$

Preliminary calculations have indicated that the change in liquid temperature may be neglected for the major portion of the aerothermopressor process. If the temperature change is neglected, equation D9 allows the computation of the liquid temperature from

$$\left(\frac{k_F}{D_F}\right)^{7/9}\left(\frac{\bar{R}T}{W_s}\right)\left(\frac{T-T_g}{p_g-p_s}\right)\left(\frac{p}{p_a}\right)(\rho c_p)^{2/9} = h_{fg} \qquad \text{FOR } Re_F \geqslant 1$$

$$\left(\frac{k_F}{D_F}\right)\left(\frac{\bar{R}T}{W_s}\right)\left(\frac{T-T_g}{p_g-p_s}\right)\left(\frac{p}{p_a}\right) = h_{fg} \qquad \text{FOR } Re_F \leqslant 1 \quad \ldots\ldots \; D10$$

With the assumption that the change in liquid temperature may be neglected, equations D4, D5, and D7 may be combined to give an expression for the change in drop diameter with time,

$$\frac{dd}{dt} = -\frac{4k_F}{\rho_f h_{fg} d}(T-T_g)\,|\,Re_F\,|^{1/3} \qquad \text{FOR } Re_F \geqslant 1$$

$$\frac{dd}{dt} = -\frac{4k_F}{\rho_f h_{fg} d}(T-T_g) \qquad \text{FOR } Re_F \leqslant 1 \quad \ldots\ldots \; D11$$

The specific humidity of the stream is given by

$$\frac{w_f}{w_a} = \frac{w_{f_0} - w_f}{w_a} = \omega_0 - \omega = \frac{N\pi d^3}{6}\rho_f\,, \quad \ldots\ldots \; D12$$

where N is the number of liquid drops per unit mass rate of flow of air. If the assumption is made that there is no change in the number of drops per unit mass rate of flow of air, the change in specific humidity may be computed from equation D12,

$$\frac{d\omega}{\omega_0-\omega} = -3\,\frac{dd}{d} \quad \dots\dots \; D13$$

This assumption implies that the drop size is uniform, that there is no fragmentation or coagulation of the drops, and that no drops impinge on the walls of the evaporation section.

Rivas (6) has also correlated values of the coefficients of drag for solid spheres in gas streams and recommends the following correlations:

$$C_D = \frac{D}{\frac{\rho(V-V_L)^2}{2g}\pi d^2} = 24\,|Re_F|^{-2/3} \qquad \text{FOR } Re_F \geq 1$$

$$C_D = 24\,|Re_F|^{-1} \qquad \text{FOR } Re_F \leq 1 \quad \dots\dots \; D14$$

These correlations are subject to inaccuracies similar to those discussed in connection with the heat and mass transfer surface coefficient equations.

Combination of equations D3 and D14 allows the prediction of change in liquid velocity from

$$\frac{dV_L}{dt} = 18\,\frac{\mu_F}{\rho_L d^2}(V-V_L)\,|Re_F|^{1/3} \qquad \text{FOR } Re_F \geq 1$$

$$\frac{dV_L}{dt} = 18\,\frac{\mu_F}{\rho_L d^2}(V-V_L) \qquad \text{FOR } Re_F \leq 1 \quad \dots\dots \; D15$$

Equations D10, D11, D13, and D15 predict the effects of heat, mass, and momentum transfer between the liquid droplets and the liquid-vapor mixture. Combination of these equations with the equations predicting the changes in stream properties from Appendix A (Table 2) permits the complete computation of an infinitesmal portion of the aerothermopressor process, subject to the limitations of the stated assumptions.

If the equations are to be integrated over the entire evaporation section, it is necessary to introduce the additional assumption that upon injection of the water into the gas stream, a homogeneous distribution of droplets is formed throughout the gas instantaneously. This assumption necessarily leads to large errors in the prediction of the behavior of the first portion of evaporation process.

It is also necessary to predict the initial diameter of the droplets which are formed upon injection. The results of the computation are obviously very much effected by errors in the prediction of this drop size since the characteristics of the entire acceleration and evaporation process are extremely sensitive to drop diameter. The work of Plender (7) indicates that the drop size prediction equation of Nukiyama and Tanasawa (8) gives reasonable values. This equation is

$$d = \frac{5300}{V}, \qquad \ldots\ldots \quad D16$$

where d is the surface to volume mean diameter of the drops in microns (μ) which are formed when liquid water is injected in a gas stream whose velocity relative to the drops is V meters per second.

The system of controlling equations is so complex that they can be integrated only by numerical techniques. Gavril (2) is at the time of this writing accomplishing this integration of a somewhat more general set of equations for a wide range of initial conditions with the Whirlwind computer. The writer has completed only one numerical integration using the simplest, non-iterative techniques.

The values of the parameters chosen for this integration are as follows:

initial stagnation temperature, $T_{01} = 1500$ R

initial stagnation pressure, $p_{01} = 14.7$ psia

initial mach number, $M_1 = 0.500$

initial injection rate, $\omega_0 = 0.20$ lb water/lb air

Fanning friction factor, $f = 0.005$

initial drop size (equation D16), $d_1 = 19.0\,\mu = 62.3\,(10^{-6})$ ft.

liquid temperature (equation D10), $T_g = 582$ R

diameter of evaporation section, $D = 2.125$ in.

The results of this integration are plotted on Figure 26 together with corresponding experimental data. The discrepancies between the theoretical and experimental results are discussed in Section III D.

Bibliography

1. "The Mechanics and Thermodynamics of Steady, One-Dimensional Gas Flow", by Ascher H. Shapiro and William R. Hawthorne, Journal of Applied Mechanics, Vol. 14, No. 4, December, 1947.

2. "A Theoretical Investigation of the Thermodynamic and Dynamic Effects of Water Injection into High-Velocity, High-Temperature Gas Streams", by Bruce D. Gavril, Thesis for degree of Doctor of Science, M.I.T., in preparation.

3. "The Design, Construction, and Preliminary Test of the Aero-Thermoprex", by R. A. Hawkins and L. V. Mowell, Thesis for the degree of Naval Engineer, M.I.T., 1949.

4. "Small-Scale Constant Area Test of an Aerothermopressor", by P. A. Gisvold, Jr., and J. C. Matheson, Thesis for degree of Naval Engineer, M.I.T., 1952.

5. "Techniques for Measuring Specific Humidity of the Gas Phase of a High-Temperature, High-Velocity, Two-Phase Stream of Air and Water", by Howard K. Larson, Thesis for degree of Master of Science, M.I.T., in preparation.

6. "A Theoretical Investigation of Liquid Droplet Evaporation in a High Velocity Stream", by Miguel A. Rivas, Jr., Thesis for the degree of Bachelor of Science, M.I.T., 1951.

7. "Atomization of Water Sprays in a High-Speed Air Stream", Thesis for degree of Master of Science, M.I.T., 1952.

8. "An Experiment on the Atomization of Liquid by Means of an Air Stream", by S. Nukyama and Y. Tanasawa, Trans. S.M.E. Japan, Vol. 4, 1938, Reports 1-6.

9. "Gas Tables", by J. H. Keenan and J. Kaye, John Wiley and Sons, Inc., New York, 1948.

10. "Analysis of Various Systems for Supersonic Wind Tunnels", by W. R. Hawthorne, J. Kaye, J. H. Keenan, A. H. Shapiro and K. R. Wadleigh, Meteor Report UAC-23, Project Meteor, M.I.T., June, 1948.

Nomenclature

Symbols	
A	area
C	constant or velocity of sound
$C_{\mathcal{D}}$	coefficient of drag
c_p	specific heat at constant pressure
c_v	specific heat at constant volume
D	diameter of evaporation section or diffusivity
$\mathcal{D}$	drag force
d	exact differential operator
$đ$	inexact differential operator
d	liquid drop diameter
E	internal energy
f	Fanning friction factor
g	proportionality constant in Newton's Second Law
h	enthalpy
h_m	surface coefficient of mass transfer
h_q	surface coefficient of heat transfer
k	ratio of specific heats, $k = c_p \div c_v$
k	thermal conductivity
L	distance from plane of injection
M	mach number
m	constant or mass of liquid drop
N	number of drops per unit mass rate of flow of gas
Nu_m	Nusselt number for mass transfer
Nu_q	Nusselt number for heat transfer
Pr	Prandtl number
p	pressure
Q	quantity of heat
q	rate of heat transfer
R	gas constant
$\bar{R}$	universal gas constant

Symbols

Re	Reynold's number
r	radius
Sc	Schmidt number
s	entropy
T	absolute temperature
t	time
u	internal energy
V	velocity
v	specific volume
W	quantity of work or molecular weight
w	mass rate of flow
x	distance
Y	defined by equation on pages 24 and 55
y	ratio of liquid velocity to gas velocity
Z	defined by equation C16, page 82
α	defined by equation A28, page 69
γ	defined by equation B19, page 75
δ	absolute value of differential operator
η	defined by equation B23, page 77
ξ	defined by equation B23, page 77
ρ	density
μ	viscosity
τ	wall shear stress
ω	specific humidity
ω_0	initial injection rate, ratio of mass rate of flow of liquid to mass rate of flow of gas

Subscripts

0	stagnation state
1	state at entrance to evaporation section (Figure 1)
2	state at entrance to diffuser (Figure 1)
3	state at exit of diffuser (Figure 1)

Subscripts

a	air or gas
c	critical or choking
F	value for film temperature, $\frac{T+T_g}{2}$
f	saturated liquid water
fg	change from saturated liquid to saturated vapor
g	saturated water vapor
l	liquid
M	maximum
s	superheated water vapor

List of Tables and Figures

Tables

Figures

Table 1

Tabulation of Types of Water Injection Nozzles Utilized in Small Scale Aerothermopressor

No.	Description	Sketch
1	Single axial-flow jet, 0.140 in. diameter, centrally located at air nozzle exit plane.	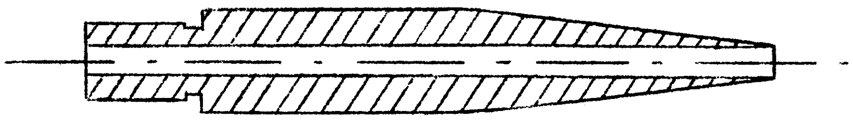
2	Impingement sheet nozzle, centrally located at air nozzle exit plane.	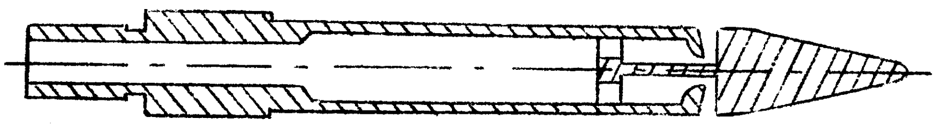
3	0.125" OD, 0.110" ID axial jets; one in center; six equally displaced on circumference of circle with d = 1 1/4 in, centrally located at air nozzle exit plane.	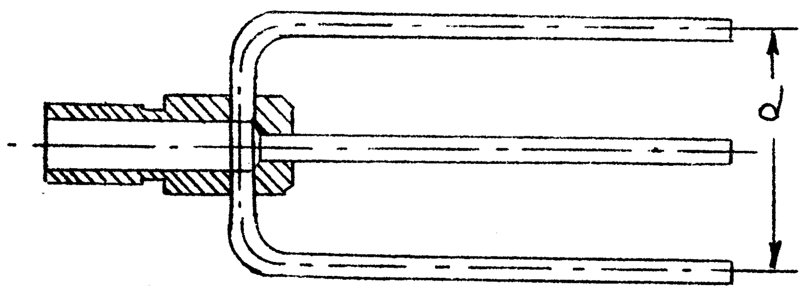
6	0.072" OD, 0.054" ID axial jets; one in center; six equally displaced on circumference of 1 1/4 in circle; six equally displaced on circumference of 5/8 in circle, centrally located at air nozzle exit plane.	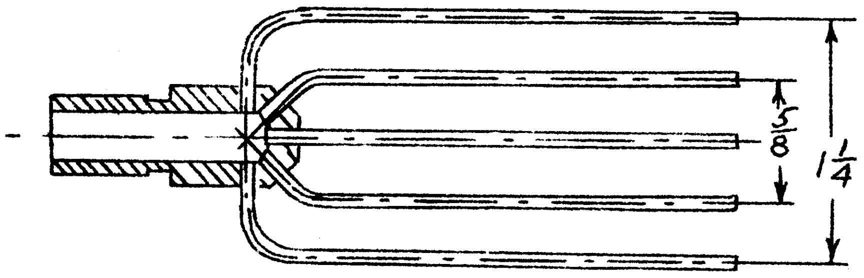
7	Six symmetrically placed 0.030" diameter radial holes 3/8" downstream from air nozzle exit plane.	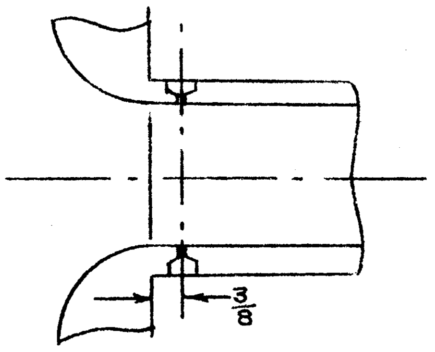
16	Centrally located axial swirl nozzles (modified Sprayco No. 3B) at air nozzle exit plane.	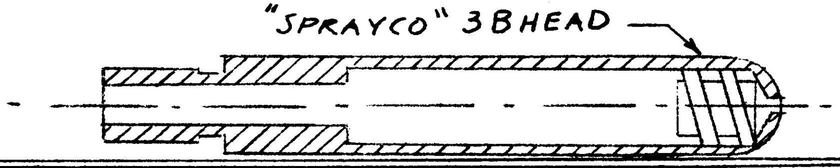

No.	Description	No.	Description
4	Same as No. 3 with circumference of circle d = 1 1/8 in.	13	Same as nozzle No. 8 but with 0.040" diameter radial holes.
5	Same as No. 3 with circumference of circle d = 1 in.	14	Combination of nozzle Nos. 1 and 13 with equal water flows in each.
8	Three symmetrically placed 0.030" diameter radial holes 3/8" downstream from nozzle exit plane and the same 10 3/4" downstream from exit plane.	15	Six symmetrically placed 0.024" diameter radial holes 3/8" downstream from air nozzle exit plane in combination with nozzle No. 1.
9	Combination of nozzle Nos. 1 and 8 with equal water flows in each.	17	Same as nozzle No. 15 but with nozzle No. 16 replacing nozzle No. 1.
10	Combination of nozzles Nos. 1 and 7 with equal rate flows in each.	18	Same as nozzle No. 3 but with 0.072" OD, 0.054" ID tubing.
11	Same as nozzle No. 7 but with 0.040" diameter radial holes.	19	Same as nozzle No. 18 but located 1 1/2" upstream from air nozzle exit plane.
12	Combination of nozzles Nos. 1 and 11 with equal water flows in each.	20	Same as nozzle No. 3 but located 1 1/2" upstream from air nozzle exit plane.

TABLE 2

INFLUENCE COEFFICIENTS FOR ADIABATIC, CONSTANT AREA LIQUID EVAPORATION PROCESS

INDEP. VAR. → DEP. VAR. ↓	$\frac{h_s - h_f}{C_p T}\ \frac{d\omega}{1+\omega}$	$\frac{d\omega}{1+\omega}$	$(1-y^2)\ \frac{d\omega}{1+\omega}$	$4f\frac{dL}{D} + 2(1-y)\frac{d\omega}{1+\omega}$	$\frac{\omega_0 - \omega}{1+\omega}\ \frac{dV_l}{V}$	$\frac{dW}{W}$	$\frac{dk}{k}$
$\frac{dT}{T}$	$\frac{kM^2-1}{1-M^2}$	$-\frac{(k-1)M^2}{1-M^2}$	$\frac{(k+1)M^2(kM^2-1)}{2(1-M^2)}$	$-\frac{k(k-1)M^4}{2(1-M^2)}$	$-\frac{(k-1)M^2}{1-M^2}\left[y+(1-y)kM^2\right]$	$\frac{(k-1)M^2}{1-M^2}$	0
$\frac{dp}{p}$	$\frac{kM^2}{1-M^2}$	$-\frac{kM^2}{1-M^2}$	$\frac{k(k-1)M^4}{2(1-M^2)}$	$-\frac{kM^2\left[1+(k-1)M^2\right]}{2(1-M^2)}$	$-\frac{kM^2\left[1+(k-1)M^2(1-y))\right]}{1-M^2}$	$\frac{kM^2}{1-M^2}$	0
$\frac{dV^2}{V^2}$	$-\frac{2}{1-M^2}$	$\frac{2}{1-M^2}$	$-\frac{(k-1)M^2}{1-M^2}$	$\frac{kM^2}{1-M^2}$	$\frac{2kM^2-2y(k-1)M^2}{1-M^2}$	$-\frac{2}{1-M^2}$	0
$\frac{dM^2}{M^2}$	$-\frac{kM^2+1}{1-M^2}$	$\frac{2+(k-1)M^2}{1-M^2}$	$-\frac{(k-1)M^2(kM^2+1)}{2(1-M^2)}$	$\frac{kM^2\left[2+(k-1)M^2\right]}{2(1-M^2)}$	$\frac{kM^2}{1-M^2}\left[2+(k-1)M^2 - \frac{k-1}{k}y(1+kM^2)\right]$	$-\frac{kM^2+1}{1-M^2}$	-1
$\frac{dT_0}{T_0}$	$-\frac{1}{\alpha}$	$-\frac{(k-1)M^2\left(\frac{1+\omega_0}{1+\omega}\right)y^2}{2\alpha}$	$-\frac{(k-1)M^2}{2\alpha}$	0	0	$\frac{\alpha-1}{\alpha}$	$\frac{1}{k-1}\ \frac{\alpha-1}{\alpha}$
$\frac{dp_0}{p_0}$	$\frac{k}{k-1}\ \frac{\alpha-1}{\alpha}$	$-\frac{kM^2\left(\frac{1+\omega_0}{1+\omega}\right)y^2}{2\alpha}$	$\frac{kM^2}{2}\ \frac{\alpha-1}{\alpha}$	$-\frac{kM^2}{2}$	$-(1-y)kM^2$	$\frac{k}{k-1}\ \frac{\alpha-1}{\alpha}$	$\frac{k}{(k-1)^2}\left[\frac{\alpha-1}{\alpha} - \ln\alpha\right]$
	$\frac{T_0}{T} \equiv \alpha \equiv 1 + \frac{k-1}{2}M^2\left(1+\frac{\omega_0-\omega}{1+\omega}y^2\right)$				$\frac{p_0}{p} \equiv \left(\frac{T_0}{T}\right)^{\frac{k}{k-1}} = \alpha^{\frac{k}{k-1}}$	$y \equiv \frac{V_l}{V}$	

TABLE 3

INFLUENCE COEFFICIENTS FOR ADIABATIC, CONSTANT-AREA AEROTHERMOPRESSOR

SPECIAL CASE WHERE $y \equiv V_l/V$ IS INDEPENDENT

INDEP. VAR. → DEP. VAR. ↓	$\frac{h_s-h_f}{c_pT}\frac{d\omega}{1+\omega}$	$\frac{d\omega}{1+\omega}$	$(1-y^2)\frac{d\omega}{1+\omega}+\frac{\omega_0-\omega}{1+\omega}dy^2$	$4f\frac{dL}{D}+2(1-y)\frac{d\omega}{1+\omega}+2\frac{\omega_0-\omega}{1+\omega}dy$	$\frac{dW}{W}$	$\frac{dk}{k}$
$\frac{dT}{T}$	$\frac{\beta-1}{\alpha-\beta}$	$-\frac{\alpha-1}{\alpha-\beta}$	$-\frac{k-1}{2}M^2\frac{\beta-1}{\alpha-\beta}$	$-\frac{kM^2}{2}\frac{\alpha-1}{\alpha-\beta}$	$\frac{\alpha-1}{\alpha-\beta}$	0
$\frac{dp}{p}$	$\frac{\beta-\frac{1}{2}}{\alpha-\beta}$	$-\frac{\beta-\frac{1}{2}}{\alpha-\beta}$	$\frac{k-1}{2}M^2\frac{\beta-\frac{1}{2}}{\alpha-\beta}$	$-\frac{kM^2}{2}\frac{\alpha-\frac{1}{2}}{\alpha-\beta}$	$\frac{\beta-\frac{1}{2}}{\alpha-\beta}$	0
$\frac{dV^2}{V^2}$	$-\frac{1}{\alpha-\beta}$	$\frac{1}{\alpha-\beta}$	$-\frac{k-1}{2}M^2\frac{1}{\alpha-\beta}$	$\frac{kM^2}{2}\frac{1}{\alpha-\beta}$	$-\frac{1}{\alpha-\beta}$	0
$\frac{dM^2}{M^2}$	$-\frac{\beta}{\alpha-\beta}$	$+\frac{\alpha}{\alpha-\beta}$	$-\frac{k-1}{2}M^2\frac{\beta}{\alpha-\beta}$	$\frac{kM^2}{2}\frac{\alpha}{\alpha-\beta}$	$-\frac{\beta}{\alpha-\beta}$	-1
$\frac{dT_0}{T_0}$	$-\frac{1}{\alpha}$	$-\frac{\alpha-1}{\alpha}$	$-(k-1)M^2\frac{\beta-1}{\alpha-\beta}$	0	$\frac{\alpha-1}{\alpha}$	$\frac{1}{k-1}\frac{\alpha-1}{\alpha}$
$\frac{dp_0}{p_0}$	$\frac{\frac{k-\alpha}{k-1}\beta-\frac{\alpha}{2}}{\alpha(\alpha-\beta)}$	$-\frac{k}{k-1}\frac{\alpha-1}{\alpha}$	$\frac{kM^2}{4}\left[\frac{1-M^2\left(1+\frac{\omega_0-\omega}{1+\omega}y\right)}{\alpha-\beta}\right]$	$-\frac{kM^2}{4}\left[\frac{1-M^2\left(1+\frac{\omega_0-\omega}{1+\omega}y^2\right)}{\alpha-\beta}\right]$	$\frac{\frac{k-\alpha}{k-1}\beta-\frac{\alpha}{2}}{\alpha(\alpha-\beta)}$	$\frac{k}{(k-1)^2}\left[\frac{\alpha-1}{\alpha}-\ln\alpha\right]$
	$\frac{T_0}{T}\equiv\alpha\equiv 1+\frac{k-1}{2}M^2\left(1+\frac{\omega_0-\omega}{1+\omega}y^2\right)$ $\quad$ $\frac{p_0}{p}\equiv\left(\frac{T_0}{T}\right)^{\frac{k-1}{k}}=(\alpha)^{\frac{k-1}{k}}$ $\quad$ $\beta\equiv\frac{1}{2}+\frac{kM^2}{2}\left(1+\frac{\omega_0-\omega}{1+\omega}y\right)$					

TABLE 4

INFLUENCE COEFFICIENTS FOR ADIABATIC, CONSTANT-AREA AEROTHERMOPRESSOR

SPECIAL CASE WHERE $y \equiv V_\ell/V = 1$, $dV_\ell = dV$

INDEP. VAR. → DEP. VAR. ↓	$\frac{h_s-h_f}{c_pT}\frac{d\omega}{1+\omega}$	$\frac{d\omega}{1+\omega}$	$4f\frac{dL}{D}$	$\frac{dW}{W}$	$\frac{dk}{k}$
$\frac{dT}{T}$	$-\frac{1-kM^2\left(\frac{1+\omega_0}{1+\omega}\right)}{1-M^2\left(\frac{1+\omega_0}{1+\omega}\right)}$	$-\frac{(k-1)M^2\left(\frac{1+\omega_0}{1+\omega}\right)}{1-M^2\left(\frac{1+\omega_0}{1+\omega}\right)}$	$-\frac{kM^2}{2}\left[\frac{(k-1)M^2\left(\frac{1+\omega_0}{1+\omega}\right)}{1-M^2\left(\frac{1+\omega_0}{1+\omega}\right)}\right]$	$+\frac{(k-1)M^2\left(\frac{1+\omega_0}{1+\omega}\right)}{1-M^2\left(\frac{1+\omega_0}{1+\omega}\right)}$	0
$\frac{dp}{p}$	$\frac{kM^2\left(\frac{1+\omega_0}{1+\omega}\right)}{1-M^2\left(\frac{1+\omega_0}{1+\omega}\right)}$	$-\frac{kM^2\left(\frac{1+\omega_0}{1+\omega}\right)}{1-M^2\left(\frac{1+\omega_0}{1+\omega}\right)}$	$-\frac{kM^2}{2}\left[\frac{1+(k-1)M^2\left(\frac{1+\omega_0}{1+\omega}\right)}{1-M^2\left(\frac{1+\omega_0}{1+\omega}\right)}\right]$	$\frac{kM^2\left(\frac{1+\omega_0}{1+\omega}\right)}{1-M^2\left(\frac{1+\omega_0}{1+\omega}\right)}$	0
$\frac{dV^2}{V^2}$	$-\frac{2}{1-M^2\left(\frac{1+\omega_0}{1+\omega}\right)}$	$\frac{2}{1-M^2\left(\frac{1+\omega_0}{1+\omega}\right)}$	$\frac{kM^2}{2}\left[\frac{2}{1-M^2\left(\frac{1+\omega_0}{1+\omega}\right)}\right]$	$-\frac{2}{1-M^2\left(\frac{1+\omega_0}{1+\omega}\right)}$	0
$\frac{dM^2}{M^2}$	$-\frac{1+kM^2\left(\frac{1+\omega_0}{1+\omega}\right)}{1-M^2\left(\frac{1+\omega_0}{1+\omega}\right)}$	$\frac{2+(k-1)M^2\left(\frac{1+\omega_0}{1+\omega}\right)}{1-M^2\left(\frac{1+\omega_0}{1+\omega}\right)}$	$\frac{kM^2}{2}\left[\frac{2+(k-1)M^2\left(\frac{1+\omega_0}{1+\omega}\right)}{1-M^2\left(\frac{1+\omega_0}{1+\omega}\right)}\right]$	$-\frac{1+kM^2\left(\frac{1+\omega_0}{1+\omega}\right)}{1-M^2\left(\frac{1+\omega_0}{1+\omega}\right)}$	-1
$\frac{dT_0}{T_0}$	$-\frac{2}{2+(k-1)M^2\left(\frac{1+\omega_0}{1+\omega}\right)}$	$-\frac{(k-1)M^2\left(\frac{1+\omega_0}{1+\omega}\right)}{2+(k-1)M^2\left(\frac{1+\omega_0}{1+\omega}\right)}$	0	$+\frac{(k-1)M^2\left(\frac{1+\omega_0}{1+\omega}\right)}{2+(k-1)M^2\left(\frac{1+\omega_0}{1+\omega}\right)}$	$\frac{M^2\left(\frac{1+\omega_0}{1+\omega}\right)}{2+(k-1)M^2\left(\frac{1+\omega_0}{1+\omega}\right)}$
$\frac{dp_0}{p_0}$	$\frac{kM^2\left(\frac{1+\omega_0}{1+\omega}\right)}{2+(k-1)M^2\left(\frac{1+\omega_0}{1+\omega}\right)}$	$-\frac{kM^2\left(\frac{1+\omega_0}{1+\omega}\right)}{2+(k-1)M^2\left(\frac{1+\omega_0}{1+\omega}\right)}$	$-\frac{kM^2}{2}$	$\frac{kM^2\left(\frac{1+\omega_0}{1+\omega}\right)}{2+(k-1)M^2\left(\frac{1+\omega_0}{1+\omega}\right)}$	$\frac{K}{K-1}\left\{\frac{M^2\left(\frac{1+\omega_0}{1+\omega}\right)}{2+(K-1)M^2\left(\frac{1+\omega_0}{1+\omega}\right)}\right.$
					$\left.-\frac{1}{K-1}\ln\left[1+\frac{K-1}{2}M^2\left(\frac{1+\omega_0}{1+\omega}\right)\right]\right\}$

FIGURE 1

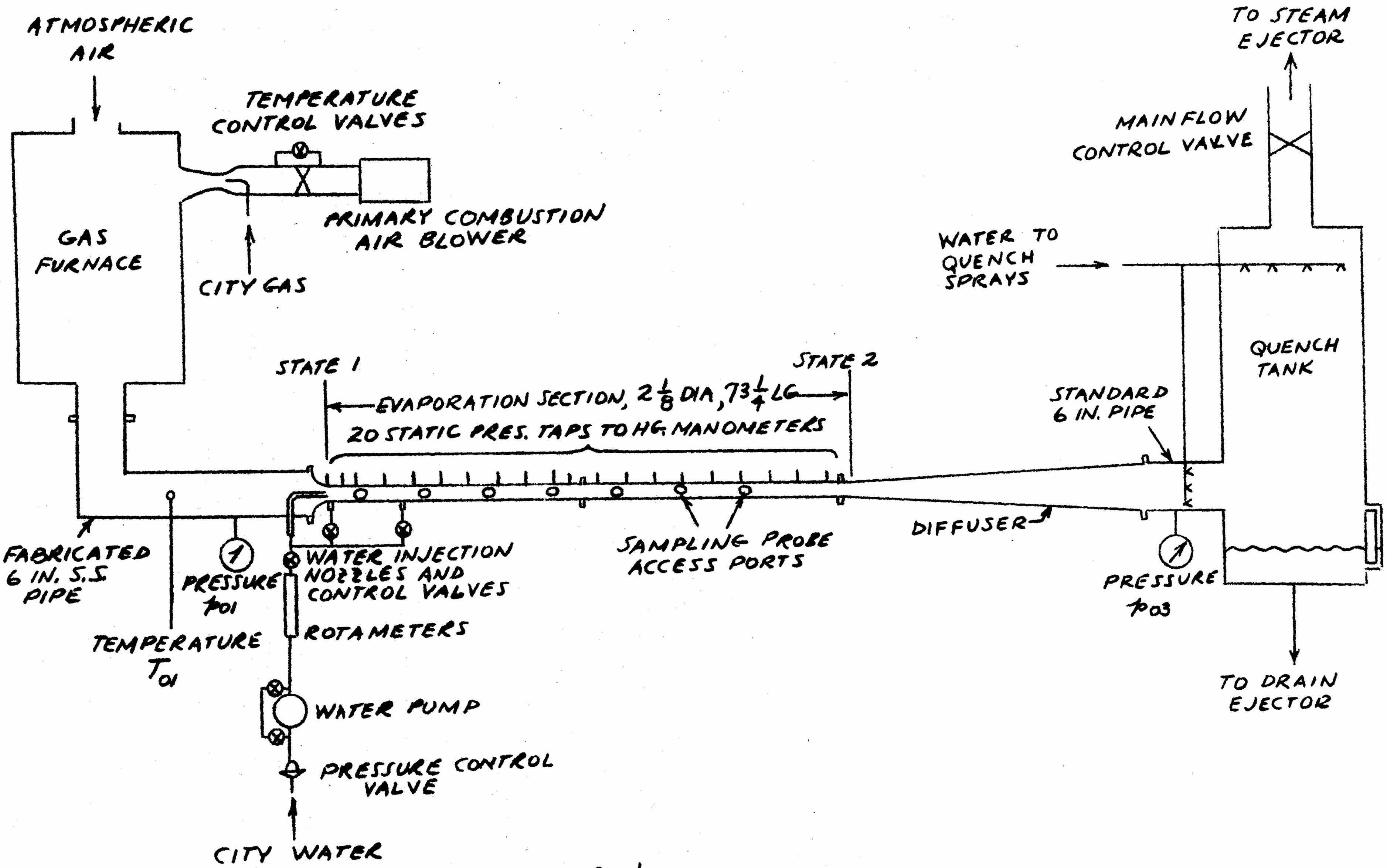

FIGURE 1

SCHEMATIC LAYOUT OF MAIN TEST EQUIPMENT

FIGURE 2

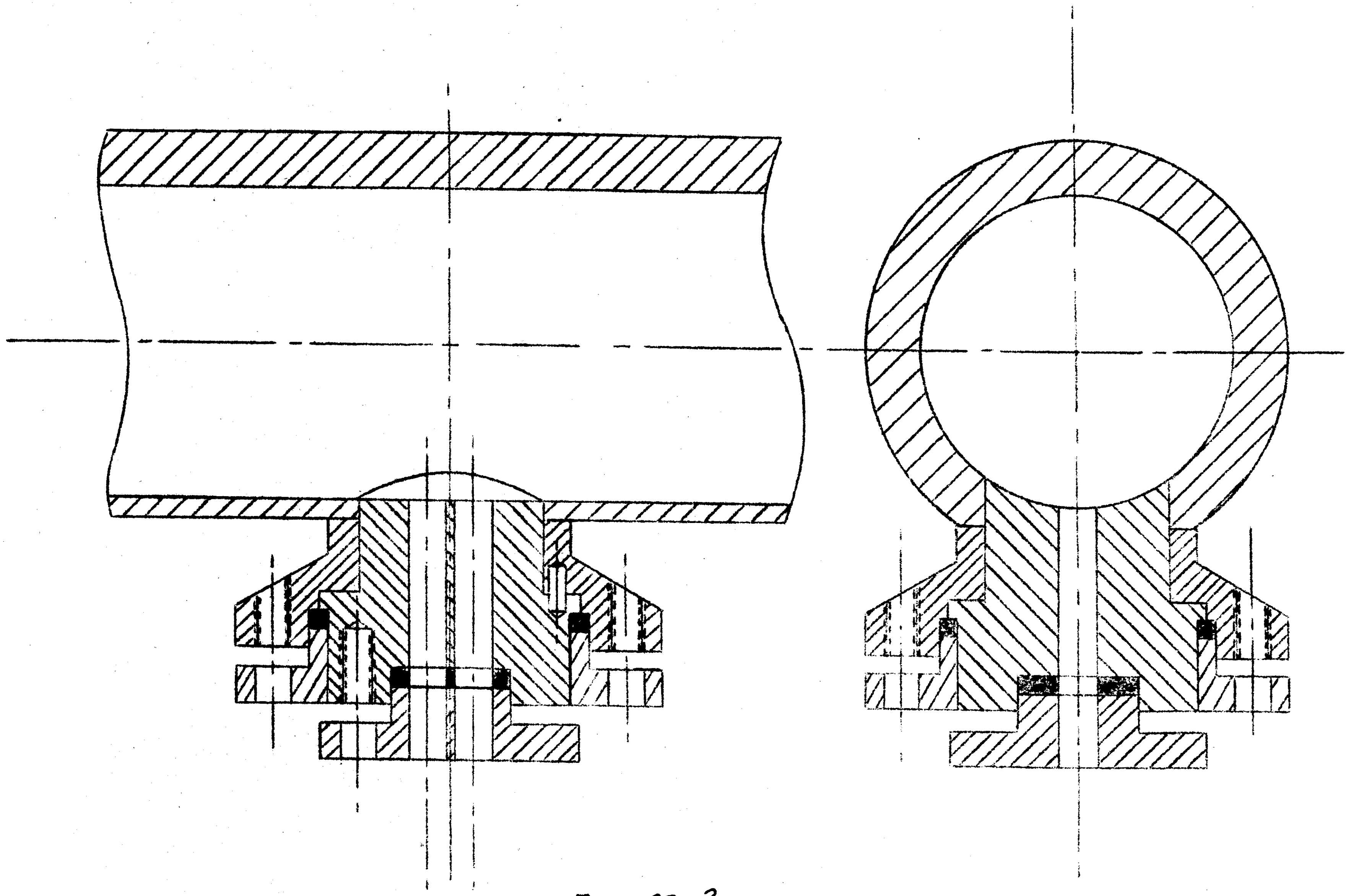

FIGURE 2

DETAILS OF HUMIDITY PROBE ACCESS PORT AND GLAND

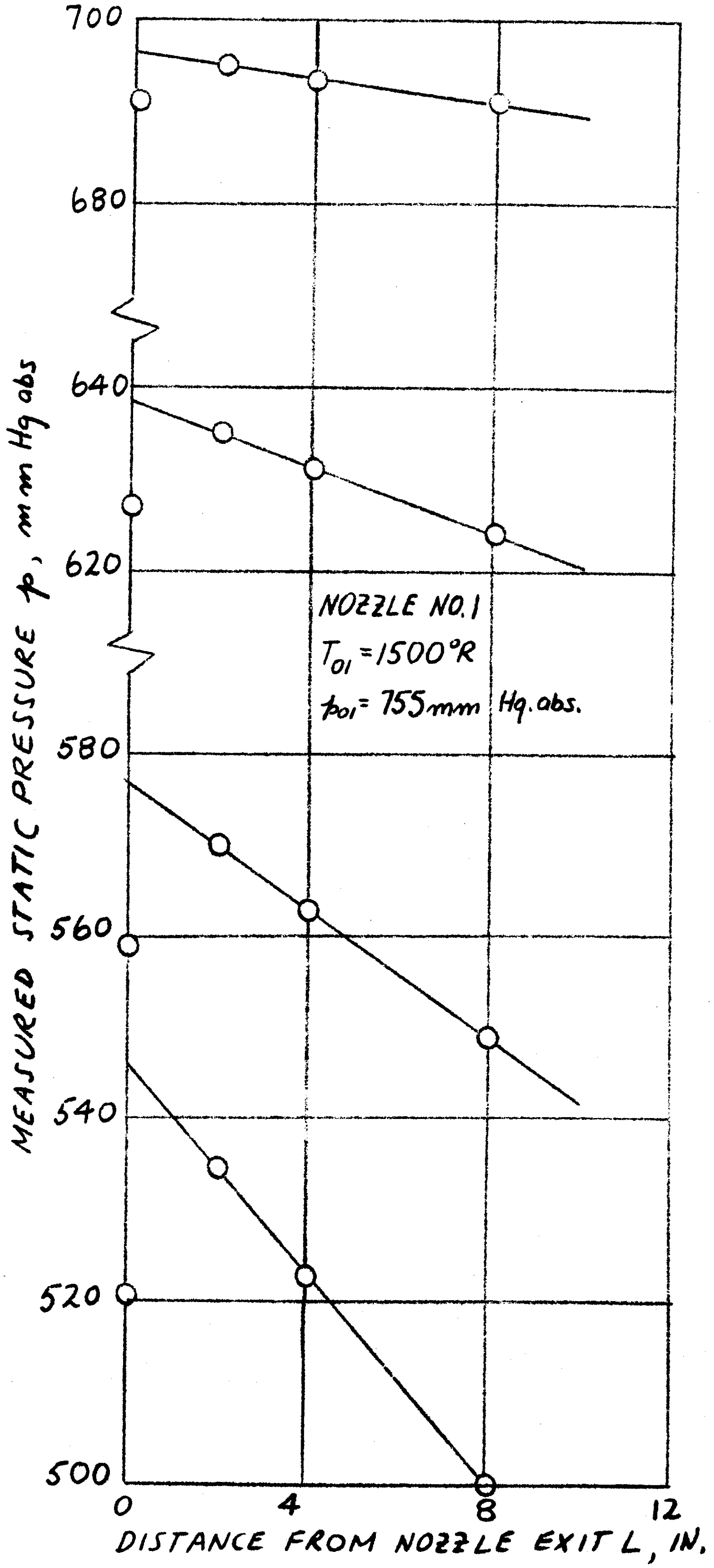

FIGURE 3

TYPICAL STATIC PRESSURE VARIATION WITH LENGTH AT ENTRANCE OF AEROTHERMOPRESSOR EVAPORATION SECTION

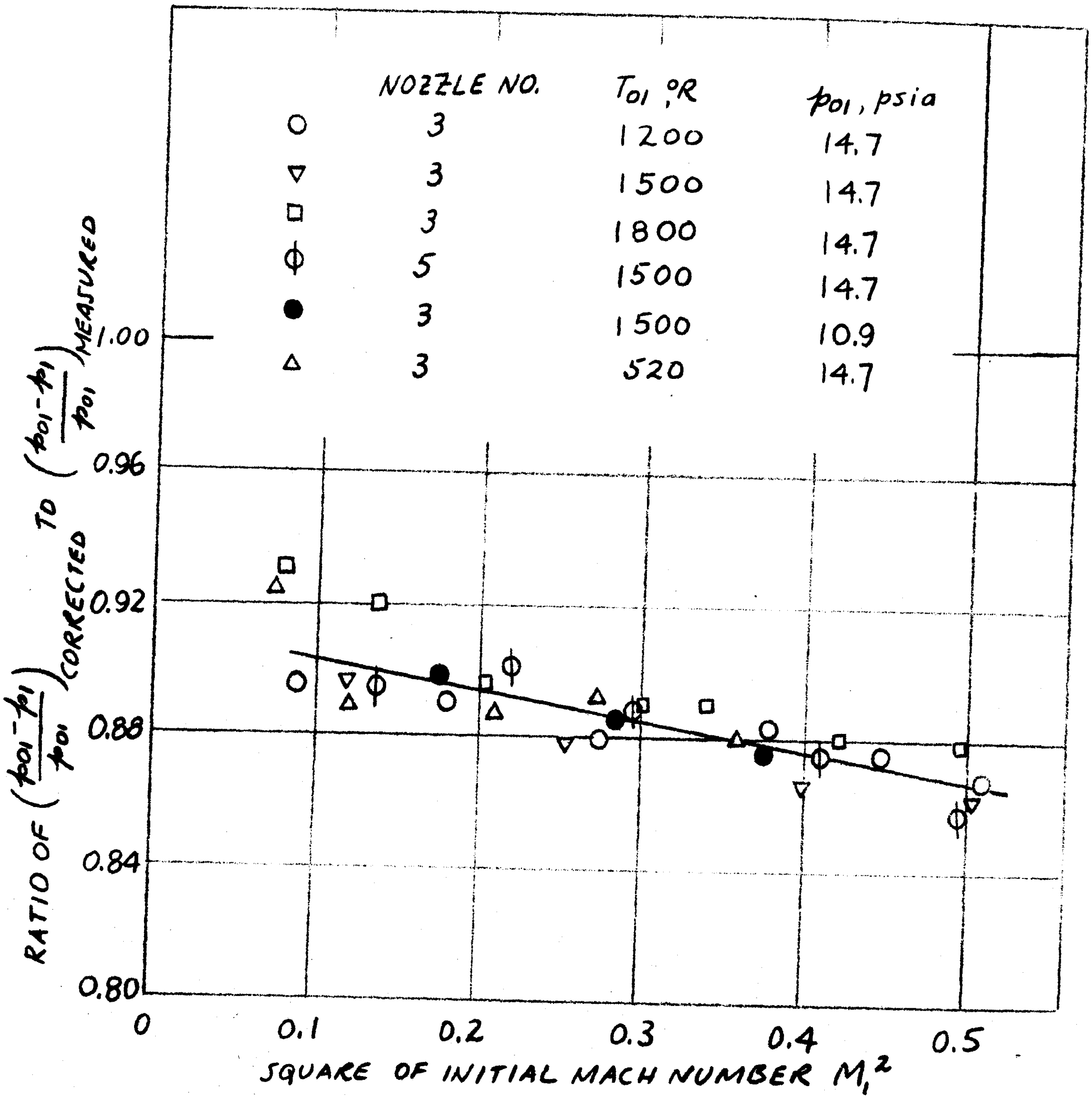

FIGURE 4

CORRECTION FACTOR FOR AEROTHERMOPRESSOR ENTRANCE NOZZLE WITH WATER INJECTION NOZZLE NO. 3 OR 5 – AS A FUNCTION OF INITIAL MACH NUMBER

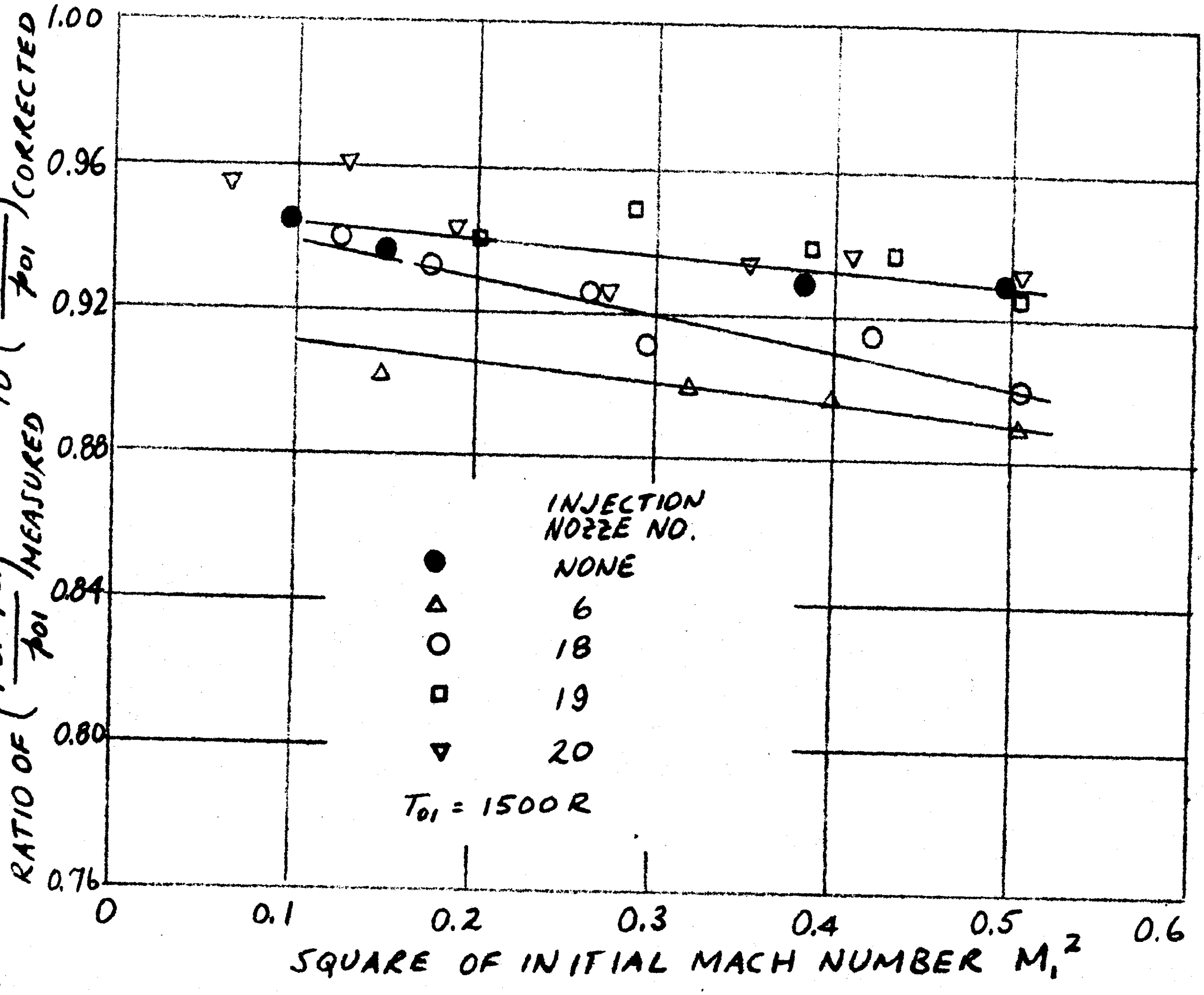

FIGURE 5

CORRECTION FACTOR FOR AEROTHERMOPRESSOR ENTRANCE NOZZLE WITH NO WATER INJECTION NOZZLE AND WITH INJECTION NOZZLES NOS. 6, 18, 19, 20 – AS A FUNCTION OF INITIAL MACH NUMBER

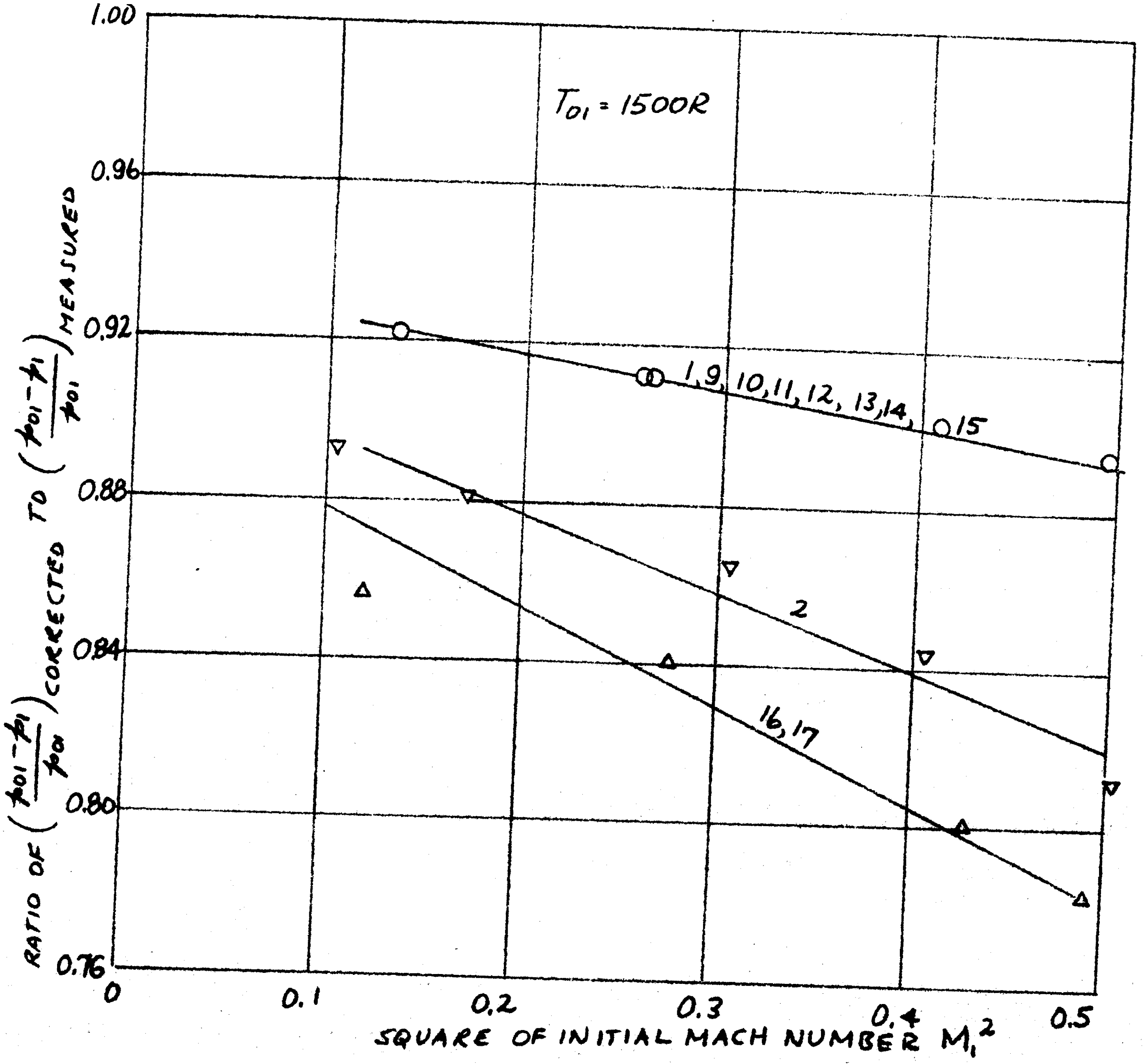

FIGURE 6

CORRECTION FACTOR FOR AEROTHERMOPRESSOR ENTRANCE NOZZLE WITH WATER INJECTION NOZZLES 1, 2, 9 TO 17 – AS A FUNCTION OF INITIAL MACH NUMBER

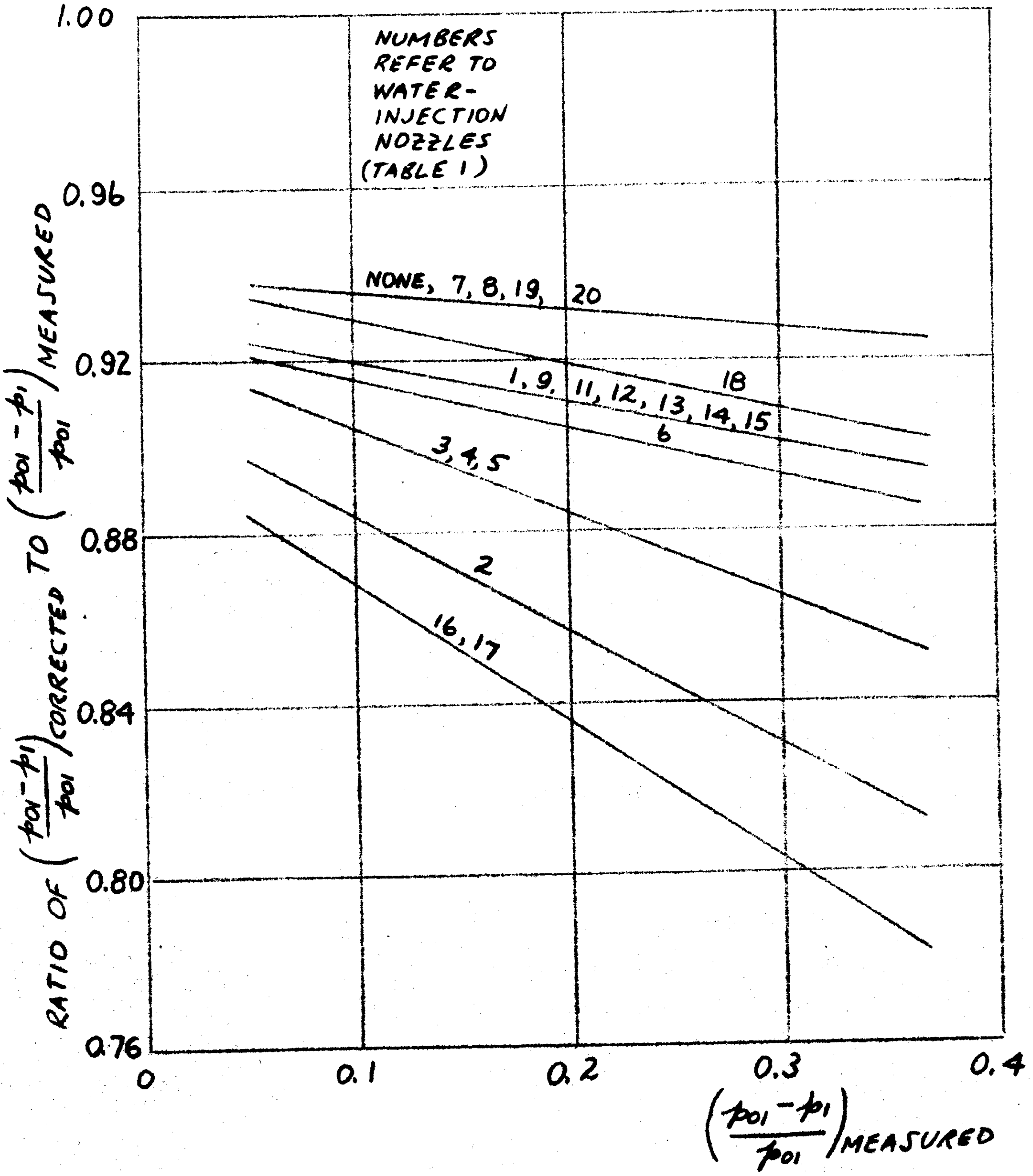

FIGURE 7

CORRECTION FACTOR FOR AEROTHERMOPRESSOR ENTRANCE NOZZLE WITH VARIOUS WATER INJECTION NOZZLES - AS A FUNCTION OF MEASURED PRESSURE DROP.

FIGURE 8

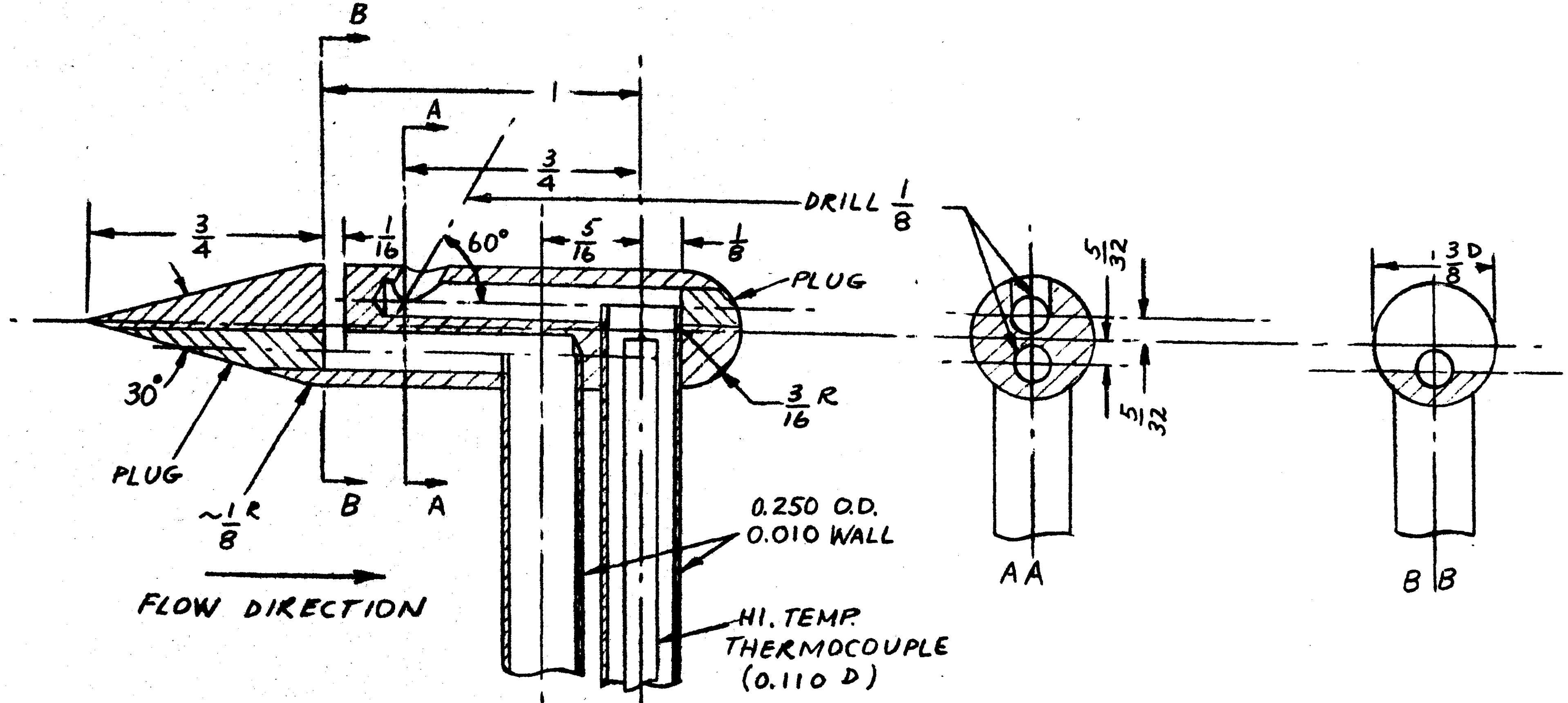

SCALE 2X
321 OR 347 STAINLESS STEEL

FIGURE 8

VAPOR SAMPLING PROBE NUMBER I

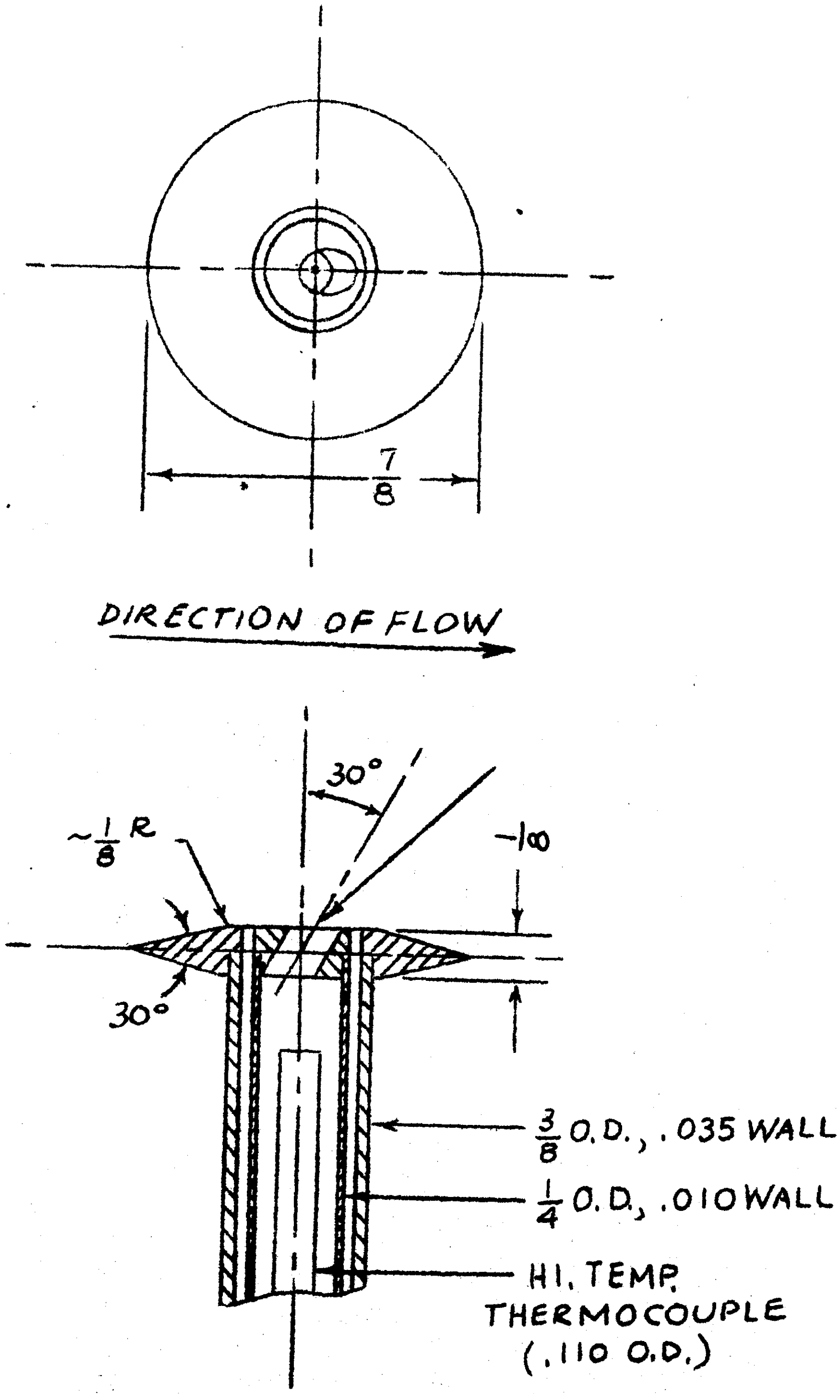

SCALE 2X
321 OR 347 S.S.

FIGURE 9

VAPOR SAMPLING PROBE NUMBER II

FIGURE 10

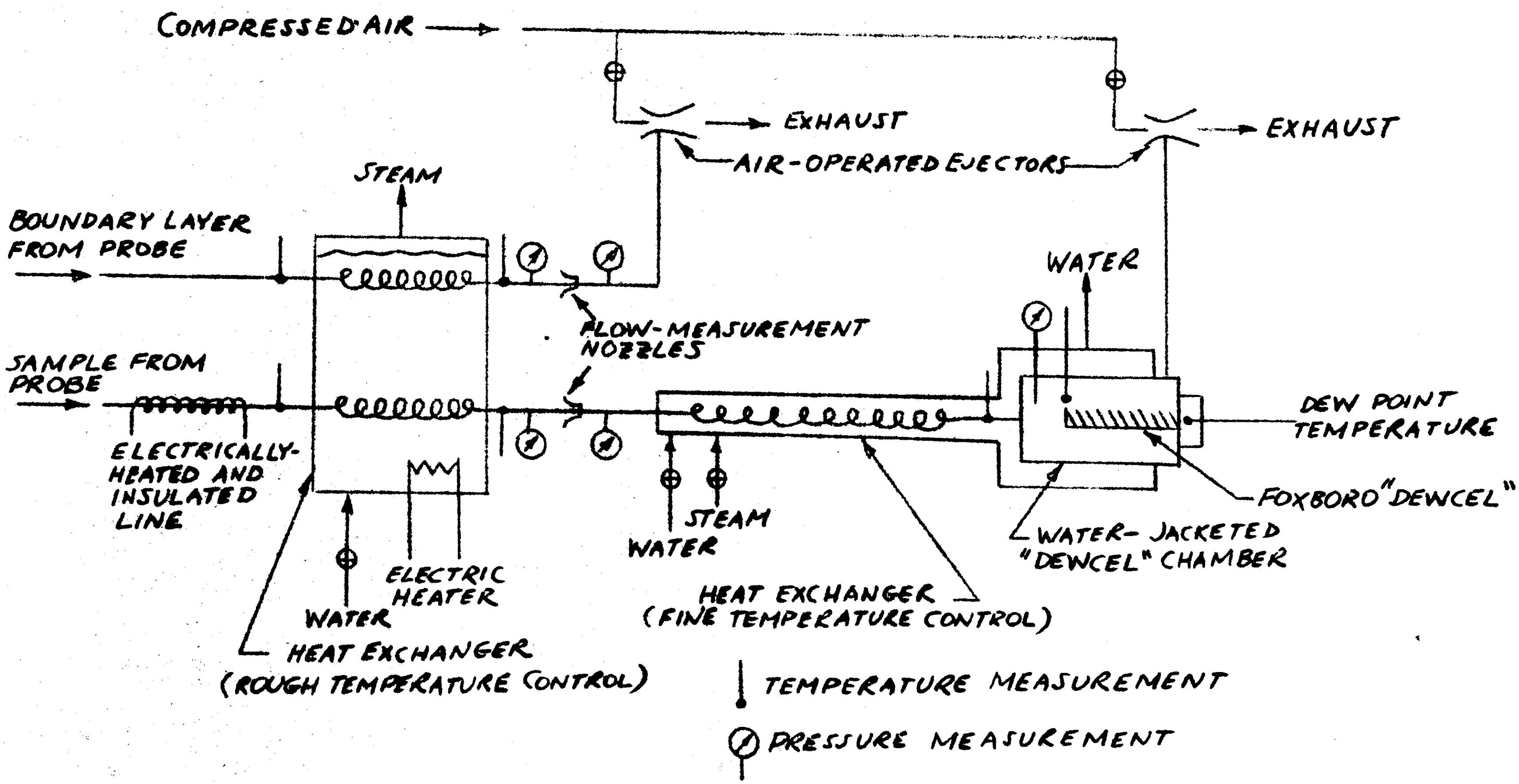

FIGURE 10

SCHEMATIC DIAGRAM OF APPARATUS FOR HUMIDITY MEASUREMENT

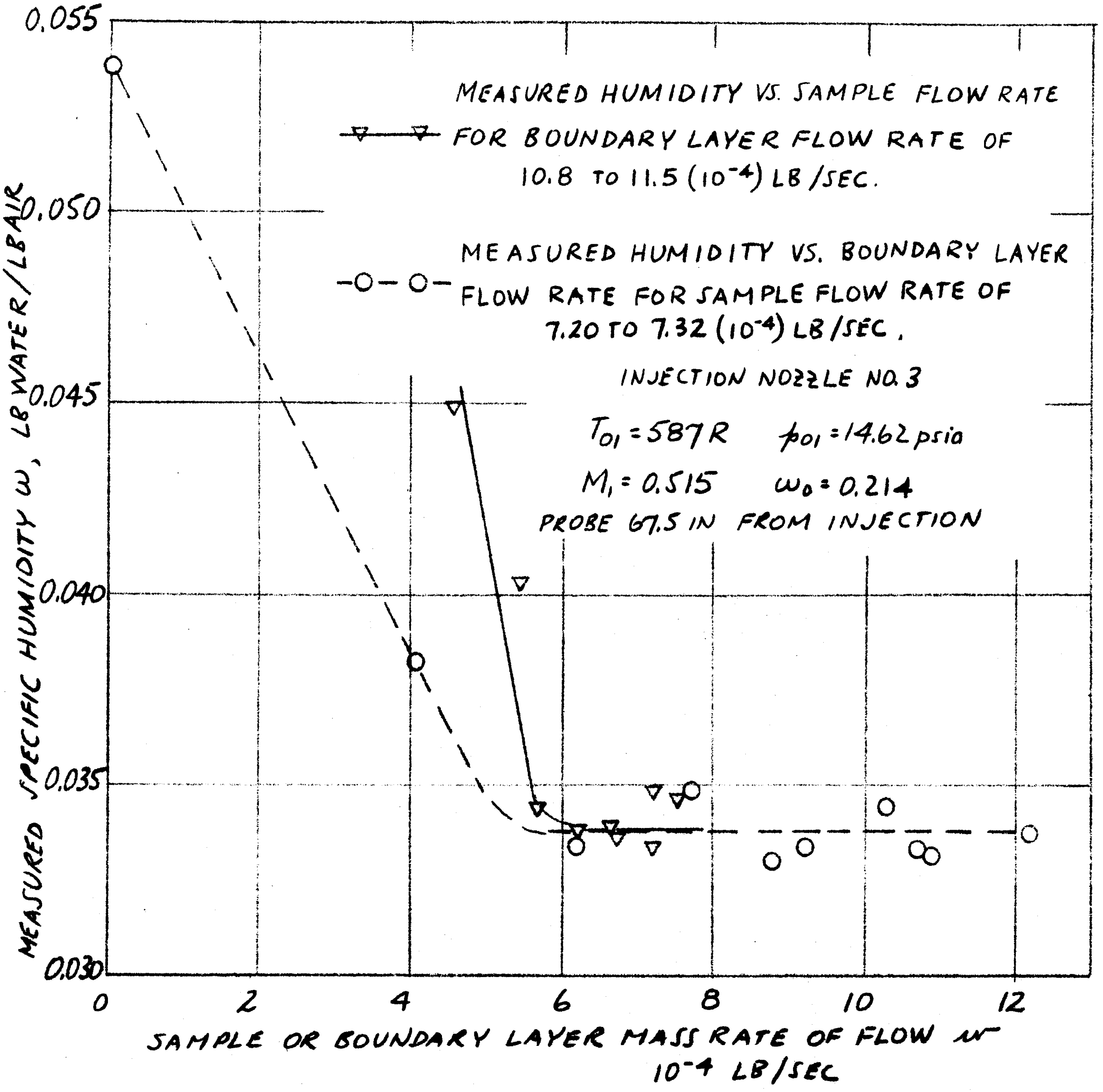

FIGURE 11

VARIATION OF MEASURED SPECIFIC HUMIDITY WITH SAMPLE AND BOUNDARY LAYER MASS RATES OF FLOW

PROBE I

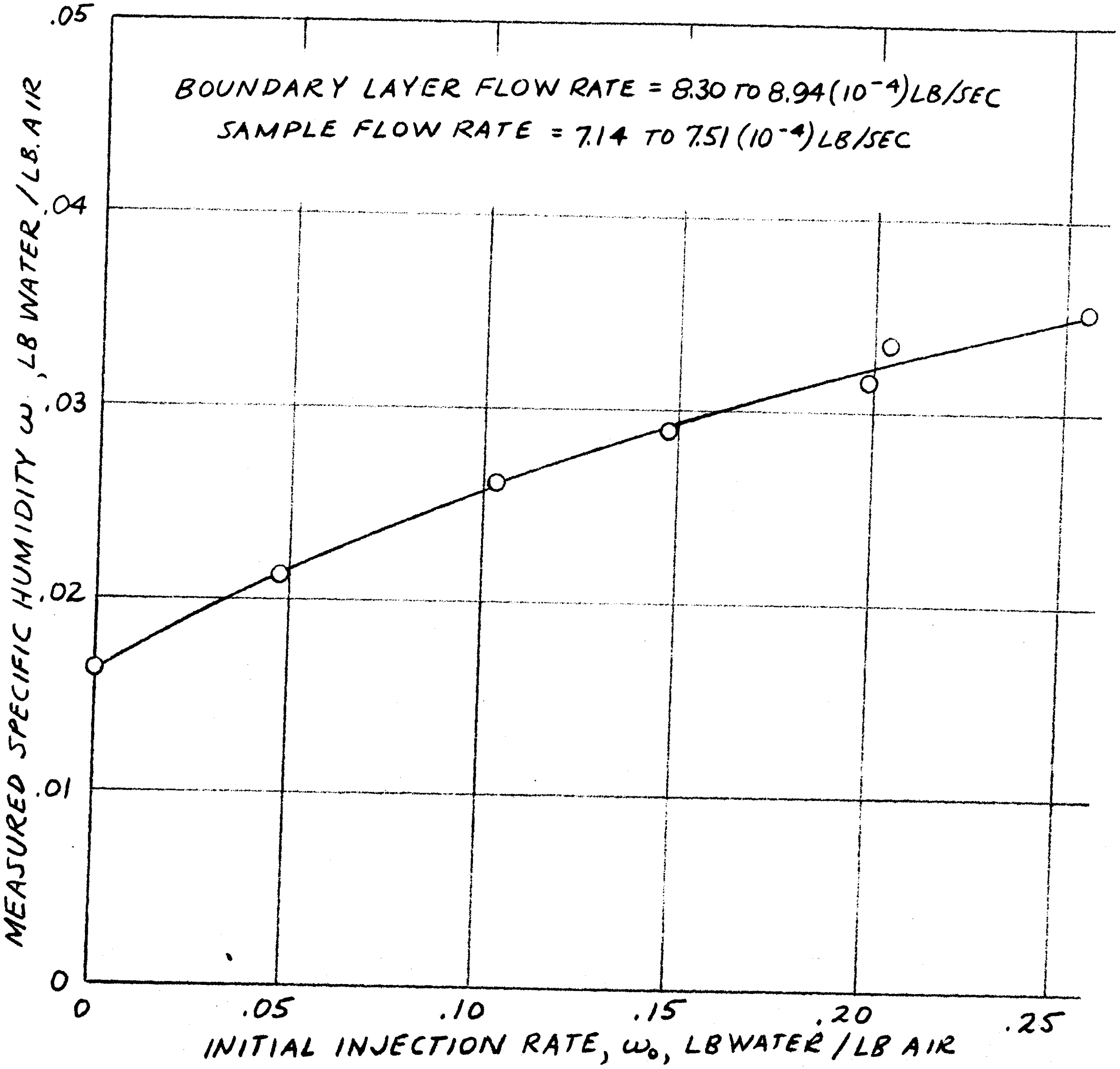

FIGURE 12

VARIATION OF MEASURED SPECIFIC HUMIDITY WITH INITIAL INJECTION RATE FOR PROBE NUMBER I.

PROBE LOCATED AT CENTER OF SECTION $67\frac{1}{2}$ IN. FROM PLANE OF INJECTION.

$T_{01} = 123F$, $p_{01} = 14.62$ psia, $M_1 = 0.515$

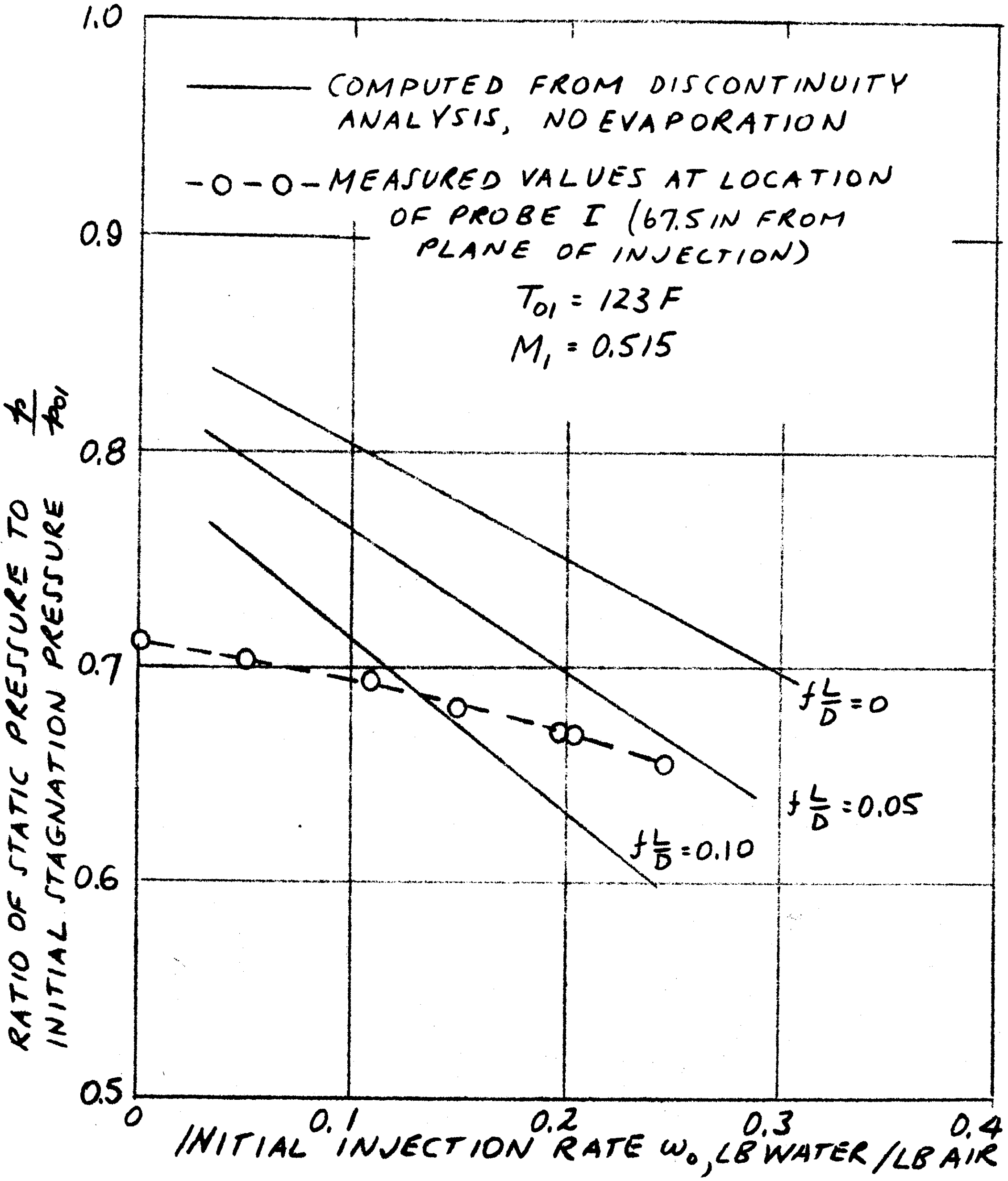

FIGURE 13

COMPARISON OF MEASURED PRESSURES WITH VALUES COMPUTED FROM DISCONTINUITY ANALYSIS.

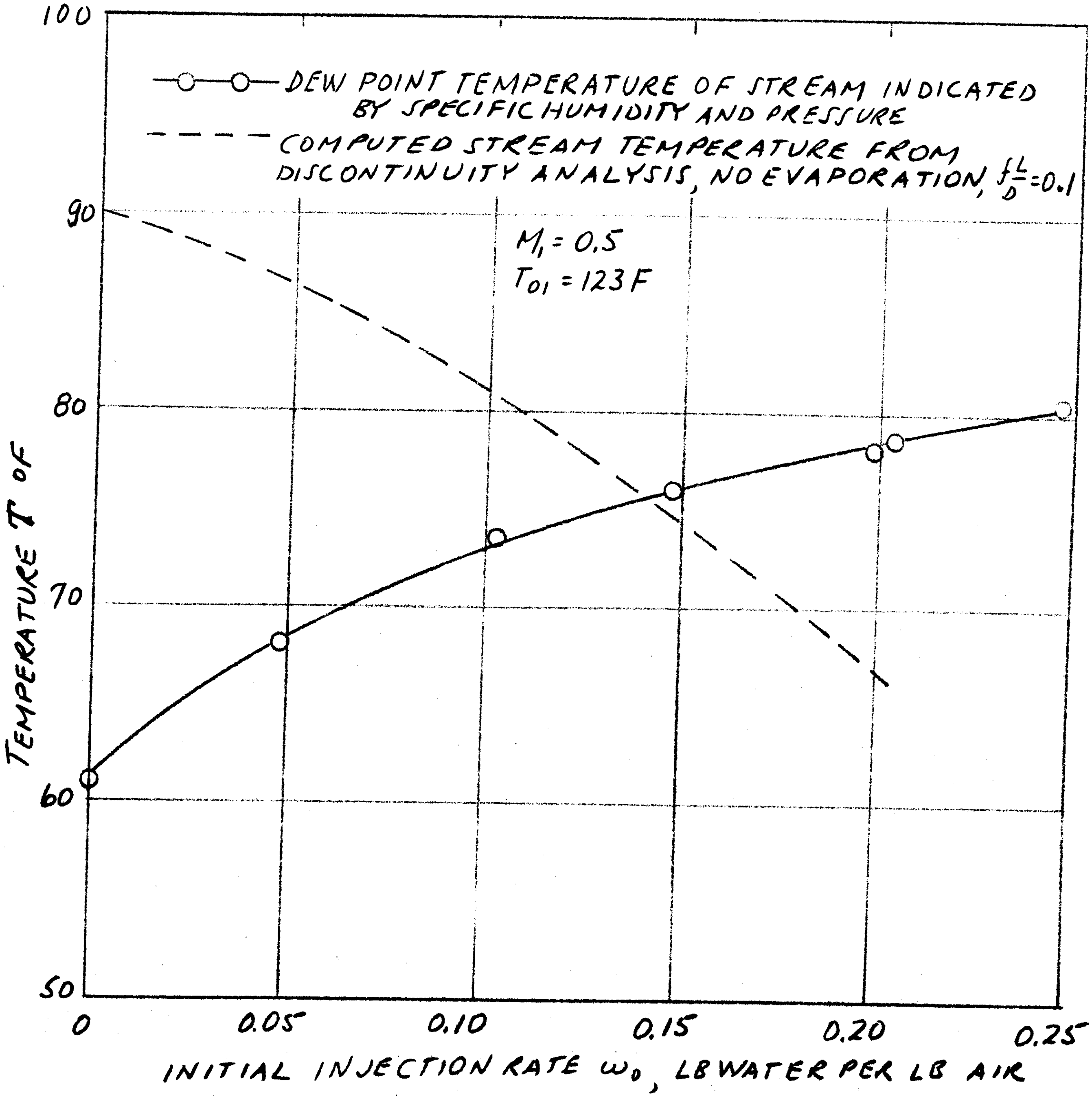

FIGURE 14

COMPARISON OF STREAM DEW POINT TEMPERATURE COMPUTED FROM MEASUREMENTS WITH PROBE I WITH STREAM TEMPERATURE COMPUTED FROM DISCONTINUITY ANALYSIS FOR NO EVAPORATION

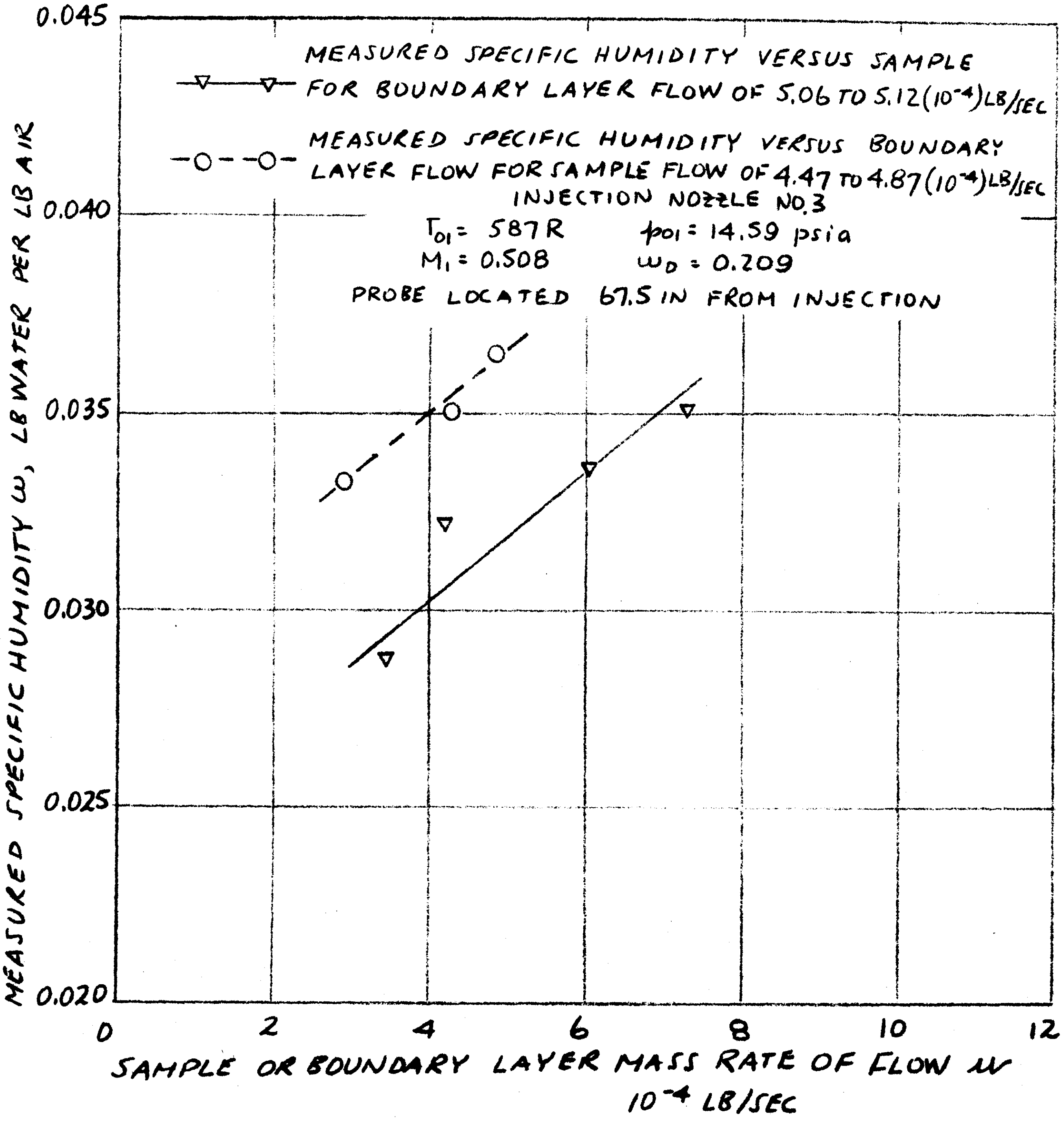

FIGURE 15

VARIATION OF MEASURED SPECIFIC HUMIDITY WITH SAMPLE AND BOUNDARY LAYER MASS RATES OF FLOW. PROBE II

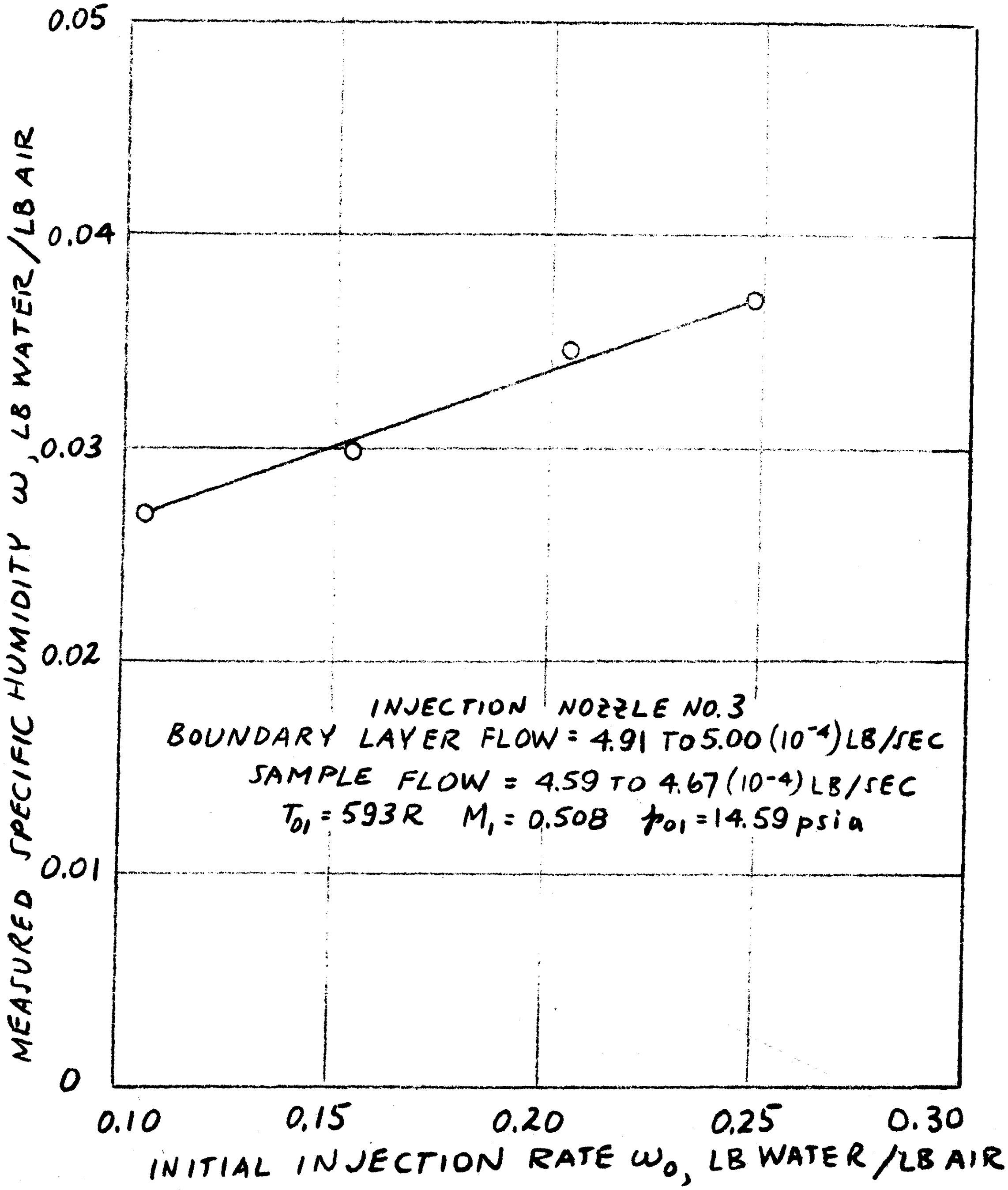

FIGURE 16

VARIATION OF MEASURED SPECIFIC HUMIDITY WITH INITIAL INJECTION RATE FOR SAMPLING PROBE II LOCATED 67.5 IN. FROM INJECTION PLANE

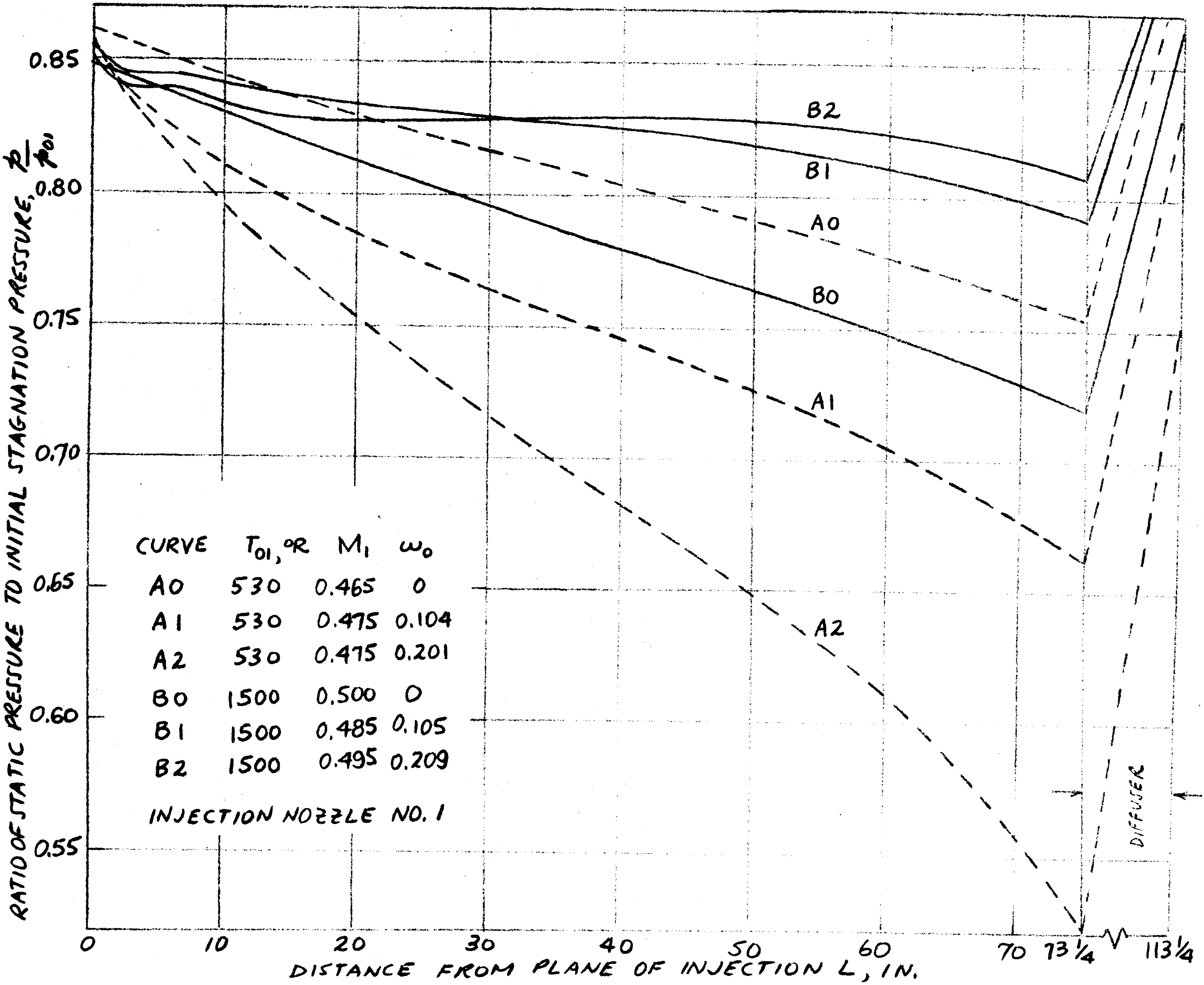

CURVE	T_{01}, °R	M_1	ω_0
A0	530	0.465	0
A1	530	0.475	0.104
A2	530	0.475	0.201
B0	1500	0.500	0
B1	1500	0.485	0.105
B2	1500	0.495	0.209

INJECTION NOZZLE NO. 1

FIGURE 17

EFFECT OF WATER INJECTION ON PRESSURE DISTRIBUTION ALONG EVAPORATION SECTION AT LOW AND HIGH TEMPERATURES

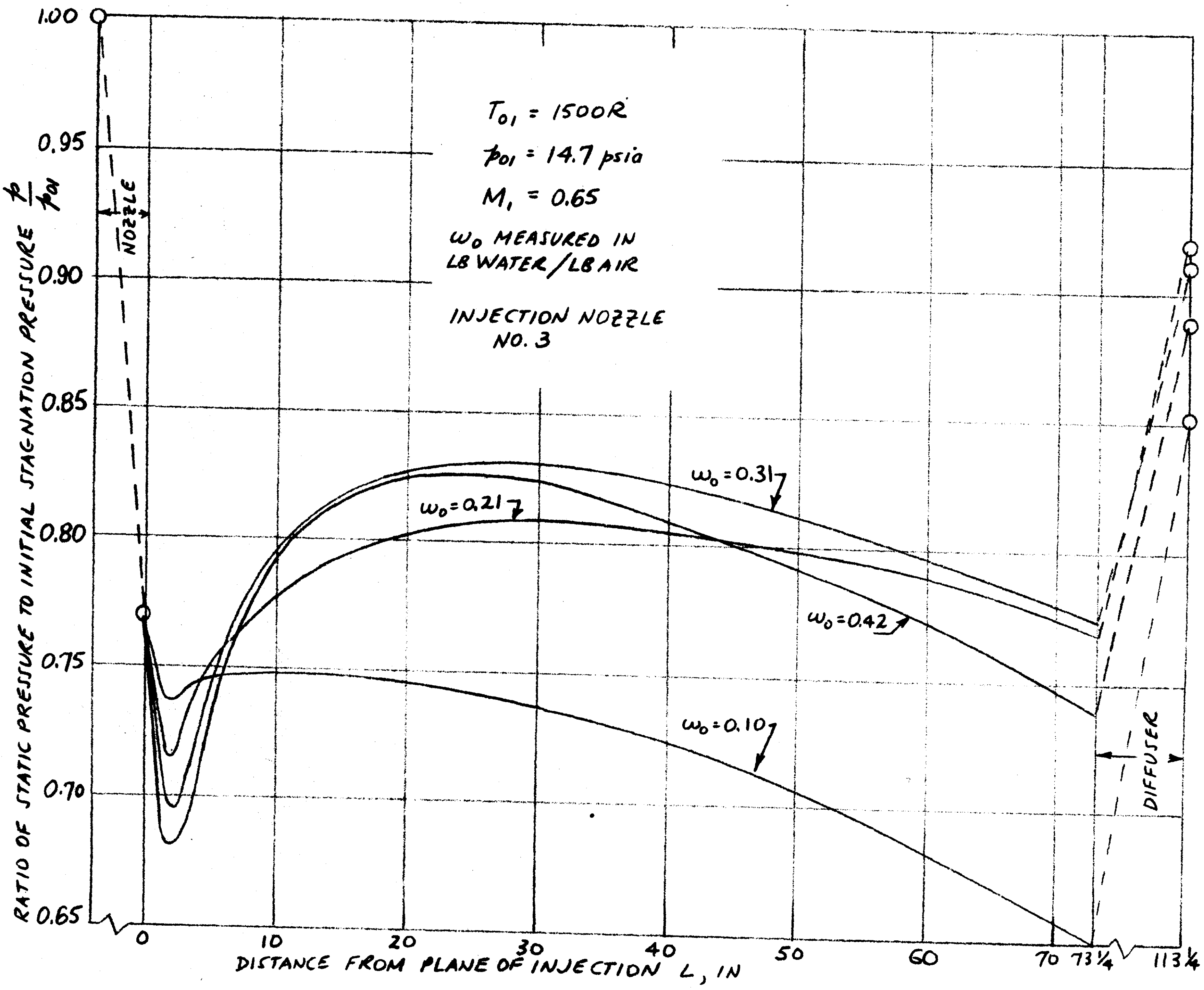

FIGURE 18

EFFECT OF WATER EVAPORATION ON STATIC PRESSURE DISTRIBUTION ALONG EVAPORATION SECTION FOR VARIOUS INJECTION RATES

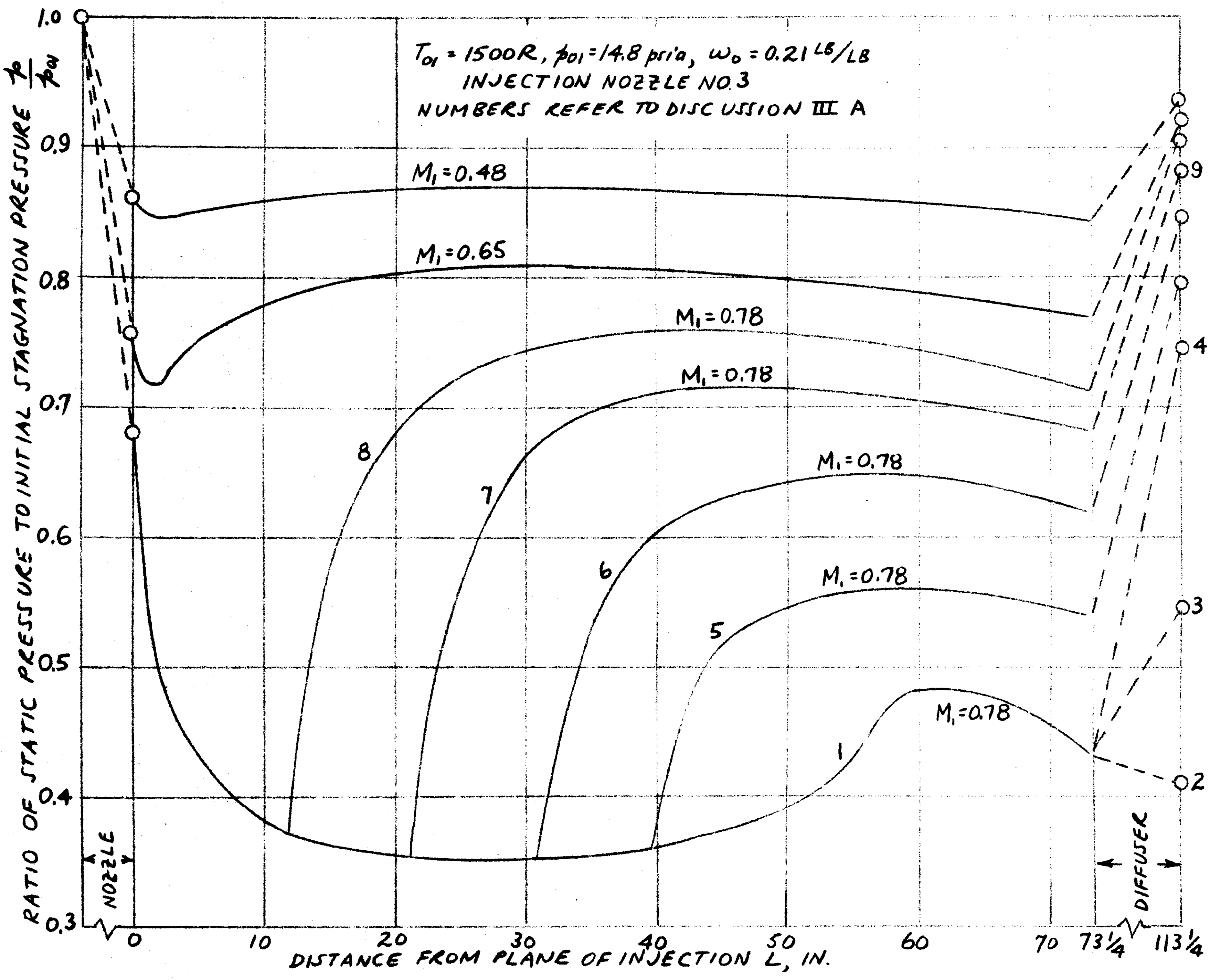

FIGURE 19

EFFECT OF WATER EVAPORATION ON STATIC PRESSURE DISTRIBUTION ALONG EVAPORATION SECTION FOR VARIOUS INITIAL MACH NUMBER VALUES

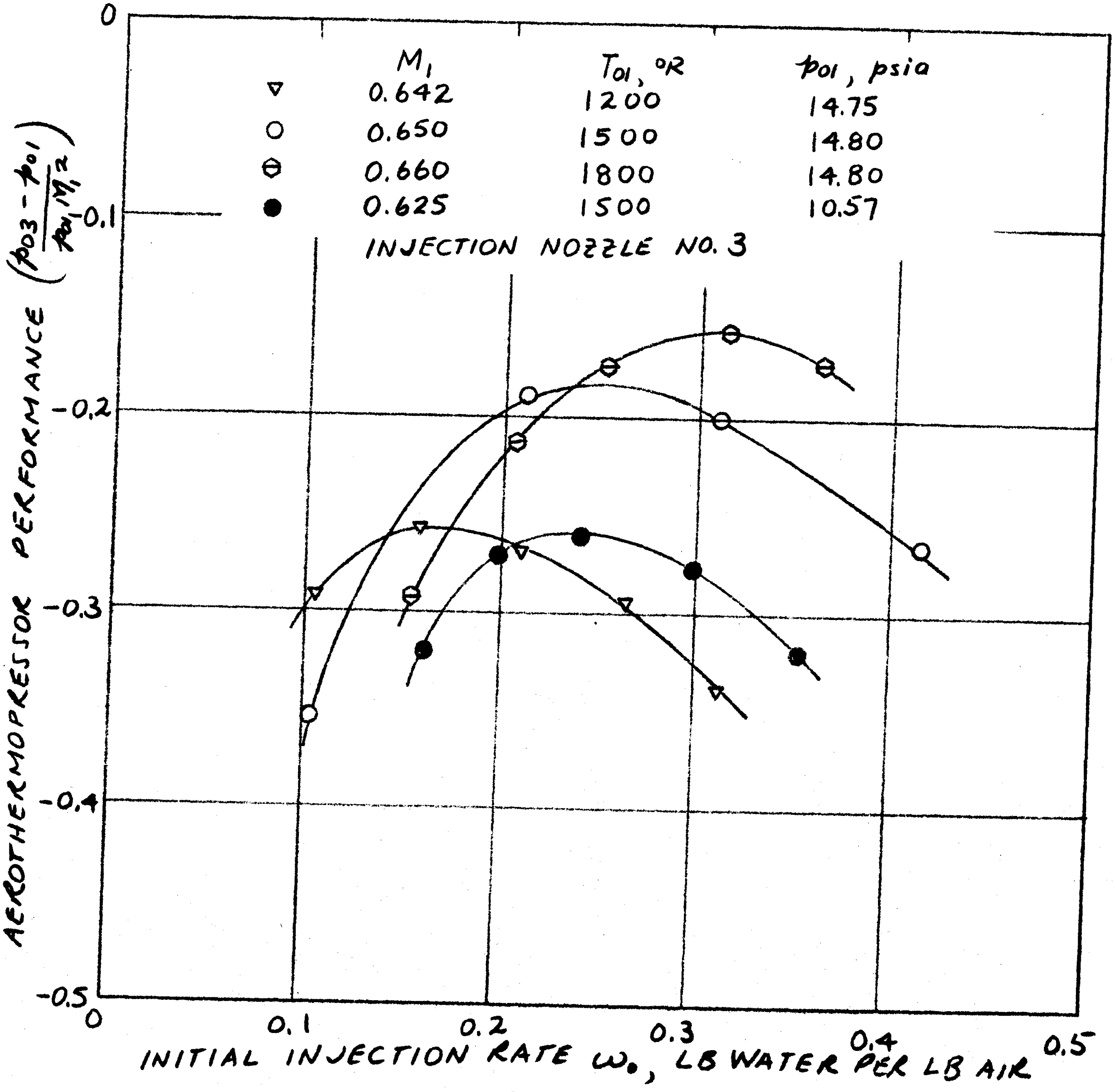

FIGURE 20

TYPICAL AEROTHERMOPRESSOR PERFORMANCE CURVES - PERFORMANCE COEFFICIENT VS. INITIAL INJECTION RATE

FIGURE 21

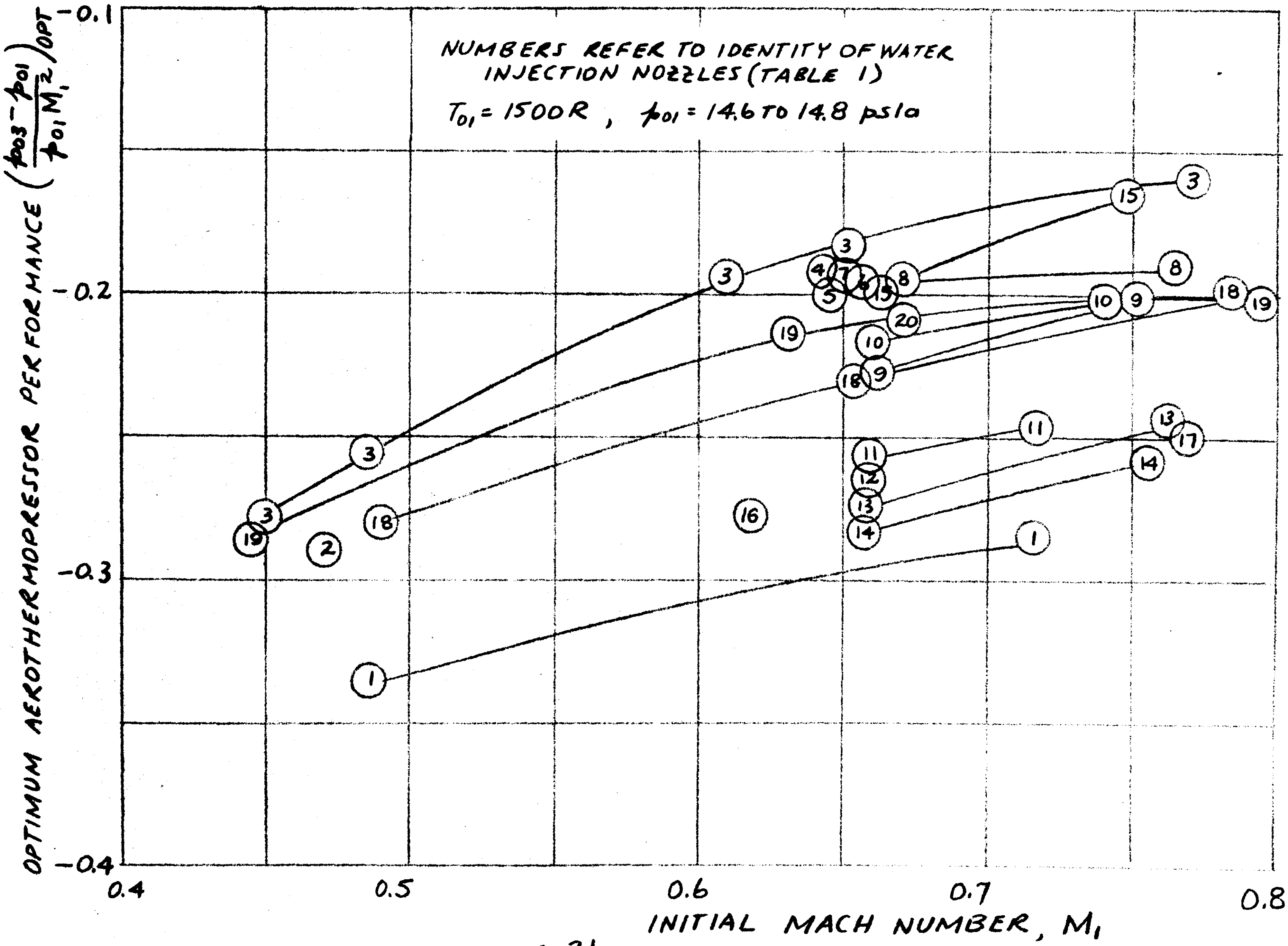

FIGURE 21
OPTIMUM AEROTHERMOPRESSOR PERFORMANCE ACHIEVED WITH VARIOUS WATER INJECTION NOZZLES

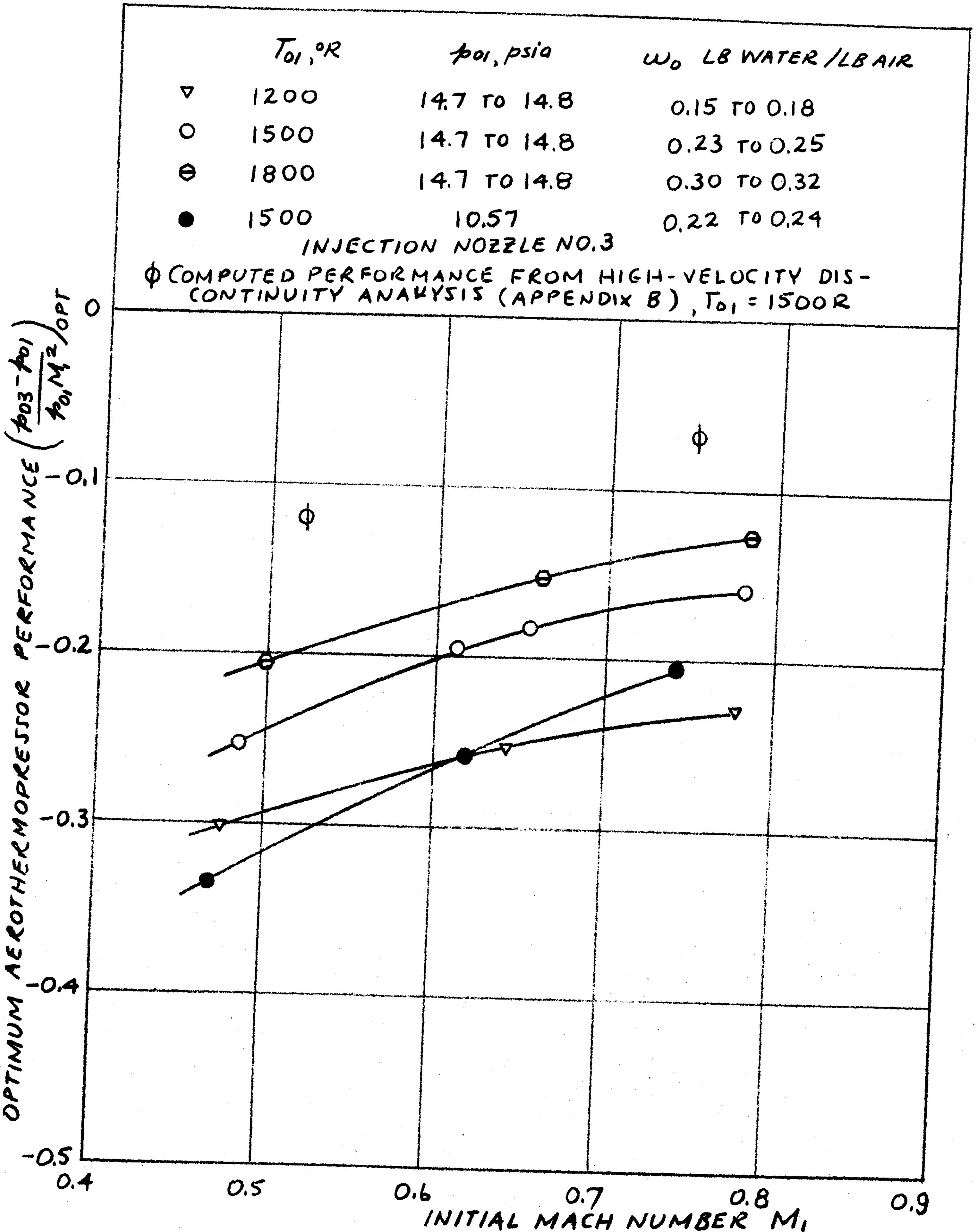

FIGURE 22
MEASURED OPTIMUM AEROTHERMOPRESSOR PERFORMANCE
VERSUS INITIAL MACH NUMBER

FIGURE 23

EFFECT OF PRESSURE LEVEL ON STATIC PRESSURE DISTRIBUTION ALONG EVAPORATION SECTION.

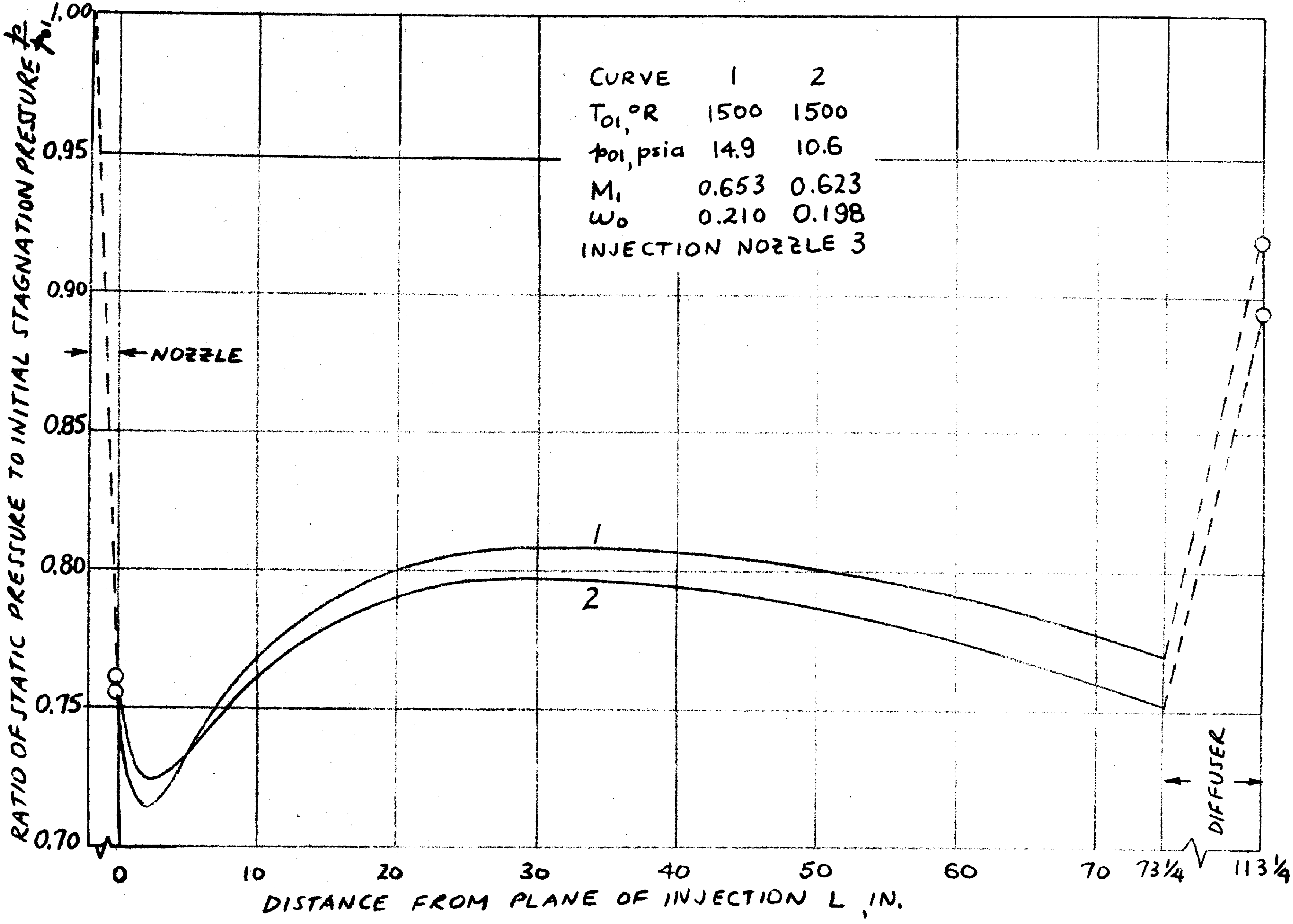

INJECTION NOZZLE 3

$\omega_0 = 0.150$ LB/LB.

$M_1 = 0.502$

$T_{01} = 1500R$

$p_{01} = 14.6$ psia

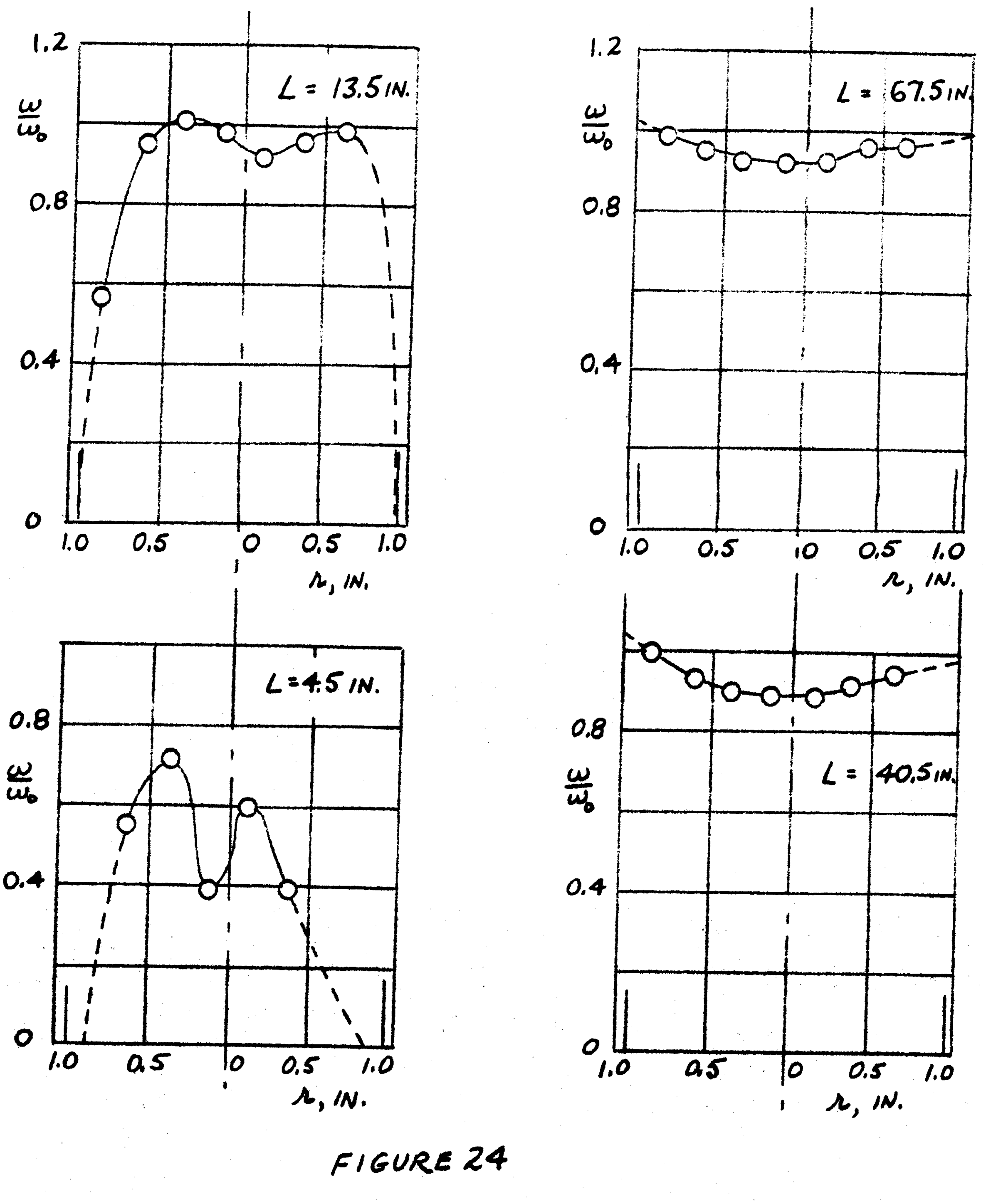

FIGURE 24

CORRECTED FRACTION EVAPORATED PROFILES AT FOUR CROSS-SECTIONS - INITIAL INJECTION RATE OF 0.150 LB. WATER PER LB. AIR

INJECTION NOZZLE 3

$\omega_0 = 0.252$ LB/LB

$M_1 = 0.500$

$T_{01} = 1500$ R

$p_{01} = 14.6$ psia

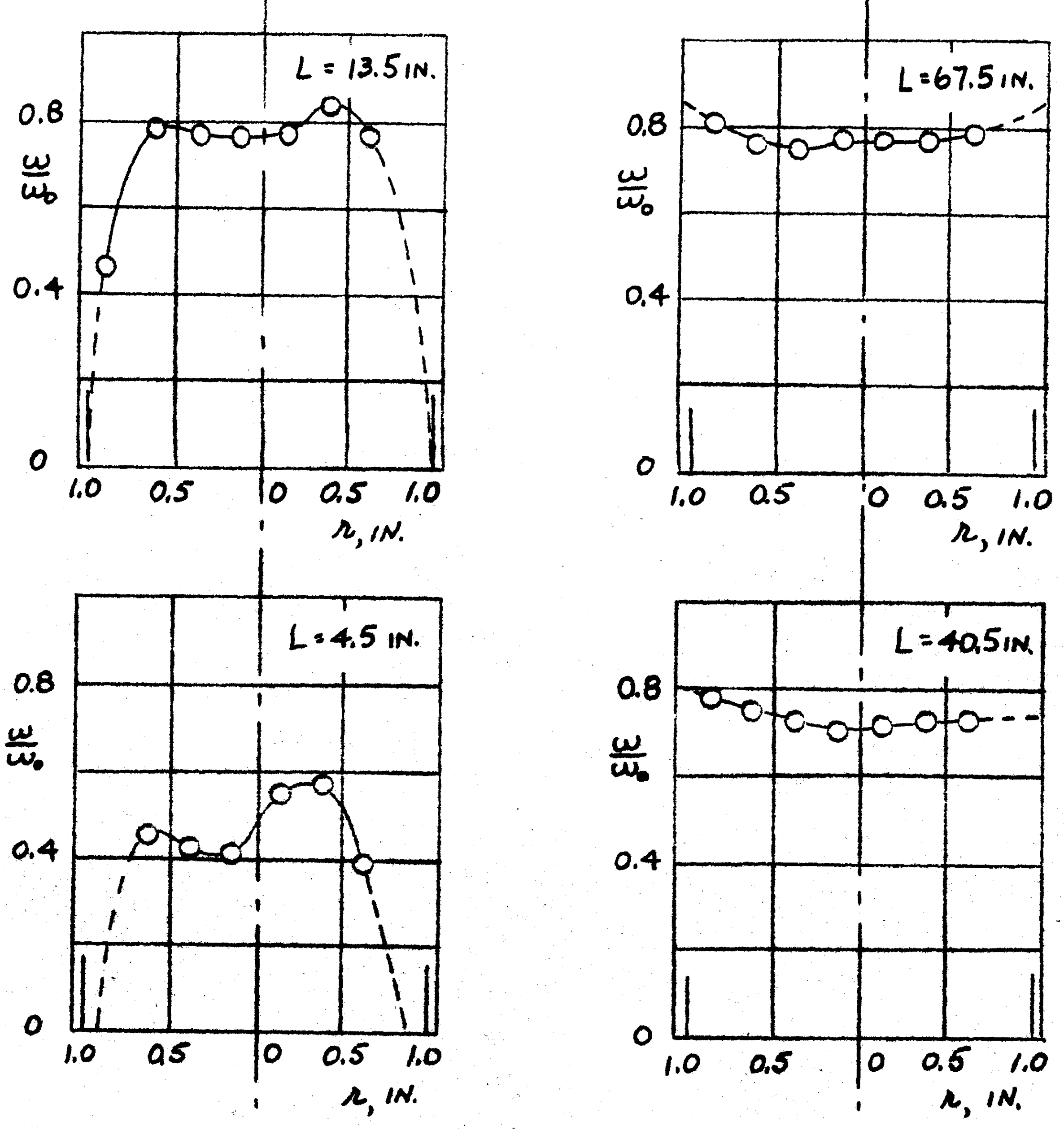

FIGURE 25

CORRECTED FRACTION EVAPORATED PROFILES AT FOUR CROSS-SECTIONS – INITIAL INJECTION RATE = 0.252 LB. WATER PER LB. AIR

FIGURE 26

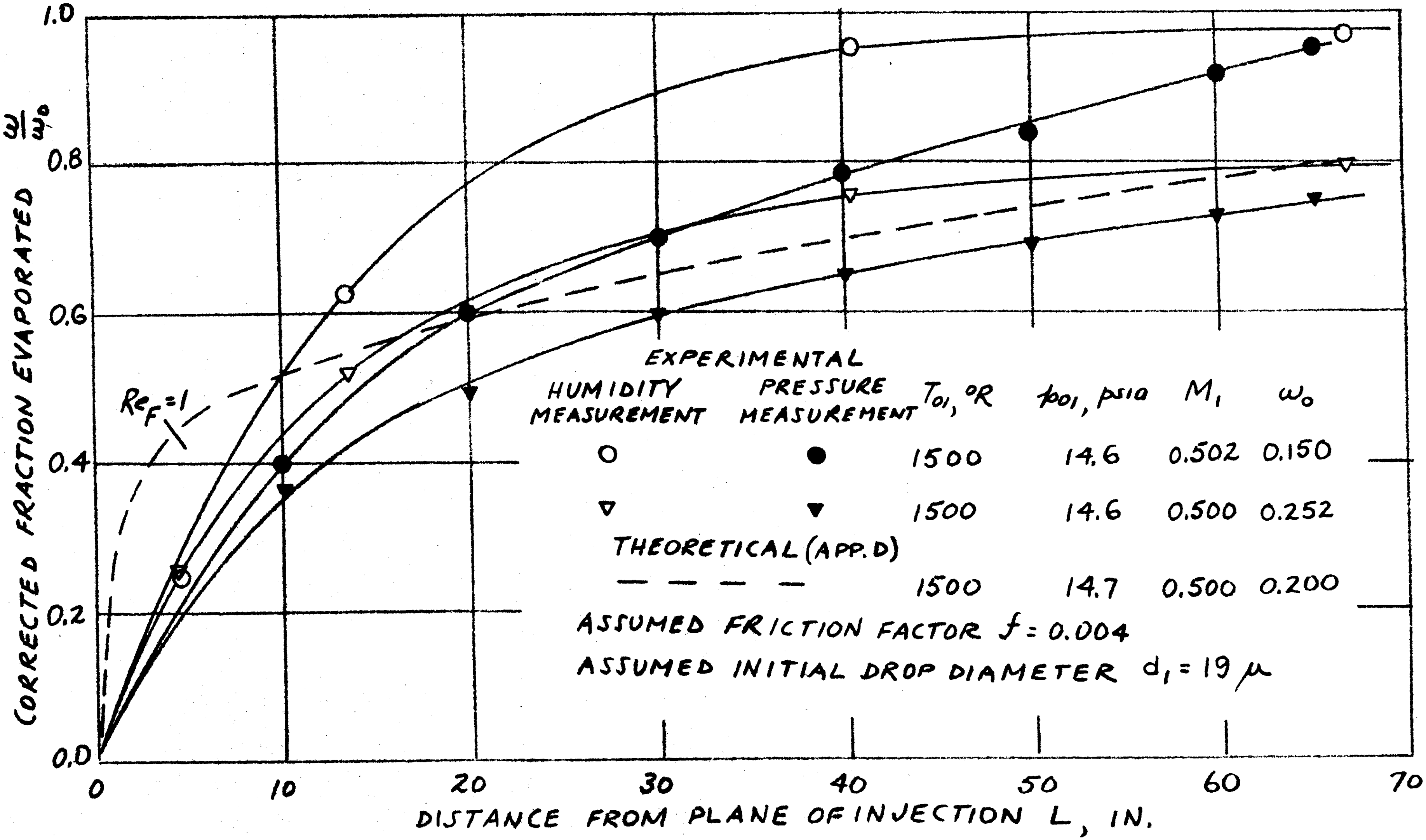

FIGURE 26

COMPARISON OF RATES OF EVAPORATION MEASURED BY HUMIDITY DATA, MEASURED BY STATIC PRESSURE DATA, AND COMPUTED BY ANALYSIS OF APPENDIX D.

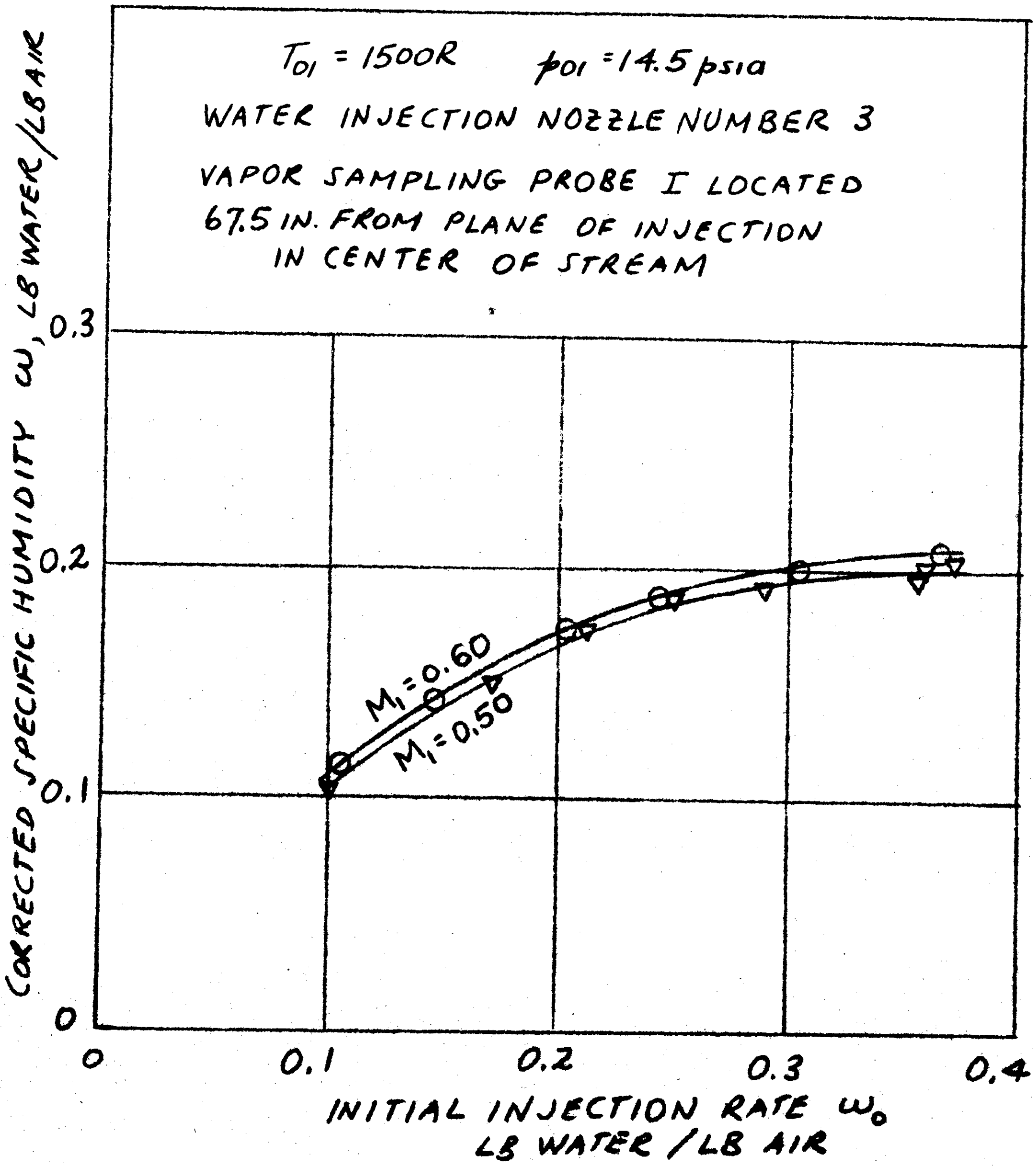

FIGURE 27

VARIATION OF RATE OF EVAPORATION WITH INITIAL MACH NUMBER AND INITIAL INJECTION RATE

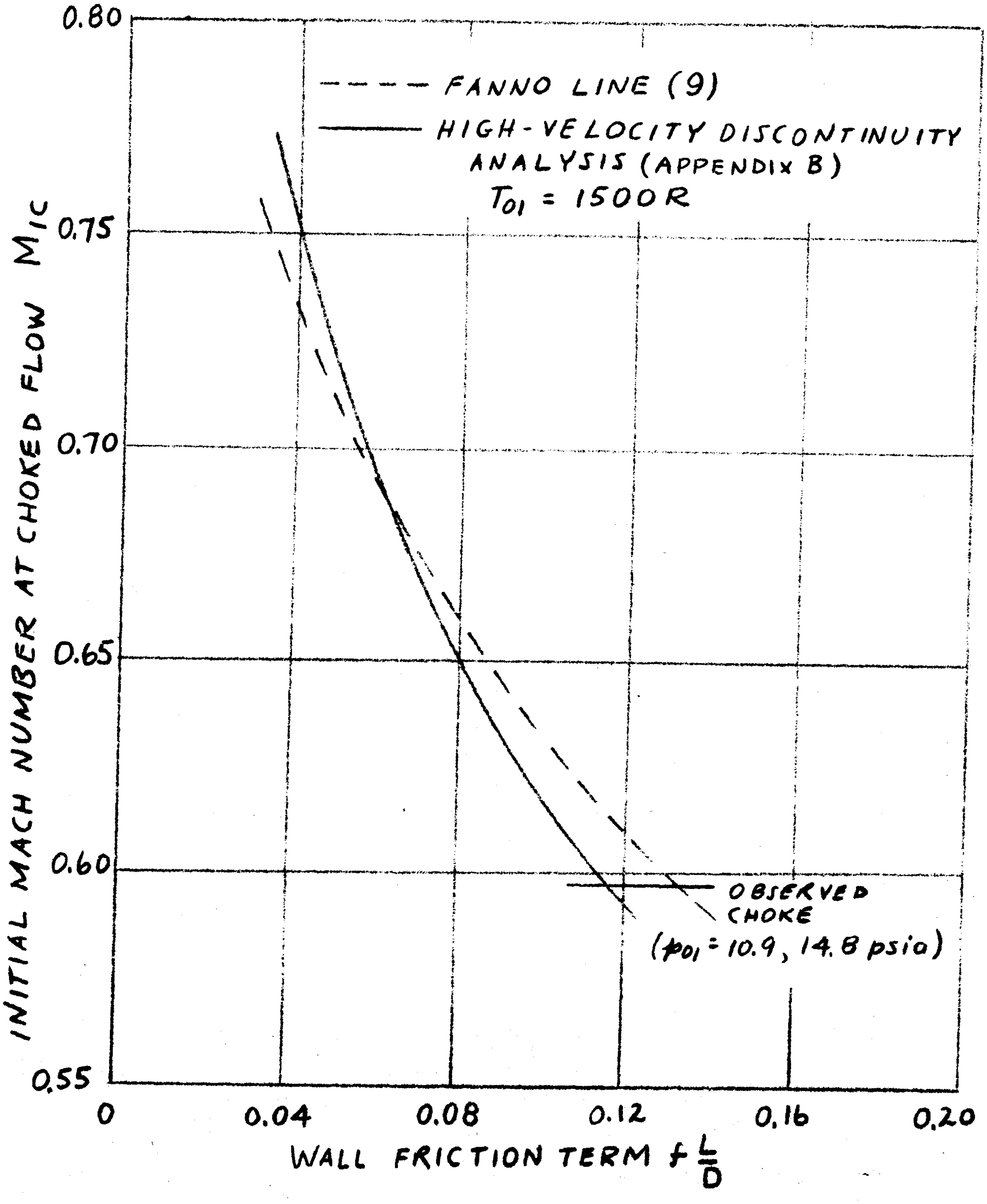

FIGURE 28

COMPARISON OF RESULTS OF FANNO LINE ANALYSIS AND HIGH-VELOCITY DISCONTINUITY ANALYSIS FOR CHOKED FLOW WITH NO WATER INJECTION,— INITIAL MACH NUMBER VERSUS WALL FRICTION.

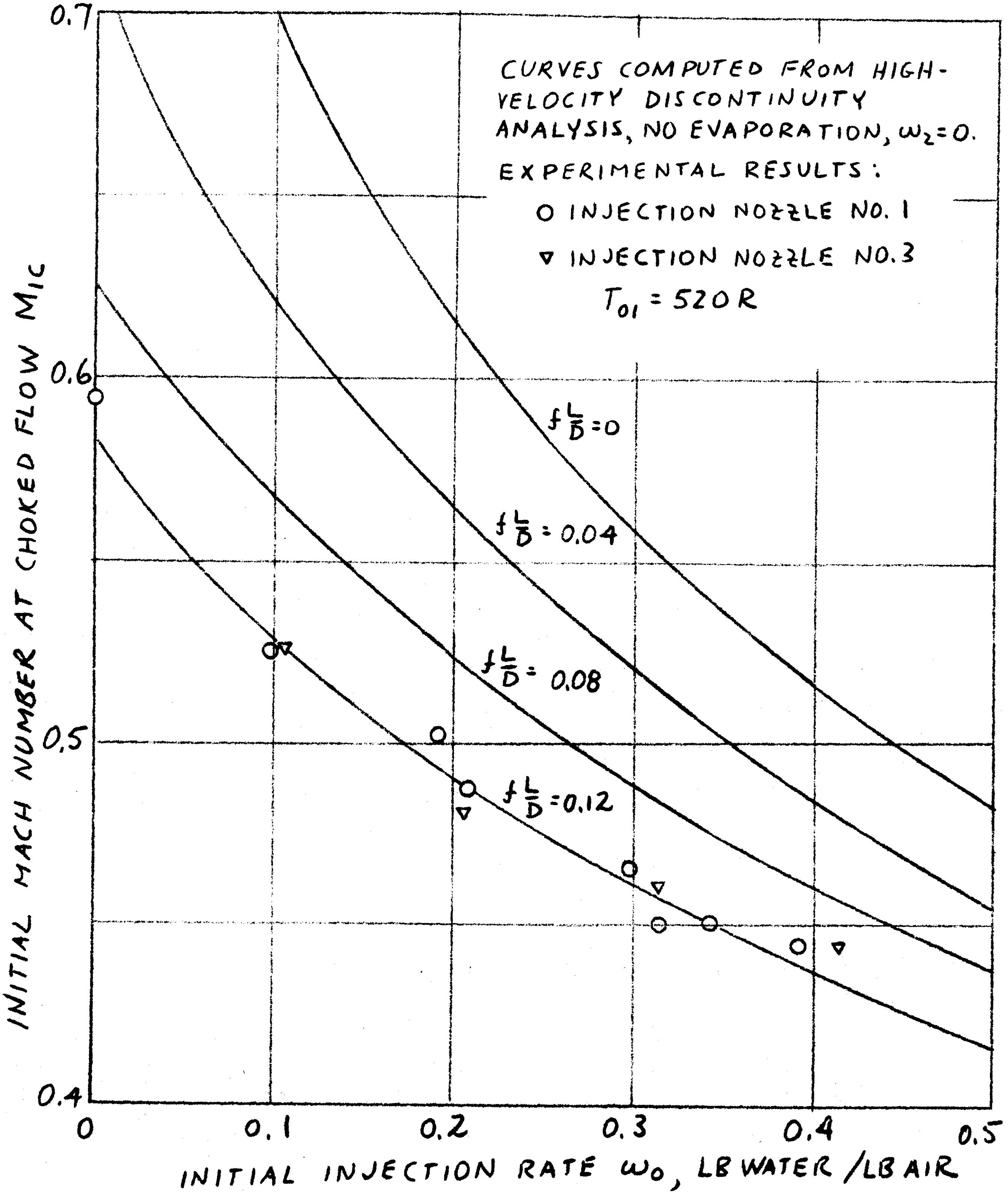

FIGURE 29

COMPARISON OF EXPERIMENTAL RESULTS WITH CALCULATIONS FROM HIGH-VELOCITY DISCONTINUITY ANALYSIS, NO EVAPORATION, CHOKED FLOW. INITIAL MACH NUMBER VERSUS INJECTION RATE.

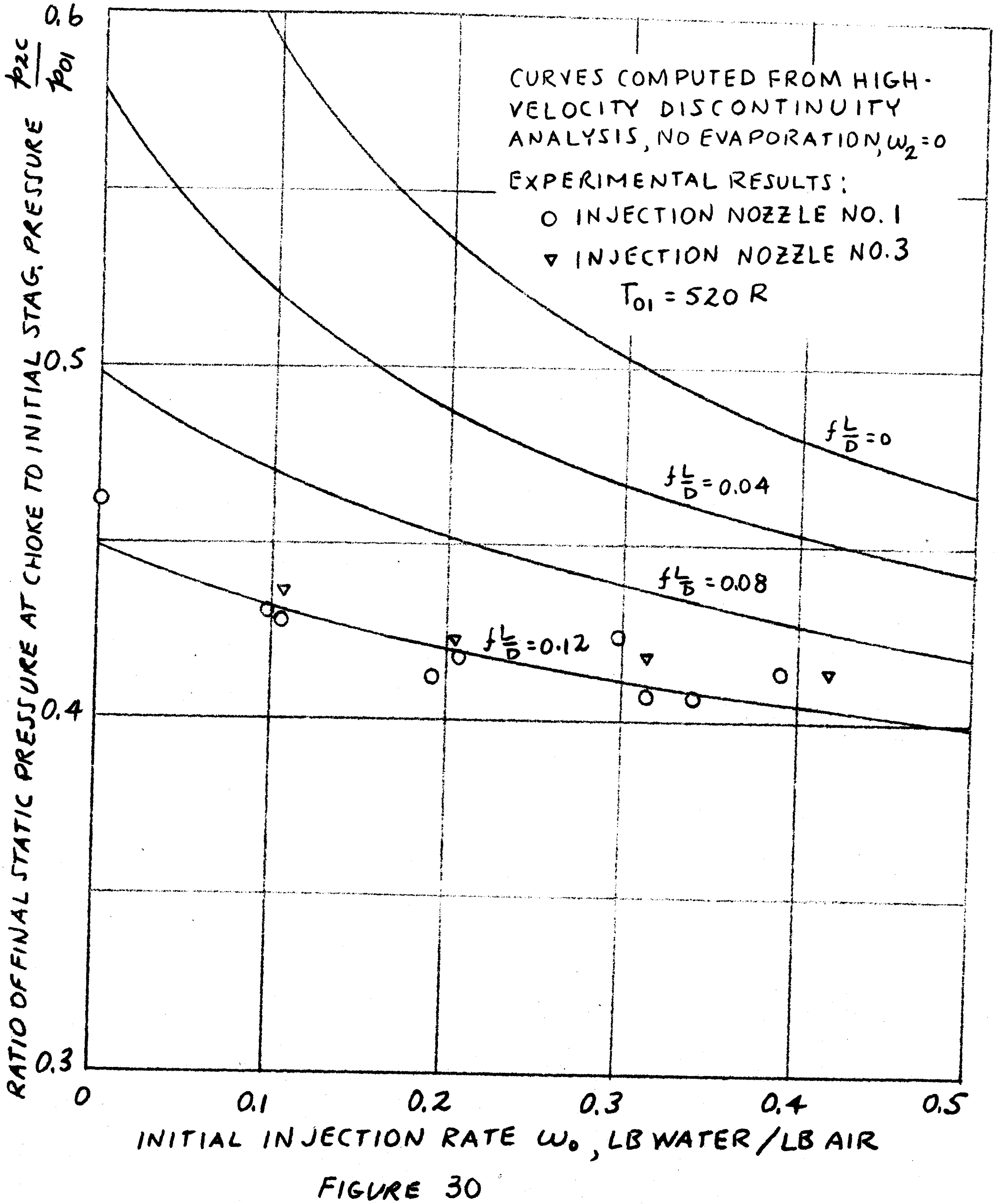

FIGURE 30

COMPARISON OF EXPERIMENTAL RESULTS WITH CALCULATIONS FROM HIGH-VELOCITY DISCONTINUITY ANALYSIS, NO EVAPORATION, CHOKED FLOW. RATIO OF FINAL STATIC PRESSURE TO INITIAL STAGNATION PRESSURE VERSUS INJECTION RATE.

FIGURE 31

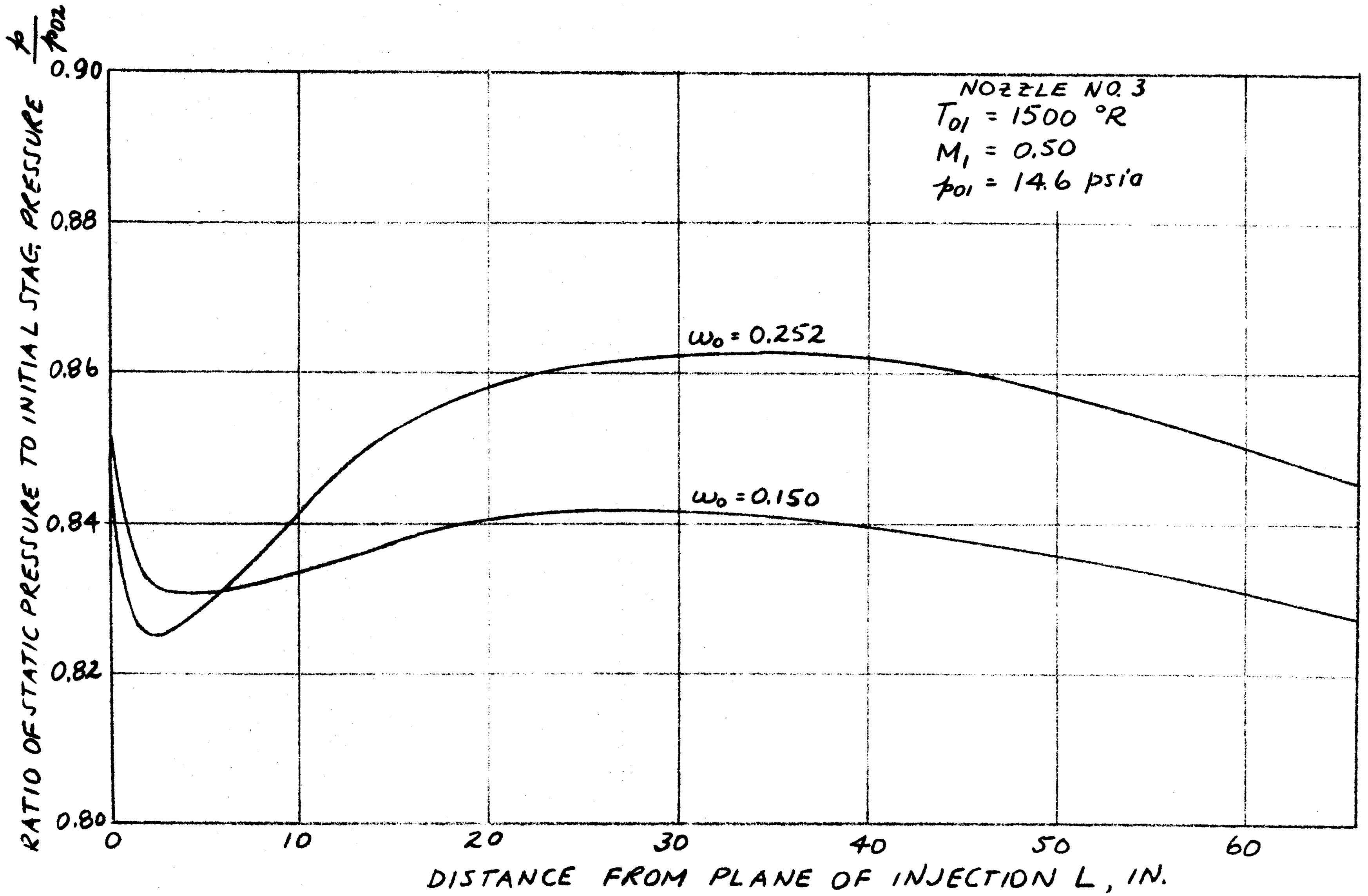

FIGURE 31

PRESSURE VARIATION ALONG EVAPORATION SECTION FOR TESTS IN WHICH HUMIDITY WAS MEASURED WITH PROBE I.

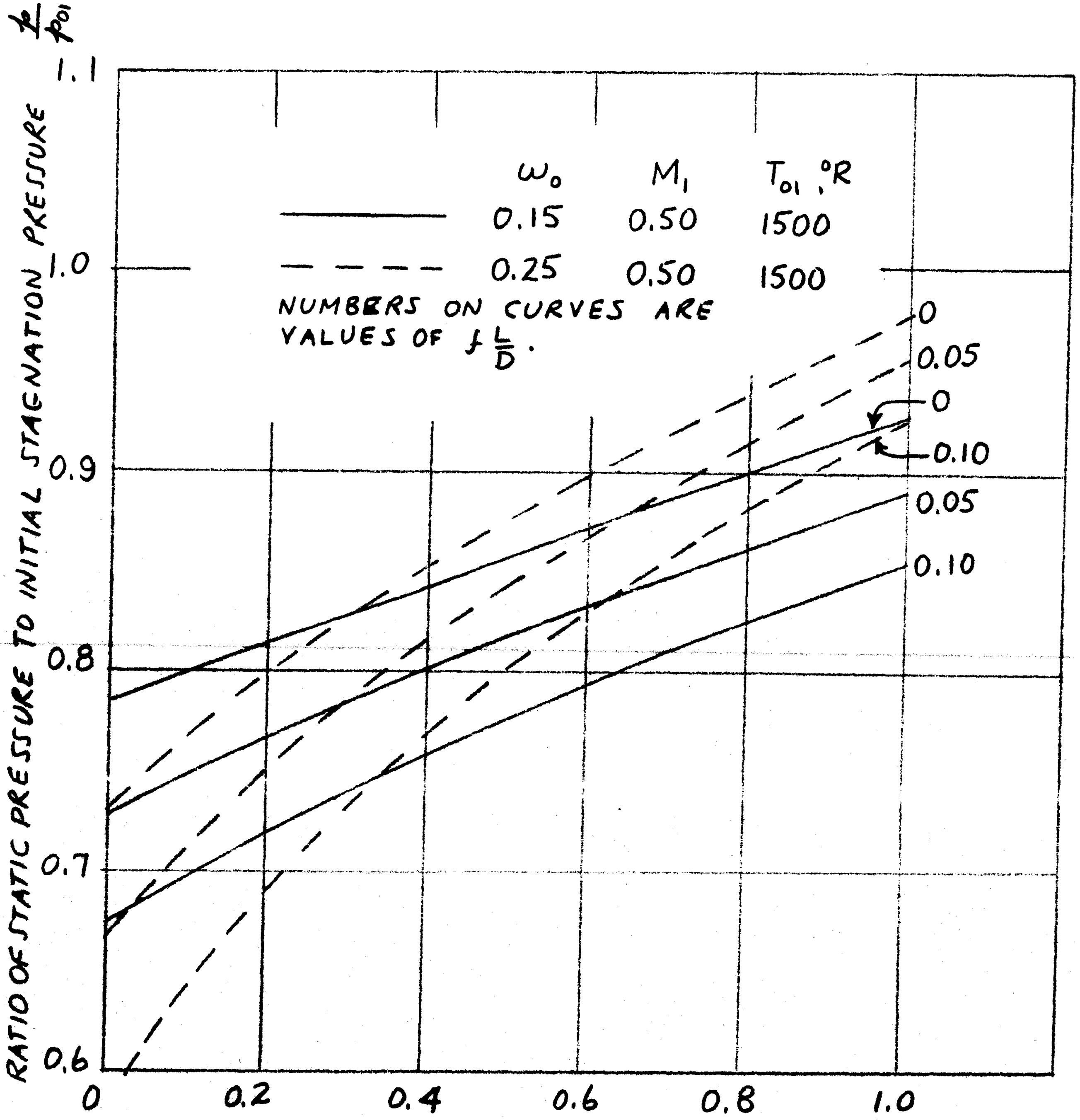

FIGURE 32

RESULTS OF COMPUTATIONS BASED ON HIGH-VELOCITY DISCONTINUITY ANALYSIS (APPENDIX B), GAVRIL (2). RATIO OF STATIC PRESSURE TO INITIAL STAGNATION PRESSURE VERSUS FRACTION EVAPORATED.

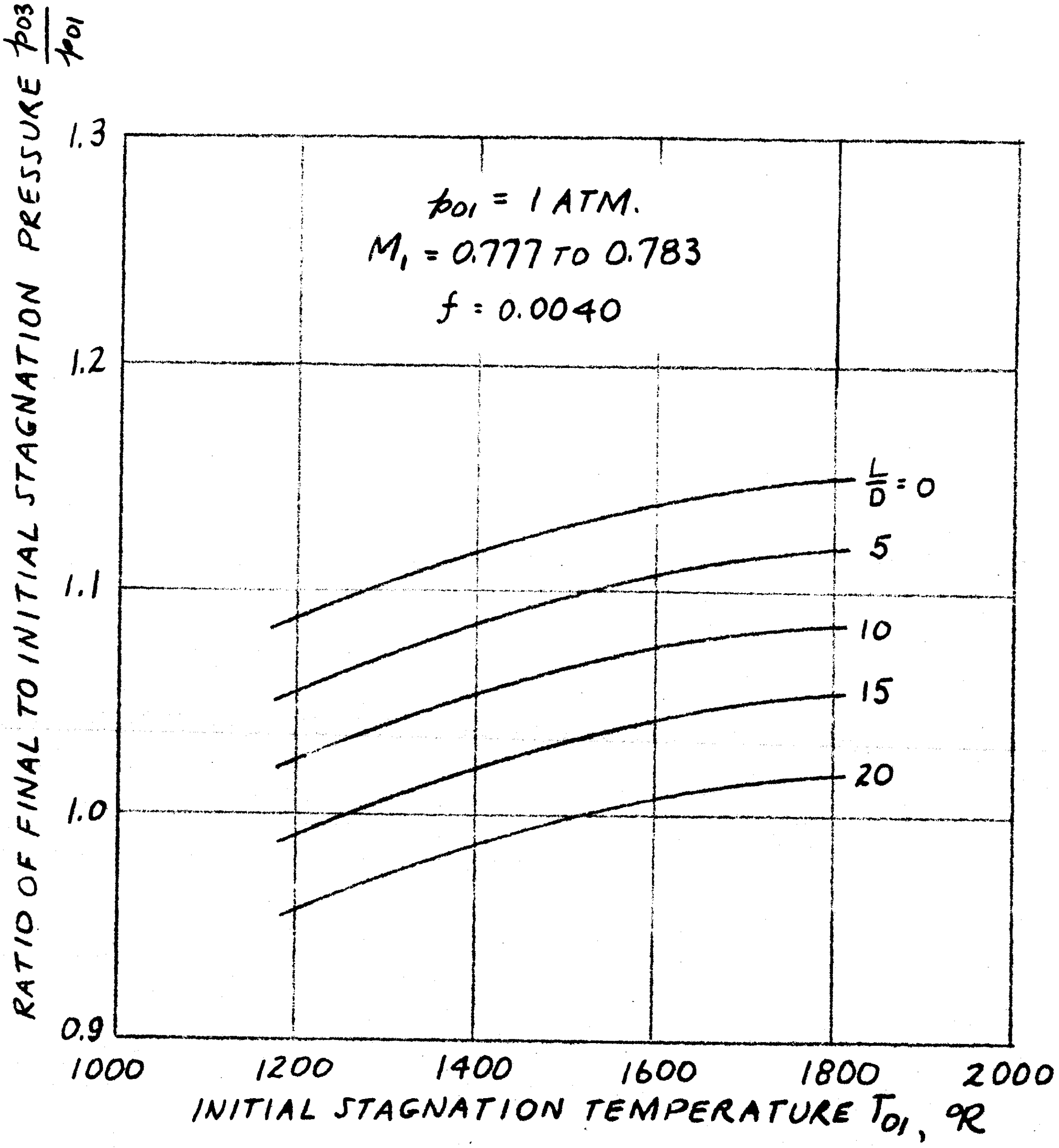

FIGURE 33

RESULTS OF EXTRAPOLATION OF SMALL SCALE TEST DATA TO LARGER SCALE AEROTHERMOPRESSORS.

STAGNATION PRESSURE RATIO VERSUS INITIAL STAGNATION TEMPERATURE FOR VARIOUS LENGTH - DIAMETER RATIOS.

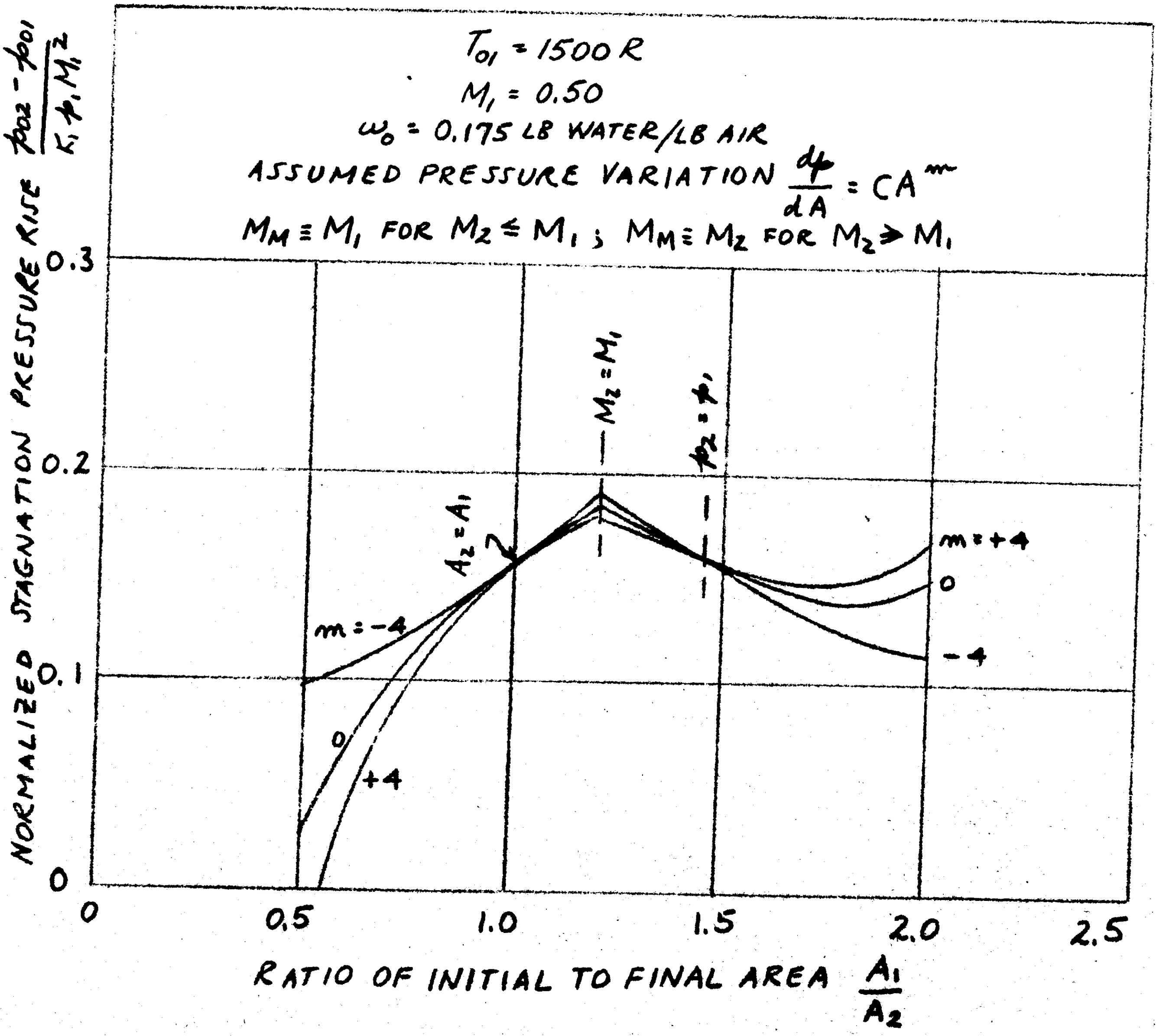

FIGURE 34

VARIATION IN STAGNATION PRESSURE RISE WITH AREA AS COMPUTED FROM LOW-VELOCITY DISCONTINUITY ANALYSIS

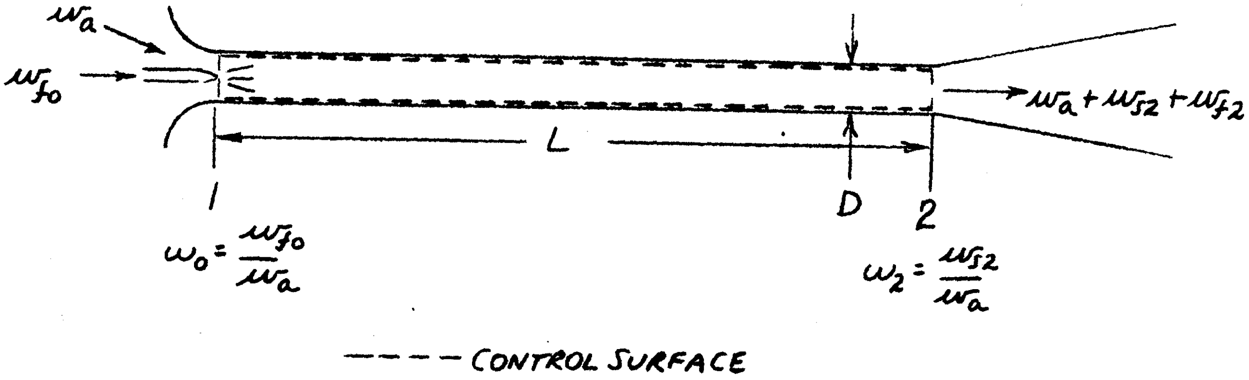

FIGURE 35a

FINITE CONTROL SURFACE FOR DISCONTINUITY ANALYSIS

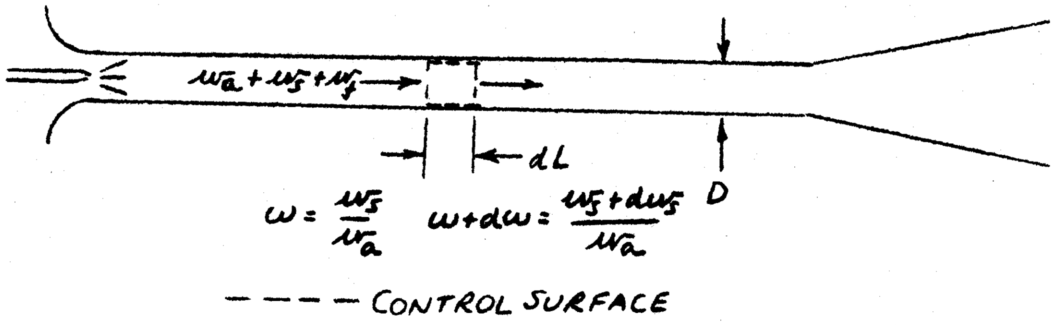

FIGURE 35 b

INFINITESMAL CONTROL SURFACE FOR DERIVATION OF INFLUENCE COEFFICIENTS

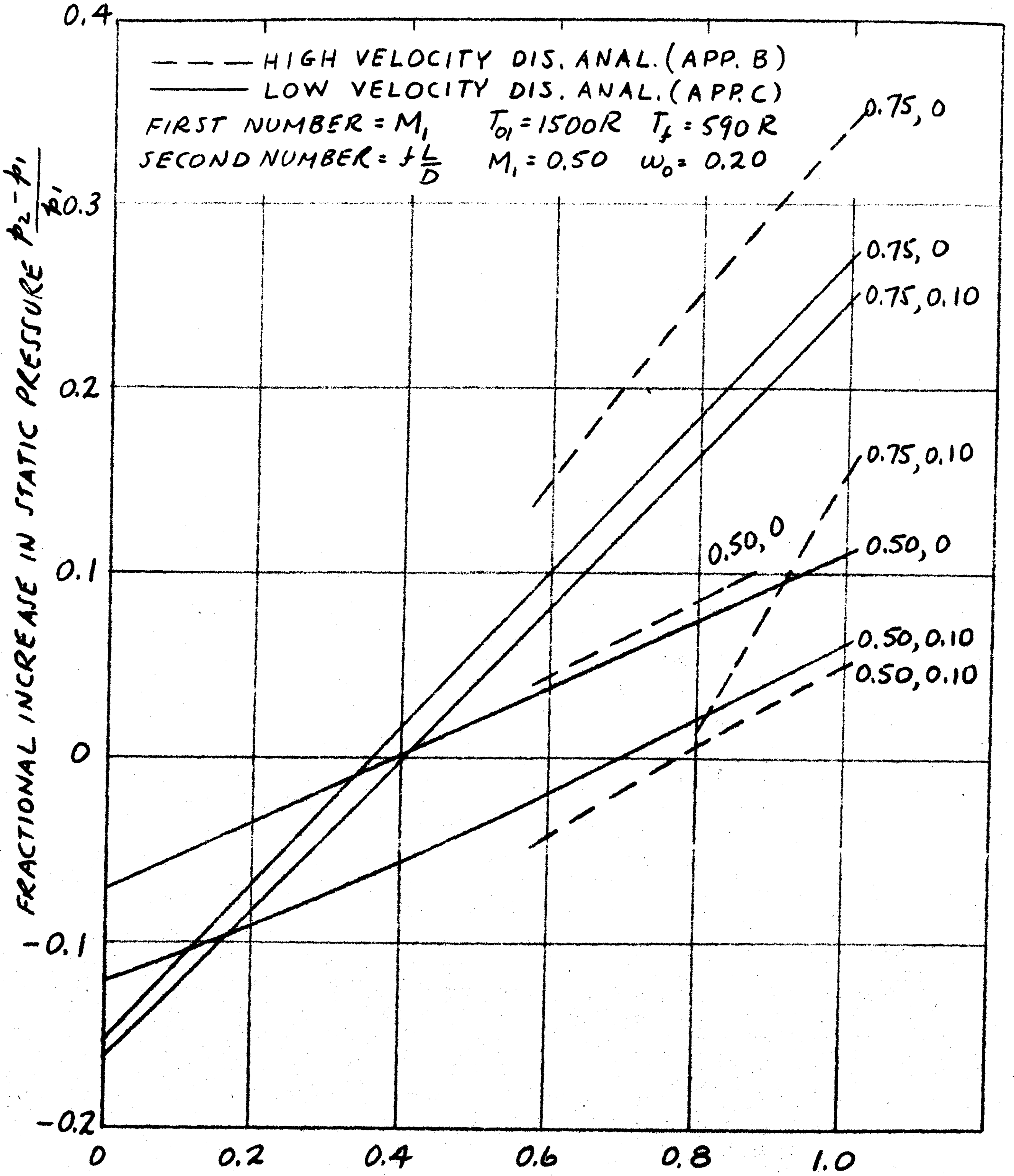

FIGURE 3b

COMPARISON OF COMPUTED RESULTS FOR LOW VELOCITY AND HIGH VELOCITY DISCONTINUITY ANALYSES — STATIC PRESSURE RISE VS. FRACTION EVAPORATED.

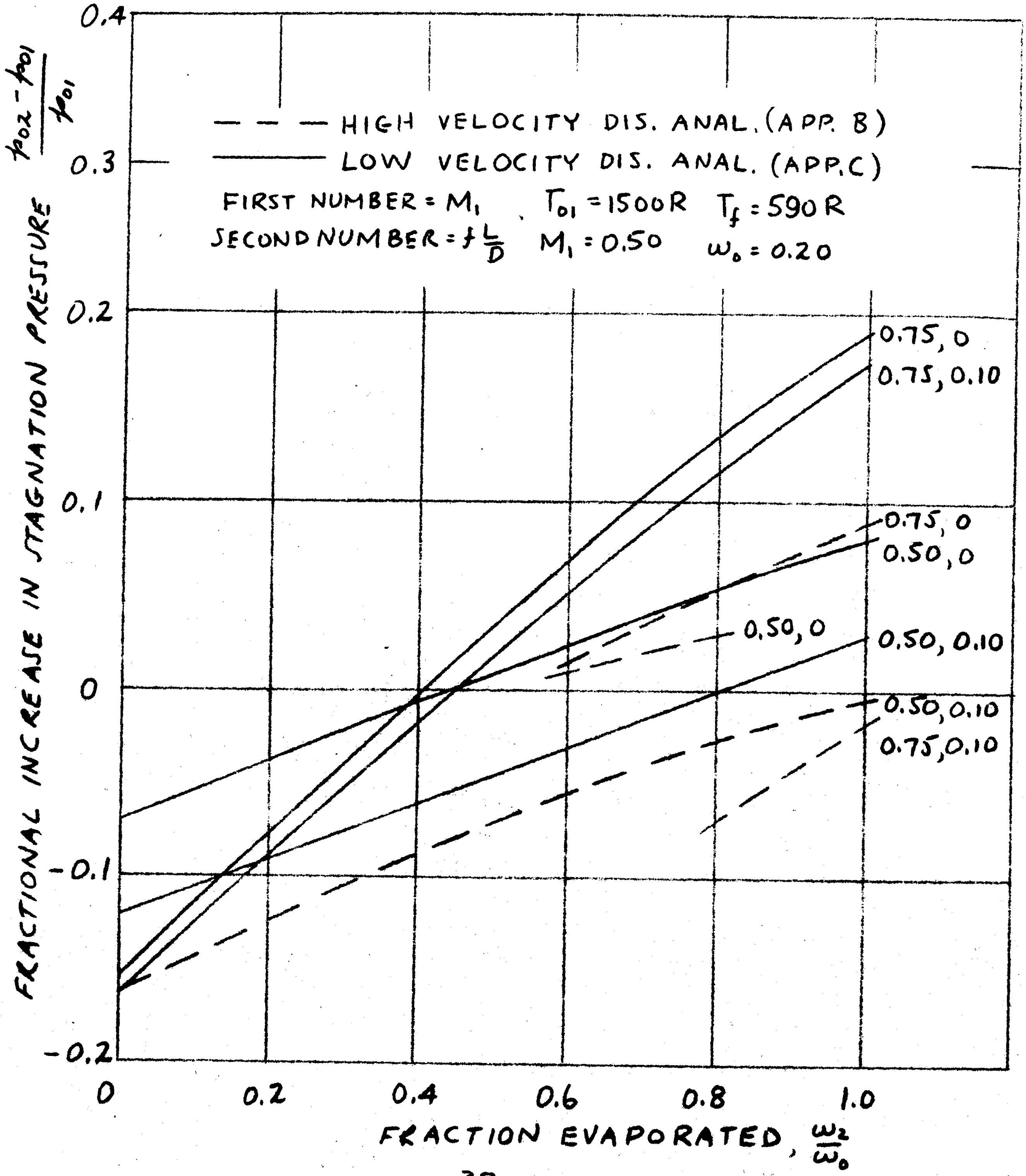

FIGURE 37

COMPARISON OF COMPUTED RESULTS FOR LOW VELOCITY AND HIGH VELOCITY DISCONTINUITY ANALYSES - STAGNATION PRESSURE RISE VS. FRACTION EVAPORATED.